CHARACTERIZATION OF THERMALLY EVAPORATED SILVER NANOPARTICLES ON GRAPHENE OXIDE COATED SUBSTRATE USING HOT-WIRE CHEMICAL VAPOUR DEPOSITION

NURUL HAZIERAH BINTI KAMARUDDIN

FACULTY OF SCIENCE
UNIVERSITY OF MALAYA
KUALA LUMPUR

2018

CHARACTERIZATION OF THERMALLY EVAPORATED SILVER NANOPARTICLES ON GRAPHENE OXIDE COATED SUBSTRATE USING HOT-WIRE CHEMICAL VAPOUR DEPOSITION

NURUL HAZIERAH BINTI KAMARUDDIN

DISSERTATION SUBMITTED IN FULFILMENT OF THE REQUIREMENTS FOR THE DEGREE OF MASTER OF SCIENCE

DEPARTMENT OF PHYSICS
FACULTY OF SCIENCE
UNIVERSITY OF MALAYA
KUALA LUMPUR

2018

UNIVERSITY OF MALAYA
ORIGINAL LITERARY WORK DECLARATION

Name of Candidate: **NURUL HAZIERAH BINTI KAMARUDDIN**

Matric No : **SGR130012**

Name of Degree : **MASTER OF SCIENCE**

Title of Dissertation ("this Work"):

CHARACTERIZATION OF THERMALLY EVAPORATED SILVER NANOPARTICLES ON GRAPHENE OXIDE COATED SUBSTRATE USING HOT-WIRE CHEMICAL VAPOUR DEPOSITION

Field of Study : **EXPERIMENTAL PHYSICS**

I do solemnly and sincerely declare that:

(1) I am the sole author/writer of this Work;
(2) This Work is original;
(3) Any use of any work in which copyright exists was done by way of fair dealing and for permitted purposes and any excerpt or extract from, or reference to or reproduction of any copyright work has been disclosed expressly and sufficiently and the title of the Work and its authorship have been acknowledged in this Work;
(4) I do not have any actual knowledge nor do I ought reasonably to know that the making of this work constitutes an infringement of any copyright work;
(5) I hereby assign all and every right in the copyright to this Work to the University of Malaya ("UM"), who henceforth shall be owner of the copyright in this Work and that any reproduction or use in any form or by any means whatsoever is prohibited without the written consent of UM having been first had and obtained;
(6) I am fully aware that if in the course of making this Work I have infringed any copyright whether intentionally or otherwise, I may be subject to legal action or any other action as may be determined by UM.

Candidate's Signature Date:

Subscribed and solemnly declared before,

Witness's Signature Date:

Name:
Designation:

CHARACTERIZATION OF THERMALLY EVAPORATED SILVER NANOPARTICLES ON GRAPHENE OXIDE COATED SUBSTRATE USING HOT-WIRE CHEMICAL VAPOUR DEPOSITION

ABSTRACT

In this research, silver nanoparticles (AgNPs) were grown by thermal evaporation technique in hydrogen gas ambient in a hot wire chemical vapour deposition (HWCVD) system. The graphene oxide (GO) thin films were spin coated onto either quartz or glass substrates in GO suspension synthesized by simplified Hummer's method from graphite flakes. AgNPs were grown on both bare and GO coated substrates to study the effects of the GO films on the properties and antibacterial activities of the AgNPs. The influence of deposition time of silver wire and substrate temperature during the AgNPs growth and post annealing environment on the morphology, optical and structural properties of the AgNPs were investigated. The field emission scanning electron microscopy images showed that the shape of AgNPs on GO coated quartz substrates was tunable towards spherically shaped nanoparticles with variation in growth parameters and post-annealing environment. The average size of AgNPs increased with the increase of growth time and the yield of uniform nanoparticle distribution was obtained at higher substrate temperature. AgNPs post-annealed in nitrogen gas environment were smaller in size as compared the AgNPs post-annealed in vacuum. Embedding AgNPs into GO film matrix showed significant effects on its structure and optical properties. Surface enhanced Raman scattering effect was obvious when AgNPs were introduced into the GO matrix. The size distribution and homogeneity of the AgNPs were consistent with the surface plasma resonance behavior of the AgNPs. Quenching of the photoluminescence intensity of AgNPs on GO coated substrate demonstrated a decrease in the electron-hole recombination rate. Electrical measurements on AgNPs on GO coated quartz substrates used in organic photovoltaic solar cell device structure showed four-fold enhancement in current density (J_{SC}) as compared to conventional organic solar cells without AgNPs. The antibacterial activity of AgNPs on GO coated glass substrates tested on *Staphylococcus aureus* (*S. aureus*) and *Escherichia coli* (*E. coli*) showed an increase in the area of zone of inhibition for bacteria as compared to AgNPs on bare glass substrates.

Keywords: Silver nanoparticles; graphene oxide; thermal evaporation; antibacterial; organic solar cells

PENGEWAPAN TERMA NANOPARTIKEL PERAK DI ATAS SUBSTRAT BERSALUT GRAFENA OKSIDA MENGGUNAKAN PEMENDAPAN WAP KIMIA WAYAR-PANAS

ABSTRAK

Di dalam penyelidikan ini, nanopartikel perak (AgNPs) telah dimendapkan dengan kaedah pengewapan terma berambienkan gas hidrogen di dalam sistem pemendapan wap kimia (HWCVD). Filem grafena oksida (GO) telah diputar salutkan samaada ke atas substrat kuarza atau kaca di dalam suspensi GO yang disintesiskan menggunakan kaedah Hummers yang dipermudahkan daripada serpihan grafit. AgNPs telah dimendapkan keatas kedua-dua substrat kosong dan yang disalutkan dengan GO untuk mengkaji kesan filem GO ke atas sifat-sifat dan aktiviti antibakteria bagi AgNPs. Pengaruh masa pemendapan wayar perak dan suhu substrat di masa pemendapan AgNPs dan persekitaran pasca penyepuhlindapan ke atas morfologi, sifat-sifat optik dan struktur AgNPs telah dikaji. Imej dari Mikroskopi Elektron Daya Imbasan (FESEM) menunjukkan yang bentuk AgNPs di atas substrat kuarza yang disalut GO boleh dikawal ke arah nanopartikel berbentuk sfera dengan variasi parameter pemendapan dan persekitaran pasca pemendapan. Purata saiz AgNPs bertambah dengan bertambahnya masa pemendapan dan penghasilan taburan nanopartikel yang seragam diperolehi pada suhu substrat yang tinggi. AgNPs yang disepuhlindap di dalam persekitaran gas nitrogen adalah lebih kecil saiznya berbanding dengan AgNPs yang disepuhlindapkan di dalam vakum. Memasukkan AgNPs ke dalam matriks filem GO menunjukkan kesan yang signifikan ke atas struktur dan sifat-sifat optik. Kesan penyerakan permukaan Raman meningkat apabila AgNPs dimasukkan ke dalam matriks filem GO. Taburan saiz dan kehomogenan AgNPs adalah konsisten dengan perlakuan resonan plasma permukaan bagi AgNPs. Pelindapkejutan bagi keamatan fotolumines (PL) bagi AgNPs di atas substrat disalut GO menunjukkan penurunan kadar penggabungan electron-lohong. Pengukuran elektrik ke atas AgNPs di atas substrat kuarza disalut GO yang digunakan di dalam struktur peranti sel suria organik fotovoltan menunjukkan peningkatan ketumpatan arus (J_{SC}) sebanyak empat kali ganda berbanding sel solar organik konvensional tanpa AgNPs. Aktiviti antibakteria pada AgNPs di atas substrat kaca disalut GO di uji dengan bakteria *Staphylococcus aureus* (*S. aureus*) dan *Escherichia coli* (*E. coli*) menunjukkan peningkatan zon penyekatan bakteria berbanding AgNPs di atas substrat kaca kosong.

Kata kunci: Nanopartikel perak; grafena oksida; pengewapan terma; antibakteria; sel solar organik

ACKNOWLEDGEMENTS

First and foremost, I would like to thank God “the almighty Allah”, whose many blessings have made me who I am today. I am deeply and forever indebted to my parents Mr. Kamaruddin Yaacob and Mrs Hasenah Mamat and all my siblings for their love and support they have given me throughout my entire life.

I am truly thankful to my supervisor, Dr. Zarina Aspanut, Professor Datin Dr. Saadah Abdul Rahman and Associate Professor Dr Vengadesh A/L Periasamy who not only gave me opportunity to conduct research under his supervision, but also showed me his tremendous help, support, patience and guidance in all stages of this thesis. I am thankful for being part of the group under their supervision as they always been concerned with the development of us.

I am greatly indebted to my group mates especially Mr. Chan Kee Wah, Mrs. Ilyani Putri, Mrs. Nurul Atiqah, Mr. Alif Rohaizad, Mr. Mohd Mukhlis and Mrs. Siti Norhaslinda for their assistance and support throughout the process.

In the completion of this work, my sincere thanks go to all the people in the Low Dimensional Materials Research Center lab, who made the lab a friendly environment for working. I would like to acknowledge Mr Mohamad and Mrs Norlela for the technical assistance, and more thanks to all my colleagues for their knowledgeable, support, and help especially to Linda, Syed, Aarthi, Maisara, Azrina, Fatin Saiha, Syifa, and Mardhiah.

Last but not least, I would like to thank University of Malaya for providing me the High Impact Research Grant (UM.C/625/1/HIR/030) and Postgraduate Research Fund (PG107-2012B), the Ministry of Higher Education for High Impact Research Grant.

TABLE OF CONTENTS

LIST OF FIGURES

LIST OF TABLES

LIST OF SYMBOLS AND ABBREVIATIONS

λ : Wavelength

J_{SC} : Short circuit current density

J_{max} : Maximum current density

P_{max} : Maximum power output

V_{OC} : Open circuit voltage

$\mathrm{PC_{71}BM}$: [6,6]-phenyl-C71-butyric-acid-methyl-ester

C_3H_6O : Acetone

Al : Aluminum

EM : Electromagnetic

E. coli : *Escherichia coli*

FESEM : Field Emission Scanning Electron Microscopy

FF : Fill factor

GO : Graphene Oxide

HTL : Hole transport layer

HWCVD : Hot wire chemical vapor deposition

HCl : Hydrochloric Acid

H_2O_2 : Hydrogen peroxide

ITO : Indium tin oxide

C_3H_8O : Isopropyl alcohol

NPs : Nanoparticles

H_3PO_4 : Phosphoric Acid

PEDOT:PSS : Poly (3, 4-ethylenedioxythiophene): poly(styrenesulfonate)

PCDTBT : Poly[N-90-heptadecanyl-2,7-carbazole-alt-5,5 - (40,70-di-2-thienyl-20,10,30-benzothiadiazole)]

$KMnO_4$: Potassium permanganate

RPM : Rotation per minute

AgNPs : Silver nanoparticles

sccm : Standard cubic centimeter per minute

S. aureus : *Staphylococcus aureus*

T_S : Substrate temperature

H_2SO_4 : Sulphuric acid

SPR : Surface plasmon resonance

UV-VIS-NIR : Ultraviolet-visible-near infrared

ZOI : Zone of inhibition

CHAPTER 1: INTRODUCTIONS

1.1 Research Background

1.1.1 Nanoscience and Nanotechnology

Nanoscience is a branch of science that mainly deals with the fundamental principles of molecules and structures having at least one dimension with a size range of 1 and 100 nm. Nanotechnology is an emerging technology that mainly focuses on the synthesis, processing, and applications of materials in nanoscale. Nanoscale materials or nanomaterials have been discovered and met tremendous interest in scientific research to generate innovations in many fields (El-Nour et al., 2010). Many great contributions have been created in the last few years such as medicine, electronics, advanced materials and environmental technology.

The nanomaterial is made up of at least a cluster of molecules. They are often looked as a key for a sustainable future due to their extremely small feature sized typically between 1-100 nm. The miniaturization of the particle relative to the bulk atoms causes some changes in the particle properties such as catalytic and chemical reactivity, electrical resistivity, and adhesion. The decrease in the particle size represents an increase in collective active surface area, thus results in higher chemical reactivity. Generally, the physical and chemical properties of the material are depending on the surface properties as surfaces are able to control the flow of a material or energy across an interface of material and its surrounding (Hickman, 2002).

1.1.2 Background of Silver Nanoparticles and Graphene Oxide

Silver nanoparticles (AgNPs) are popular among researchers due to its superior properties that can be utilized in various applications. AgNPs have distinctive physicochemical properties, including a high electrical and thermal conductivity, surface-enhanced Raman scattering, chemical stability, catalytic activity and non-linear optical behavior (Shahverdi et al., 2007). As the bulk metal is scaled down to nano dimensions, confinement effect of charge carrier and enhancement of surface to volume ratio is observed (Takami, 2012). A dramatic change in optical properties arises from the collective oscillation of the conduction electrons in the nanosize metal (Armelao et al., 2006; Atwater & Polman, 2010; Maier et al., 2003). This phenomenon is called surface plasmon resonance (SPR) effect which can lead to the highest absorption of incident light at a certain wavelength as a function of size, distribution, and shape of metal nanoparticles (NPs) (Willets & Van Duyne, 2007). By tailoring these physical properties, the position and intensity of SPR signal can be controlled in order to meet the needs of technological applications. The details of SPR phenomenon will be discussed in next section in Chapter 2.

Nowadays, researchers have focused their work on the architecture of AgNPs-dielectric with tailored topological features, including metal/insulator multilayers, core-shell structures and supported or embedded metal NPs. These tailored features may result in strongly diversified physicochemical properties (Cho et al., 2004). A well-tailored structure of AgNPs with uniform size distribution and shapes can be utilized in advance applications. AgNPs-dielectric represents an appealing class of functional systems for catalytic, optical, biological and medical applications (Mahmoud et al., 2012; Venugopal & Mitra, 2013). Various dielectric matrices have been reported such as graphene oxide (GO), silicon dioxide (SiO_2), titanium dioxide (TiO_2), and aluminum oxide (Al_2O_3) were used to study their interaction with AgNPs.

Recently, there has been growing interest in GO as dielectric materials or matrix for the growth of AgNPs. GO differs from graphene in a way that it has different oxygen functionalities, covalently bonded to carbon atoms of the hexagonal basal plane. The chemical functionalities present in GO makes it easily dispersible in different solvents, giving an opportunity to deposit on desired substrates, using simple techniques like spin coating and spray process (Wan et al., 2017). Hence, it is suitable to use as a matrix for the deposition of AgNPs.

1.2 Research Problems and Motivation

In recent years, great interest has been focused on precise control of the AgNPs structure due to its unique properties. Currently, many methods have been reported for the synthesis of AgNPs by using chemical, physical, electrochemical, photochemical, physical synthesis and biological routes (Krylova & Eremenko, 2005). Each method has advantages and disadvantages with common problems related to costs, scalability, particle sizes and size distribution. Among the existing methods, the chemical methods have been mostly used for the production of AgNPs.

Chemical methods provide an easy way to synthesize AgNPs in solution. However, this chemical method involved the use of hazardous chemicals which is not environmentally friendly and difficult to control the size and distribution of the growth NPs. Even though these AgNPs are relatively easy to synthesize, they are easily agglomerated to form larger particles which remain the main obstacle to overcome in the synthesis and thus resulted in the loss of their nanoscale properties. Therefore, there is a need for a technique to grow AgNPs which is environmentally friendly and has a better control on the size and distribution of the NPs.

Performance of organic solar cell with the incorporation of AgNPs-GO films as the hole transport layer and antibacterial activities of AgNPs have been investigated by many researchers. However, studies on these aspects on AgNPs grown by controlled thermal evaporation technique have not been reported much. Therefore, it would very interesting to investigate these properties on the AgNPs grown by the environmentally friendly physical technique used in this work. Potential applications of AgNPs and AgNPs-GO films grown by this technique can be useful in health-related devices.

1.3 Objectives of the Research

The objectives of this project are;

1. To obtain AgNPs on GO (AgNPs-GO) thin films by thermal evaporation using home-built HWCVD.
2. To identify the structural and optical properties of AgNPs-GO films using Raman scattering and optical absorbance spectroscopy.
3. To investigate the performance of organic solar cell with the incorporation of AgNPs-GO films as the hole transport layer (HTL) and the antibacterial activities of AgNPs-GO films layer against *Escherichia coli (E. coli)* and *Staphylococcus aureus (S. aureus).*

1.4 Thesis Structure

A brief overview of the chapters follows the present chapter is given next.

Chapter 2: Literature review

Chapter 2 outlines the literature review of this research. It starts with the background of the noble metal NPs. A brief discussion on the selection of AgNPs and GO as the candidate materials in this work are presented. SPR effects induced by the metal NPs will be introduced in terms of qualitative approach. Lastly, the potential industrial application of the AgNPs-GO film is presented as a conclusion to this chapter. This chapter ends with the setup and mechanism of the organic solar cell and antibacterial activity.

Chapter 3: Experimental methods

In this chapter, preparation techniques of AgNPs-GO films will be divided into two parts, i.e. GO synthesis and silver nanoparticle deposition. GO was synthesized using simplified

Hummer's method. Following this, spin coater was utilized to deposit GO thin film. Next, hot wire chemical vapor deposition method (HWCVD) is used to prepare AgNPs film. For the preparation of AgNPs, few parameters were varied to get the optimized parameter. Analytical techniques are carried out using field emission scanning electron microscopy (FESEM), Raman Spectroscopy and ultraviolet-visible-near infrared optical spectroscopy (UV-VIS-NIR) spectrophotometer. Their operation mechanism and provided information will be discussed. Then, the methods for organic solar cells (OSCs) device fabrication and the antibacterial application are explained at the end of this chapter.

Chapter 4: Results and discussion

This chapter consists of results and discussion obtained from different characterization techniques covering three categories; morphological, structural, and optical characterization. The first part of this chapter are discussing on the sample analysis prepared by three varied parameters i.e.; deposition time, substrate temperature and post-deposition heat treatment. Following this, the obtained result from current density-voltage (J-V) characteristic and disk diffusion experiments are presented.

Chapter 5: Conclusions and future works

The results obtained with a review on the objectives of this work are concluded in this chapter. Finally, suggestions for future studies are also included in this chapter.

CHAPTER 2: LITERATURE REVIEW

2.1 Chapter Overview

This chapter focuses on the research background of studies done in this field, covering topics related to the fundamental properties and various applications of noble metal NPs. The physical, chemical, optical properties and the latest advancement in technology on the usage of noble metal NPs are highlighted in this chapter. It is already established that noble metal NPs exhibit an intriguing phenomenon called the surface plasmon resonance (SPR). This phenomenon and its significance for various potential applications will be briefly discussed. The reason AgNPs and GO was chosen in this work will be discussed in this chapter. The growth methods for AgNPs and GO that have been utilized and their advantages will also be discussed. Finally, the potential application of AgNPs-GO film and its value for future technology such as for solar cell technology and antibacterial coating will be discussed.

2.2 Noble Metal Nanoparticles

Noble metal can be strictly defined as an electronic structure which requires a filled d-band which does not cross the Fermi level. Based on this definition, only gold (Au), silver (Ag) and Copper (Cu) fall in this category. Properties of particles of sizes between 1-100 nm behave differently from their bulk counterparts. New properties are observed on this nanoscale due to the interface that is not observed in the bulk counterparts. As the size or shape of the nanoparticle changes, the observed color also changes. Gold NPs have a characteristic red color, while silver NPs are yellow. Studies have shown that the color is due to the collective oscillation of the electrons in the conduction band known as the SPR. The oscillation frequency is usually in the visible region for gold and silver, giving rise to the strong SPR absorption (Eustis et al., 2006). The size miniaturization has led to the unique optical, electrical and catalytic properties of noble metals (Rai et al., 2009). The past several decades have shown tremendous advances in noble metal nanoparticle research. The unique properties of noble metal NPs have attracted researchers from many different areas, especially material scientists to explore the effectiveness of these noble metal NPs for advanced technology applications.

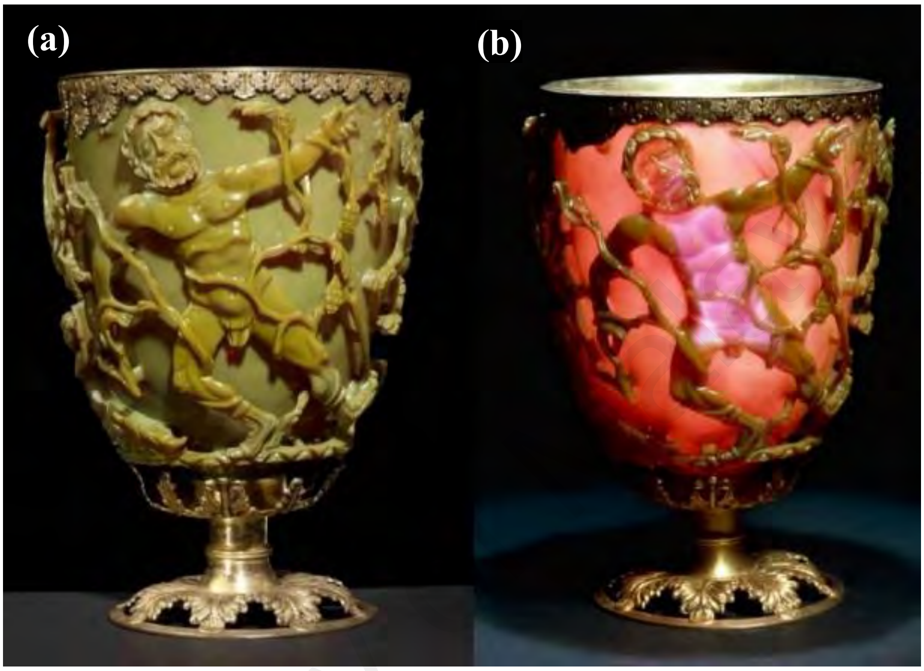

Figure 2.1: Lycurgus Cup (a Roman goblet dating from the 4th century A.D) in (a) reflected and (b) transmitted light.

This unique optical property of noble metals NPs is portrayed in the Lycurgus cup in Roman times as shown in Figure 2.1. The cup appears to be green in daylight due to reflected light. However, when illuminated from within, it turns into a glowing translucent red. This phenomenon can be understood due to the light-scattering effect exhibited by nano-sized Ag and Au particles (Kolwas & Derkachova, 2015). It is interesting to observe that different sizes of noble metal NPs can produce different colors when scattered by light. When the particle size approaches the size of the wavelengths of visible light, the SPR effect takes place. The tunable SPR absorption peak is found to be highly sensitive to the structural properties of metal NPs which in turn changes the frequency and intensity of the SPR peak (Lee et al., 2008). The detailed mechanism of the SPR effects will be discussed in the next part.

2.3 Surface Plasmon Resonance

The miniaturization of optical components to nanoscale dimension involves interesting physical processes such as light localization and electromagnetic (EM) radiation (Maier et al., 2003). To study such processes, an interdisciplinary field known as plasmonics was proposed and has become one of the important research fields regarding modern optics in recent years (Halas et al., 2011; Maier & Atwater, 2005). Back in 1908, Gustav Mie proposed that the interaction of light with metal NPs will result in the collective oscillation of metal-free electrons with respect to the nanoparticle lattice in resonance with the light field (Mie, 1908). This light interaction is known as SPR.

SPR is a phenomenon of coherent oscillation of surface conduction electrons excited by electromagnetic (EM). This SPR can be recognized by UV-VIS-NIR spectroscopy which shows intense and broad optical absorption bands that arise from the coherent oscillations of conduction electrons near the NPs' surfaces. This can be attributed to the enhancement of the local electromagnetic field near the metal surface when the wavelength of the irradiation source is coincident with the optical absorption of the surface plasmon (Su et al., 2012).

In general, there are two types of SPR which are surface plasmon polaritons and localized SPR (Halas et al., 2011; Jones et al., 2011). The former phenomenon originates from the propagating wave along a metal surface or metal-dielectric film boundaries as shown in Figure 2.2 (b). As for localized SPR, it can be attributed to the localized surface plasmon in metallic NPs that have dimensions smaller than the wavelength of the incident light, λ. In practice, more attention has been paid to localize SPR because of its applications to metal NPs with various morphologies.

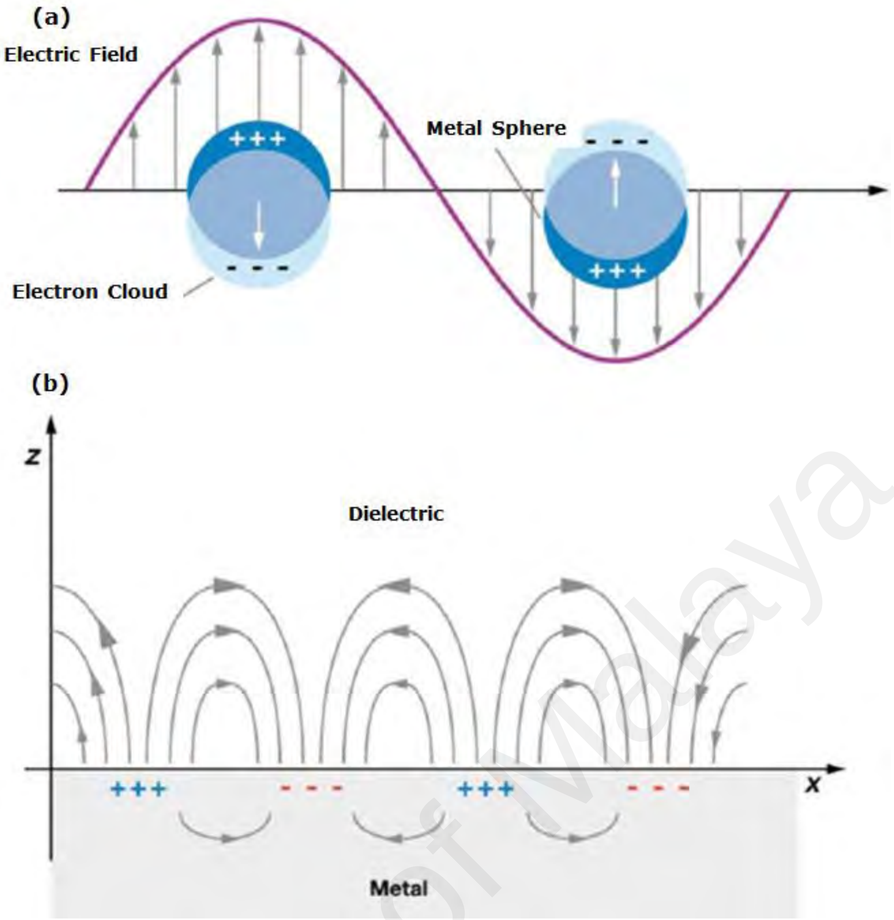

Figure 2.2: Schematic illustration of a (a) localized surface plasmon and (b) a surface plasmon polariton.

When a small spherical metallic nanoparticle is irradiated by light (EM) radiation, the oscillating electric field causes the conduction electrons to oscillate coherently as shown in Figure 2.2 (a). When the electron cloud is displaced relative to the nuclei, a restoring force arises from the Coulomb attraction between the electrons and nuclei, resulting in the oscillation of the electron cloud relative to the nuclear framework. A resonance condition is established when the frequency of light matches the natural frequency of valence electrons oscillating against this restoring force. The displacement of electron cloud generates light absorption in the metal NPs. This light absorption can be observed using UV-visible spectroscopy which is known as SPR that excites in a visible range of 380 nm – 700 nm. The SPR is determined by four factors: density of electrons, effective electron mass, and the shape and size of the charge distribution (Kelly et al., 2003).

Conversely, on bulk metal, the propagation of surface plasmon occurs along the metal surface which is excited in the infrared region of the electromagnetic spectrum. The rest of the light is reflected, making this material suitable to be used as a mirror. The displacement of electron density generates light absorption in metals. Such unique optical features make metal NPs extremely valuable in a wide range of technological applications such as optical devices (Kalfagiannis et al., 2012), chemical and biological sensors (Fan et al., 2014), various surface-enhanced spectroscopies (Kim et al., 2012) and so on.

2.4 Silver Nanoparticles – Graphene Oxide Thin Films

In this work, in the preparation of nanocomposite film, from other noble metal, silver (Ag) was chosen as the metal source. Ag, like other metals, is generally malleable and ductile, conducts electricity and heat, and has a metallic luster property. Ag forms a strong metallic bond which is non-directional and strong due to the positively charged metal atoms in fixed positions surrounded by delocalized electrons. The delocalized electrons are said to be “free” and ready to move throughout the metal, which in turn contributes to the high electrical and thermal conductivities. Like the other noble metals, Ag can support many different plasmon modes which has the highest absorption efficiency with low absorption loss. This can be attributed to the fact that the interesting properties of nanoscale Ag can be developed due to the lack of symmetry at the interface or electron confinements that do not scale linearly with size (Eustis et al., 2006). Of other noble metals, Ag has probably played the most important role in the development of plasmonic, and its unique properties make it well-suited for most of the next generation plasmonic technologies.

Controlling the morphology of Ag at the nanoscale level presents numerous properties which could be altered depending on the applications requirement. These have resulted in a growing number of scientists researching on AgNPs material in recent years. This phenomenon mainly results from the additional energetic term of $\gamma_o A$ where γ_o is surface excess free energy and A is the surface area (Ruffino & Grimaldi, 2013). Due to the large surface/volume ratio of NPs, this term has become important in changing the physical and chemical properties of NPs with respect to its bulk materials.

Driven by the intriguing properties exhibited by AgNPs, recently, AgNPs have been utilized as a fundamental component for optoelectronics (Su et al., 2015; Xiang et al., 2016), biology (Rai et al., 2009; Zhu et al., 2013) and the multidisciplinary fields. The fabrication of NPs through physical methods with controllable size and shape has been intensively studied for decades. The AgNPs' size and shape are the main parameters that determine their optical and electrical properties and therefore, enhance the performance of a device. AgNPs are relatively easy to synthesize using commercialized methods. However, they tend to agglomerate to form larger particles, thus resulting in the loss of their nanoscale properties. The tendency of AgNPs to agglomerate arises from their surface energy which has resulted in the lower performance of the device's application properties. Thus, to improve the performance of AgNPs in advanced applications, the agglomeration of AgNPs is the main obstacle need to overcome.

Based on previous publications, changing the dielectric material of AgNPs has proven to control the agglomeration of AgNPs. Among various dielectric matrices, oxide matrices such as SiO_2, TiO_2 and Al_2O_3 are most favorable (Liu et al., 2015). Nanohybrid materials based on AgNPs and GO have attracted considerable research interest (Li et al., 2015; Mehl et al., 2015; Tran & Jeong, 2015).

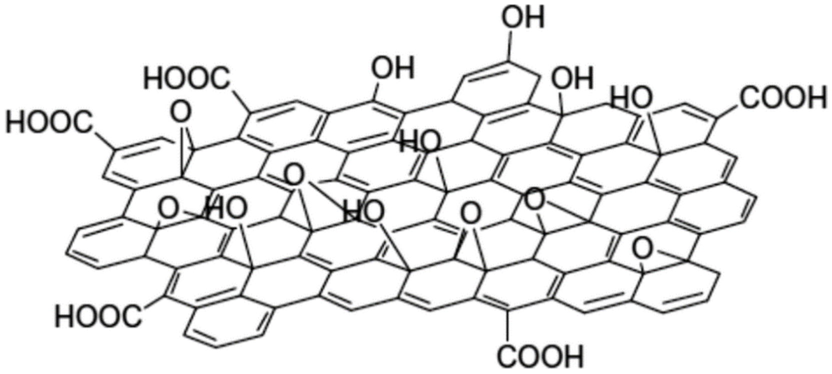

Figure 2.3: The chemical structure of graphene oxide.

GO can be defined as monolayers of carbon atoms that form dense honeycomb structures containing an abundance of oxygen functional group epoxide (-O-) and hydroxyl (-OH) functional groups on the two accessible sides, while carbonyl (-CHO) carboxylic groups (-COOH) cluster at the edges (Ganguly et al., 2011). The chemical structure of GO was shown in Figure 2.3. It has been known that the presence of defects and oxygen functional groups make GO excellent templates for the post assembly of NPs.

The oxygenated functional groups can act as anchor sites for the deposition and nucleation of particles, consequently forming AgNPs on the surfaces and edges of the GO sheets. Figure 2.4 shows the structural process for the deposition of GO and AgNPs-GO. Large surface areas of GO can be as platform for AgNPs to adhere on it which will reduce the agglomeration of AgNPs. Thus, this structure allowed researchers to study the properties that exhibits by Ag. The crystallization of AgNPs on the GO surface could prevent the agglomeration of AgNPs and simultaneously prevent the restacking of the GO sheet (Xu & Wang, 2009). Based on the research done previously, hybrid AgNPs-GO exhibits superior properties in terms of its optical and electrical properties.

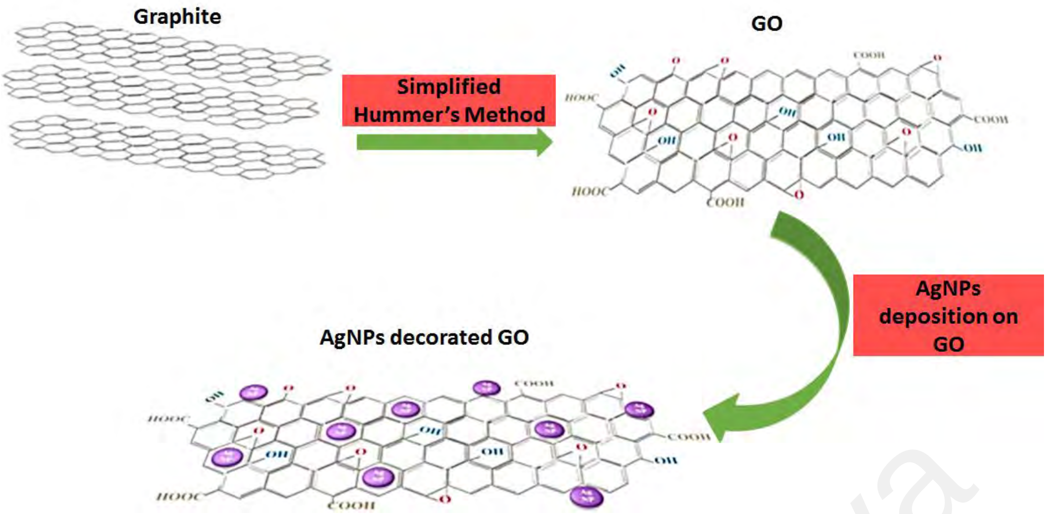

Figure 2.4: The structural process for deposition of GO and AgNPs-GO.

As aforementioned, many researchers had reported on the remarkable applications of AgNPs-GO in surface-enhanced Raman scattering (Kim et al., 2012), catalysis (Qi et al., 2013), sensors (Huang et al., 2016; Hafiz et al., 2014) and antimicrobials applications (Liu et al., 2011). The presence of AgNPs-GO displays superior sensing properties compared to GO and AgNPs on multiwall carbon nanotubes (Cui et al., 2013). This result is in agreement with other researchers that had marked an enhancement in the sensing performance of AgNPs-GO compared to GO alone (Kavinkumar & Manivannan, 2016). To explore the combined superior properties of AgNPs and GO sheets, AgNPs-GO nanohybrid materials have been intensively studied.

2.5 Deposition of Graphene Oxide

The most common method to synthesize graphene oxide is called the Hummers method. This method involves the oxidation of graphite flakes using an oxidizing agent in an acidic environment. The oxidation process will increase the interplanar distance between the graphite layers. The degree of oxidation depends on the reaction conditions and the precursor graphite used. Note that GO is formed through the complete exfoliation of graphite oxide by sonication or vigorously stirred in water for a long time. During the oxidation process, the increase in interplanar distance disrupts graphite's sp^2 bonding network, causing the non-conductivity of GO (Stone, 1988). Oxygen reacts to different sites on the graphite sheets and may attach to the adjacent carbon on the surface. This reaction causes the weakening of the Van der Waals interaction between the graphene layers. The π conjugated structure and electrical conductivity of GO can be healed to the level of graphite through a controlled process of deoxidation by restoring the carbon network through chemical reduction (Marcano et al., 2010).

Past researchers have focused more on the deposition of GO as a thin film. This is driven by the fact that GO thin film can be immediately integrated into practical devices. Moreover, the hydrophilicity of GO allows it to be easily deposited on substrates as thin film. GO contains several oxide functional groups, mainly alcohols and epoxides, and it also can adsorbed water above and below the carbon basal plane (Marcano et al., 2010). Control over film uniformity, surface morphology, thickness, and surface coverage depend on the deposition methods and parameters used. Drop casting (Lorenzoni et al., 2015), dip coating, and spin coating (Jeong et al., 2010; Kumar et al., 2015; Thouti et al., 2015) are widely used methods to deposit GO thin films on substrates. Figure 2.5 illustrates the dip-coating and drop-casting deposition of GO.

Figure 2.5: The dip-coating and drop-casting deposition methods (Reese & Bao, 2007).

Dip-coating and drop-casting are relatively easy methods to be used to deposit GO thin films. Figure 2.5 presents the dip-coating and drop-casting deposition methods. Using these methods, the film will be deposited non-uniformly on the substrate and results in the agglomeration of GO platelets as the droplets of water evaporate and grow smaller. The interaction between water with the substrate is important to deposit the GO on the substrate. This is in conjunction to the dispersion of GO platelets in water, thus making it more concentrated as evaporation happens, resulting in agglomeration (Scott et al., 2007).

For the spin-coating method (Eda & Chhowalla, 2010; Jeong et al., 2010; Thouti et al., 2015), a relatively high concentration (0.5 – 3 mg mL^{-1}) of GO is required to deposit a uniform thin film. The rapid evaporation of solvent during spin-coating is important to ensure greater adhesion of GO sheet with the substrate surface. Compared to the drop-casting and dip-coating methods, spin-coating offers a more uniform and continuous film with typically less wrinkling. The film thickness can be controlled by adjusting the value for rotation per minute (rpm), spinning time and concentration of GO. Thereby, in this work, the spin-coating method is chosen to deposit GO thin films.

2.6 Growth Methods of Silver Nanoparticles

An array of physical, chemical and biological methods has been used to synthesis nanomaterials. Detailed methodologies have been utilized to synthesis noble metal NPs of particular sizes and shapes. Those methods include chemical reduction (Tan et al., 2002; Petit et al., 1993; Vorobyova & Lesnikovich, 1999), green synthesis (Ethiraj et al., 2016), laser ablation (Mafune et al., 2000), gamma irradiation (He et al., 2015), thermal decomposition (Tam et al., 2013), magnetron sputtering (Asanithi et al., 2012), photochemical methods (Sarkar et al., 2015), and microwave-assisted synthesis (Mahmoudi et al., 2016). All the listed methods have been successfully used to grow AgNPs. However, most of the commercialized methods struggle with size and shape controllability as well as aggregation. Furthermore, most of these methods involve large production costs as well as usage of hazardous chemicals which are not environmental-friendly.

Gas-phase nanoparticle production offers a huge advantage over wet-chemistry synthesis techniques as it allows particles to grow in an inert gas environment such as hydrogen (H_2), helium (He) or nitrogen (N_2). Furthermore, the gas-phase production does not involve the usage of hazardous wet chemicals. The most common techniques for the production of gas-phase metal NPs are inert-gas condensation (Raffi et al., 2007), spark generation (Messing et al., 2009), sputtering (Asanithi et al., 2012), furnace flow reactor (Zainy et al., 2012) and thermal evaporation (Boies et al., 2011; Haidari et al., 2015). Most synthesis methods of NPs in the gas phase are based on homogeneous nucleation in the gas phase and subsequent condensation and coagulation.

HWCVD is a relatively new deposition technology which was developed over the past 20 years. HWCVD is a low pressure deposition technique to deposit functional films, both inorganic and organic, based on the decomposition of precursor sources dissociated at a heated metallic surface (Schropp, 2015). This method provides improved controls of parameter which can produce high quality films. Researchers have utilized HWCVD to deposit metal oxide nanoparticles, carbon nanotubes, and functional polymer coatings. HWCVD utilizes the catalytic ability of metal filaments (e.g., Tungsten or Tantalum) to decompose the source gases to radicals at high temperatures (≥1500 °C). HWCVD technique is attractive in many ways whereby the deposition does not involve plasma that might have effect of damaging bombardment of energetic ions on the deposited films. Furthermore, HWCVD is an easy and scalable method. The uniformity of the deposited thin films can be easily optimized by controlling the parameters. Among parameters that can be varied in HWCVD setup are substrate temperature, deposition time, deposition pressure, filament to substrate distance (Schropp, 2009; Thangala et al., 2009).

Thermal evaporation is one of the simplest and most effective physical methods for synthesizing metal NPs. This fabrication technique results in a random array of particles with a variety of shapes and sizes. However, with the proper control of parameters, the size and shape of NPs can be well controlled. In this work, the thermal evaporation technique is utilized using HWCVD system to deposit AgNPs. This is driven by its advantages such as being cost-effective, environmentally friendly, and simple and sustainable. The experimental setup of this technique will be discussed in detail in Chapter 3.

2.7 Application of Silver Nanoparticles as Hole Transport Layer in Organic Solar Cells

Organic solar cells (OSCs) are of great interest to researchers due to their promising potential as a cost-effective photovoltaic technology in the harvesting of solar energy (Haidari et al., 2015). However, OSCs suffer low efficiency owing to the short exciton diffusion length. The exciton diffusion length is limited in the order of 10–15 nm to allow for the exciton generation. Furthermore increases of active layer thickness will hinder exciton generation (Park et al., 2009). Intensive research has been carried out over the last decade to improve the power conversion efficiency of OSCs through the development of novel materials and effective device engineering (Eda et al., 2008; Park et al., 2009). Much effort has been applied in integrating metallic nanostructures and graphene and its derivatives in OSCs for efficient device performance. Among other approaches, plasmonic enhancement by noble metal NPs was found as a promising method to improve absorption for a better light-trapping approach to enhance photocurrent generation (Fleetham et al., 2015). AgNPs are typically embedded into active or buffer layers or placed at the interfaces of active and buffer layers for this purpose.

Recently, it is been reported that nanocomposites consisting of AgNPs-GO surface is an efficient technique to improve device performance due to their enhanced catalytic and optoelectronic properties (de Faria et al., 2014; Mahmoudi et al., 2016). Graphene and its derivatives are compatible for the interfacial layers of OSCs due to their proper energy level alignment and chemical stability, especially in the hole-extraction layer (Kim et al., 2014). The growth of AgNPs-GO structure has also been shown to be effective in preventing the agglomeration of AgNPs (Fernando et al., 2014). Thus, with the effects of GO, the light-trapping properties of the device is expected to increase, which can lead to an improvement in the short-circuit current density (J_{SC}). It has been reported that the introduction of the AgNPs-GO layer into the active layer produces a high power conversion in OSCs (Sutradhar & Saha, 2016).

In this work, the multilayer stacks of AgNPs-GO films which form a nanocomposite structure with high transparency in the visible and near UV region can be obtained with proper controlled thickness of the AgNPs and GO film. A good material for hole transport layer (HTL) must be transparent so that it can absorb more light to be transferred to the active layer. The incorporation of AgNPs-GO into conventional OSCs devices as HTL will greatly enhance the photocurrent efficiency and reduce the cost per watt of thin film solar cells.

With all the above-mentioned potential applications of AgNPs-GO films, it can be deduced that AgNPs-GO film is indeed a very interesting and challenging topic to study. Therefore, by carefully and properly designing the experiment parameters, the current study is prospected to contribute to the research on this material significantly. Further details on the OSC devices will be explained in detail in Chapter 3.

There are a few important values that can be obtained from solar cell devices;

(1) Short circuit current density

J_{SC} is the cell photocurrent measured at the point where the external bias voltage is zero when there is no opposing force to the current flow from the cell and is the maximum current the cell can generate. Generally, it is presented in the form of the *Jsc* and is defined as the ratio of the short circuit photocurrent to the active cell area.

(2) Open circuit voltage

Open circuit voltage (V_{OC}) is the cell voltage measured when the current within the cell is equal to zero.

(3) Fill Factor

The fill factor (FF) measures the "squareness" of the curve. For instance, a resistive loss in the cell is shown directly from the shape of the *J-V* curve, making it "flatter" and decreasing the fill factor as shown in Figure 2.6. FF is defined as the ratio of maximum power output (P_{max}) to the product of short circuit current and open circuit voltage.

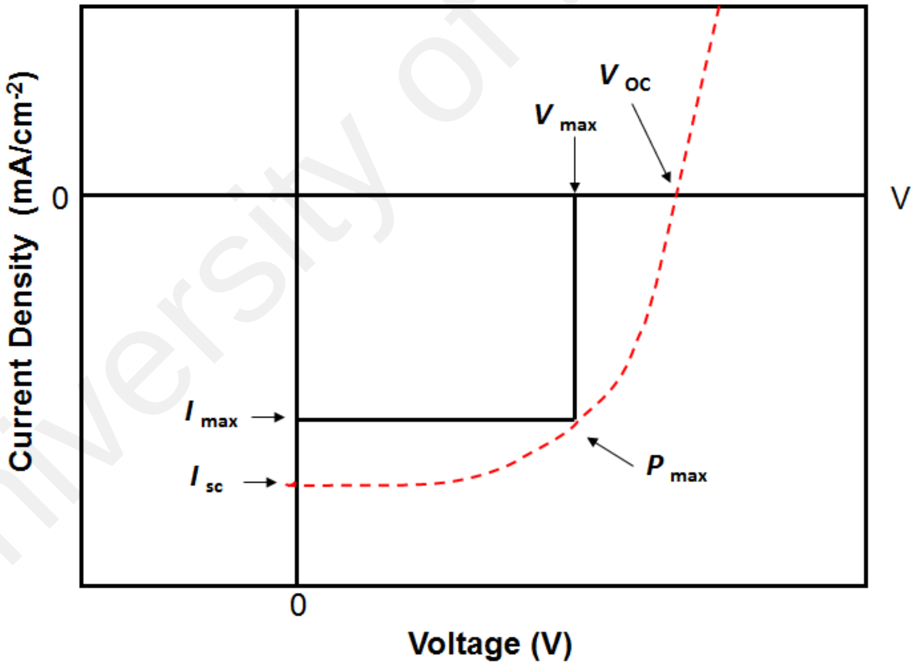

Figure 2.6: Current density-voltage (*J-V*) curve of organic solar cells.

Surveying the above-presented results on the study of plasmonic solar cells, Atwater and Polman (Atwater et al., 2010) noted that plasmonic structures can offer at least three methods for performing near-complete light absorption and photocarrier collection while reducing the thickness of the absorbing layer: (1) light scattering by plasmons. In this method, metal NPs are used as subwavelength scattering elements to couple and trap freely propagating plane waves from sunlight into a thin absorbing layer; (2) light concentration by plasmons. In this method, metal NPs are used as subwavelength antennas in which the plasmonic near-field is coupled to the semiconductor, increasing its effective absorption cross section; and (3) light trapping by surface plasmon polaritons (SPPs). In this method, a corrugated metallic film on the back surface of a thin photovoltaic absorbing layer can couple sunlight into SPP modes supported at the metal/semiconductor interface as well as into guide modes in the semiconductor slab where the light is converted to photocarriers in the semiconductor.

2.8 Antibacterial Activities of Silver Nanoparticles

AgNPs are known to exhibit the highest antibacterial activity compared to other metals (Rai et al., 2009). Scientists have found that bacteria are less prone to develop resistance against AgNPs (Park et al., 2015; Xiu et al., 2012; Zhao & Jr, 1998). The high reactivity and biocompatibility of AgNPs are related to its large surface to volume ratio. NPs play an important role in inhibiting bacterial growth in aqueous and solid media as well as increase the penetration potential of Ag particles, therefore aiding in the better utilization of metal properties (Panacek et al., 2006; Rai et al., 2009; Xiu et al., 2012). Nowadays, it has been reported that the hybrid material resulting from the combination of AgNPs with other matrices is an effective bactericidal agent that can inactivate microorganism cells.

For instance, the combination of GO nanosheets and AgNPs has showed enhancement in antibacterial performance because the GO substrates inhibit the aggregation and depletion of AgNPs. Moreover, AgNPs-GO hybrid films are biocompatible, thus providing enhanced biocompatibility (Zhang et al., 2015). This suggests that stable AgNPs-GO hybrid films will have potential applications in water purification, antibacterial materials, medical biomaterials, cell culture scaffolds, and environmental remediation.

Recently, studies have shown that GO could be effectively utilized for its antibacterial properties (Akhavan & Ghaderi, 2010; Chook et al., 2012; Liu et al., 2011). It was reported that the inactivation of bacteria is due to the direct contact of the cell membrane to the sharp edges of GO materials (Akhavan et al., 2010). It was suggested that the high density of the functional groups and small size of the GO structure result in more interaction with bacteria cells, thus killing the bacteria (Liu et al., 2011). However, a few articles have stated that GO can encourage biofilm formation at the coating surface (Das et al., 2011; Ruiz et al., 2011). Das et al. showed that when GO was placed in the center of a nutrient media plate previously inoculated with bacteria, a growth inhibition zone was not formed. Alternatively, when AgNPs-decorated GO was used, a clear inhibition zone was formed (Das et al., 2011). In a few reports, enhancement of the antibacterial activities of AgNPs was observed when complemented with the GO structure as an adhesion matrix (Akhavan et al., 2010; Chook et al., 2012; Das et al., 2011).

Figure 2.7 presents the common mechanism of bacteria cell death induced by metal NPs. The exact mechanism of the antimicrobial action of silver is not fully understood yet. From Figure 2.7, several hypotheses have been pointed out on the antibacterial action of AgNPs, namely: (i) the release of Ag^+ ions; (ii) direct interaction of the AgNPs and bacteria cell membrane, and (iii) the production of reactive oxygen species (ROS). Among all, the release of Ag^+ ions are claimed to produce the most effective antibacterial agent. To become a good antibacterial agent, a high rate of Ag^+ ion release is more favorable. Smaller sizes of AgNPs have a higher rate of Ag^+ released (Xiu et al., 2012).

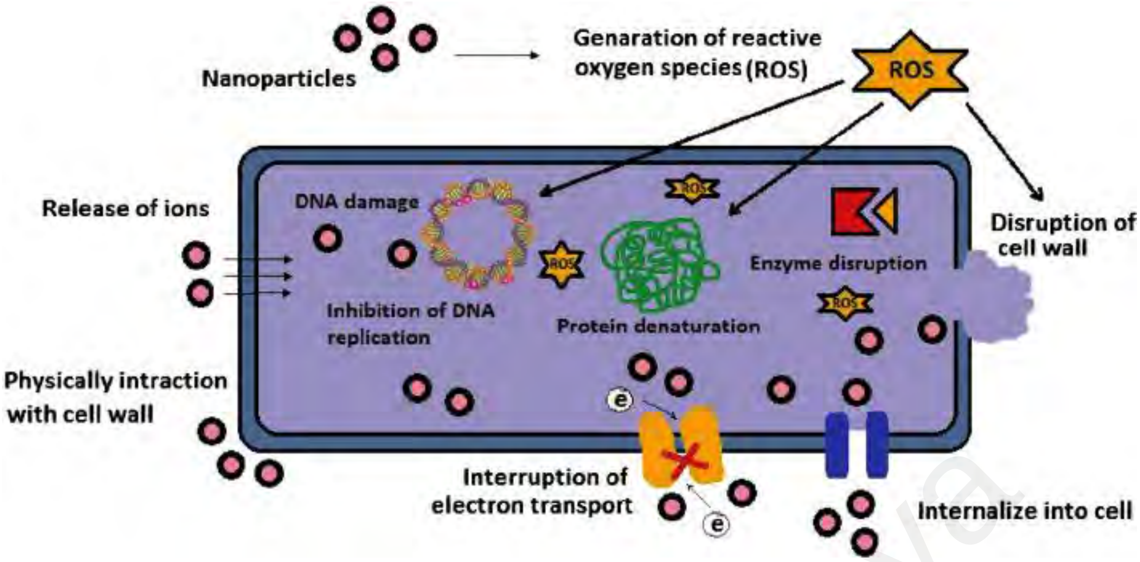

Figure 2.7: Common mechanism of cellular death induced by metal nanoparticles (Dizaj et al., 2014).

CHAPTER 3: EXPERIMENTAL METHODS

3.1 Chapter Overview

Hot wire synthesis using a homebuilt hot wire chemical vapour deposition (HWCVD) system was utilized in this research to deposit AgNPs on bare and GO coated substrates. Prior to the deposition of AgNPs, the deposition of GO was done by spin-coating. This chapter will discuss the preparation, deposition methods, and characterization of the AgNPs-GO films. The preparation of thin films will be explained in detail in this chapter. A few parameters were varied to obtain the optimized nanostructure of AgNPs-GO. The morphology, optical characterizations, and structural changes were made to the deposited film using Field Emission Scanning Electron Microscopy (FESEM), Jasco V-570 UV/VIS/NIR Spectroscopy and Renishaw inVia Raman Microscope respectively. Finally, the experimental methods on the device fabrication will be explained at the end of this chapter.

3.2 Substrate Preparation

Commercially available glass substrate was purchased and used as the substrate for the deposition of the AgNPs and GO thin film. In this work, glass, quartz and Indium Tin Oxide (ITO) coated glass were used as substrates for the samples. Samples of the quartz substrate were used for optical absorbance and Raman scattering spectroscopy measurements. The study on the performance of OSCs incorporated with AgNPs as a HTL was performed on samples deposited on ITO coated glass substrate, while samples on glass substrates were used to study the antibacterial activities of AgNPs. Glass and quartz substrates were cut to the size of 1.0 cm x 1.0 cm for the measurements of optical properties and ITO (1.5 cm x 2.0 cm) for the application. The cleaning process adopted in this work is similar to the Radio Corporation of America (RCA) cleaning process which involves the removal of organic contaminants, thin oxide layer and ionic contamination. This RCA cleaning process was developed by Werner Kern in 1965 while working for RCA (Radio Corporation of America) (Mattox, 1998; Clark & Wagener, 2008).

As for the cleaning process of glass and quartz substrates, it began with soaking the substrates in a beaker containing soap solution, a mixture of Decon 90 and deionized water. Following this, the whole beaker was immersed in an ultrasonic bath for the ultrasonic cleaning process which lasted for 15 minutes at a temperature of 60 °C. In ultrasonic cleaning, a high-frequency sound wave was used to agitate the reverse osmosis (RO) water which in turn acts on the contaminants adhering to the substrates. Contaminants can be dust, dirt, oil, grease, polishing compounds, and fingerprints. The quartz substrates were rinsed with deionized water before being further rinsed in highly flammable acetone, C_3H_6O (99.5 %, 58.08 g/mol) and finally in isopropyl alcohol, C_3H_8O (95 %, 46.07 g/mol) to remove any oil deposits and other contaminants. The next step is to dry the substrates using an N_2 gun blower to prevent the formation of water spots. ITO substrates were cleaned using a similar method with quartz substrates; i.e. by soaking them sequentially in a detergent solution, acetone, isopropyl alcohol and deionised water.

3.3 Material and Sample Preparation

Graphite flakes (3061, Asbury Graphite Mills Inc.), sulfuric acid (H_2SO_4, 98 %), potassium permanganate ($KMnO_4$, 99 %), phosphoric acid (H_3PO_4) hydrogen peroxide (H_2O_2, 30 %) and ethanol (C_2H_5OH, 95 %) were purchased from Merck (Darmstadt, Germany). Hydrochloric acid (HCl, 37 %), silver wire (99.99 %) and tungsten wire were purchased from Sigma-Aldrich (St. Louis, M.O.).

3.4 Synthesis of Graphene Oxide

An aqueous suspension of GO was prepared according to the simplified Hummer's method (Marcano et al., 2010). In this synthesis, 3 g of graphite powder was mixed into the solution containing concentrated (360 ml) H_2SO_4 and (40 ml) H_3PO_4. Then, 18 g of $KMnO_4$ was added gradually under controlled stirring and temperature. The solution was left for 3 days for the oxidation process to take place. The graphite oxide was obtained after H_2O_2 was added to the mixture to reduce the residual $KMnO_4$. A yellowish-brown solution was observed at this stage. Finally, the mixture was filtered and washed with HCl aqueous solution to remove metal ions followed by water to remove acid. Then, the graphite oxide was subjected to ultra-sonication for GO. Figure 3.1 shows the as-synthesized graphene oxide solution. The concentration of GO was calculated as shown in Table 3.1.

Figure 3.1: Graphene Oxide solution.

Table 3.1: Concentration calculation for the synthesized GO.

Sample	Mass of petri dish, M_p (mg)	Mass of petri dish + Mass of dried GO,M_{p+GO} (mg)	Mass of GO, $M_{GO} = M_{p+GO} - M_p$ (mg)	Volume of GO used, V_{GO} (ml)	Concentration of GO produced, $\rho_{GO} = M_{GO}/V_{GO}$ (mg/ml)
1	72491.1	72656.1	159.0	15	10.6
2	66576.2	66749.0	172.8	15	11.5
3	67337.0	67497.9	160.9	15	10.7
				Average	10.9

Therefore, by calculating the final average value, the concentration of GO produced was estimated to be 10.9 mg/ml.

3.5 Deposition of Thin Film

The prepared GO solution from the previous section was used to deposit a thin film using the spin-coating method before deposited with AgNPs on top of the films.

3.5.1 Spin-Coating

The deposition of a thin film using this spin-coating technique can produce a thinner thin film. The value for rotation per minute (rpm) is inversely proportional to the thickness of the thin film. That means a higher value of rpm will decrease the thin films' thickness. However, the GO solution did not show any adherence on the substrate when the rpm was set below 1000 rpm and beyond 1500 rpm. Thus, the rpm value was limited by the ability of the solution to adhere to the substrate. The concentration of the GO solution will also affect the adherence of the solution as well. A Laurell P-6000 spin coater was used in this work.

Figure 3.2 explains the deposition process diagram of using the spin-coating technique to form a GO film on a solid substrate. 20 µL of GO solution was dropped on the pre-cleaned substrate. The spin speed was set at 2000 rpm for 30 seconds to produce an appropriate GO film thickness with good distribution. The prepared GO thin films were then left to dry at room temperature before proceeding with the AgNPs deposition. The parameters for the thin film deposition by spin coating were summarize in Table 3.2.

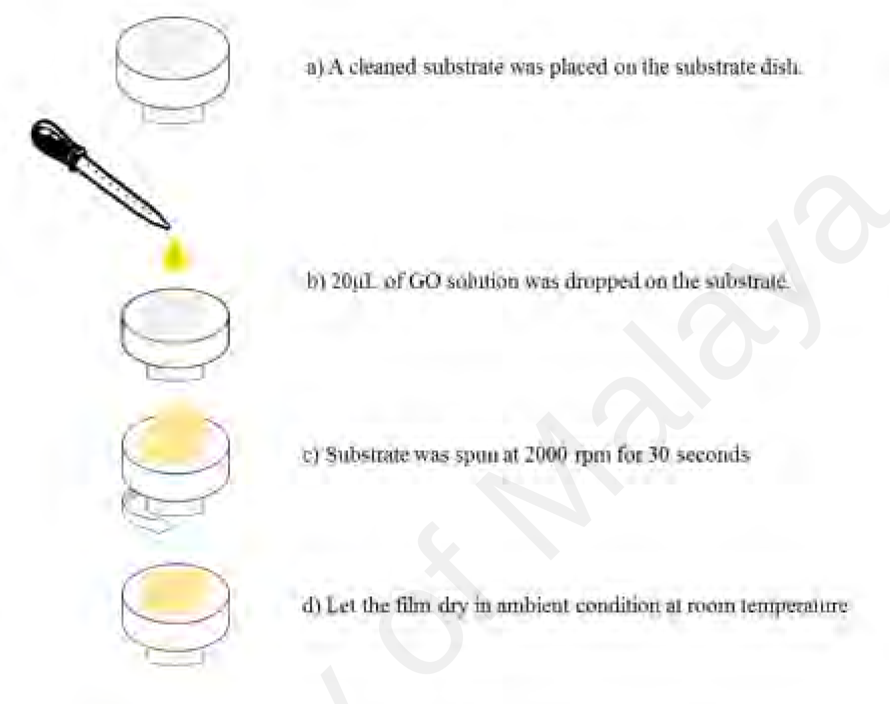

Figure 3.2: Deposition process using spin coating technique.

Table 3.2: Parameters for deposition of graphene oxide thin films.

Parameter	**Value**
RPM	2000
Time	30 seconds
Concentration	1 mg/mL

3.5.2 Hot Wire Chemical Vapor Deposition

The CVD technique used in this work is a homebuilt HWCVD system. The schematic diagram of this system is shown in Figure 3.3. It can be observed that there are several major parts in this system. The main part of the HWCVD system consists of 3 components which are the top plate, body chamber, and bottom plate. These components are made of stainless steel (SS) since it is resistant to corrosive gases besides to avoid any reaction with the process gases. The dimensions for the body chamber are 300 mm in height, 150 mm in diameter and 6 mm in wall thickness. One glass viewport was attached at the center of the body chamber to observe the experiment conditions inside the chamber during deposition. In addition, a stainless steel rotary shaft feed through with a ¼” SS tubing was assembled at the middle part of the top plate as a gas inlet. The feed through was used to support the inside Teflon (insulator) and showerhead (power electrode) connected to the power supply. Aside from that, for the hot filament connection, the electrical feed through which was connected to two electrodes was introduced into the chamber.

The bottom plate was directly connected to a turbo molecular pump and rotary vane pump via a NW 40 SS flexible hose. The vacuum gauges like the pirani and penning gauges were also attached to the bottom plate with an NW 16 connector for pressure detection. The thermocouple, heater, and grounded electrode contact were introduced into the chambers using electrical feed through. The Teflon was used as an insulator at the bottom of substrate holder stand to isolate the holder from the chamber. The configuration of the thermocouple, heater rod and grounded wire to the substrate holder are as shown in Figure 3.3.

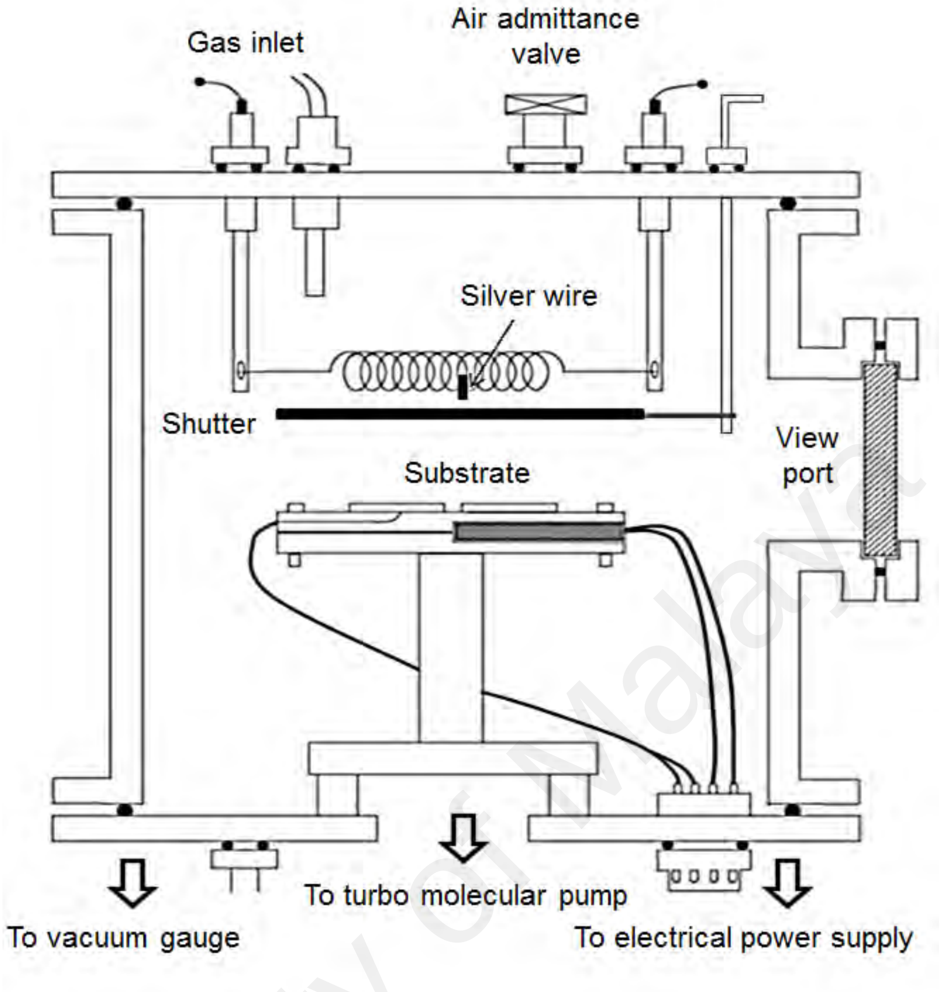

Figure 3.3: Schematic diagram for hot wire chemical vapour deposition (HWCVD).

The substrates were placed onto the top of the substrate holder. Following that, the thermocouple was inserted into a tiny hole located at the edge of the holder and touched exactly the glass substrate to measure the substrate temperature. Then, the DC supply, showerhead, heater rod and regavolt, and the grounded contact of the substrate holder were properly connected. Next, the deposition chamber was tightly sealed prior to the pumping process.

The pumping system is another important part in the HWCVD system. First, a rotary-vane pump (model EDWARDS E2M28) was used to evacuate the deposition chamber to a pressure around 10^{-3} mbar. After that, a gas line cleaning process was performed to ensure that no gases are left in the gas line. Then, to achieve a high vacuum condition of 10^{-5} mbar inside the chamber, a turbo molecular pump (model TURBOVAC TW 70 H) was operated. The minimum pressure recorded was considered as base pressure for the experiment. In this work, two different pressure gauges were used to determine the pressure level inside the chamber for different vacuum levels.

For low and medium vacuum, a TTR 90S Leybold Thermovac Pirani Gauge was used. On the other hand, the Leybold Penningvac PTR 225 was used for high vacuum levels. It is important to note that the valve of the rotary-vane pump connected to the chamber must be closed before opening the valve of the turbo molecular pump. The rotary-vane pump and turbo molecular pump cannot be used simultaneously to evacuate the chamber since their pumping speeds are different and operating them simultaneously will result in the deterioration of vacuum performance. Besides that, these two pumps were connected to a 10 kVA Uninterruptible Power Supply (UPS) to avoid sudden power shut down.

In this work, a thermal evaporation deposition technique using resistive element was adopted as a method to prepare AgNPs. Helices tungsten wire (Edwards, A10 25) was used as a resistive element to evaporate the metal. Silver wire (99.999 %) was hung onto the middle part of the tungsten wire. High current was then flowed through the tungsten wire, making it hot enough to evaporate the Ag wire. After that, the evaporated Ag condensed in the form of a thin film on the substrate surface and on the vacuum chamber walls. The process was carried out in low pressure conditions to avoid reaction between the Ag vapor and atmosphere.

In this way, the mean free path of Ag vapor atoms is in the same order as the vacuum chamber dimensions, so these particles travel in straight lines from the evaporation source towards the substrate without any excess collision with contaminants. Therefore, a more effective evaporation is achieved (Park & Rhee, 2004). For the AgNPs' preparation in this work, some parameters were fixed throughout the work. First, the distance between the tungsten wire and substrates was kept at around 7 cm. Second, the diameter and length of Ag wire were fixed at 0.5 mm and 1 mm respectively. Third, the DC current was constantly set at 6 A.

To get a better control on the thickness of Ag film and thus the morphological properties of AgNPs, the chamber was modified by adding a shutter between the hot filament and substrates as shown in Figure 3.3. As the pressure reached around 10^{-3} mbar, the current supplied to the tungsten wire to around 6 A was slowly increased and the timer for the evaporation process was started. Control of the current can be done by varying the voltage supplied. Normally, bigger and heavier Ag vapor droplets will fall downwards in the beginning of the evaporation process. Thus, the shutter was closed in advance for 1 min. Then, the shutter was opened for the desired time to allow the AgNPs to coat the substrates. The shutter was closed immediately after the deposition based on the varied deposition time. Figure 3.4 shows the flow chart of this experiment. The results obtained will be discussed in detail in Chapter 4.

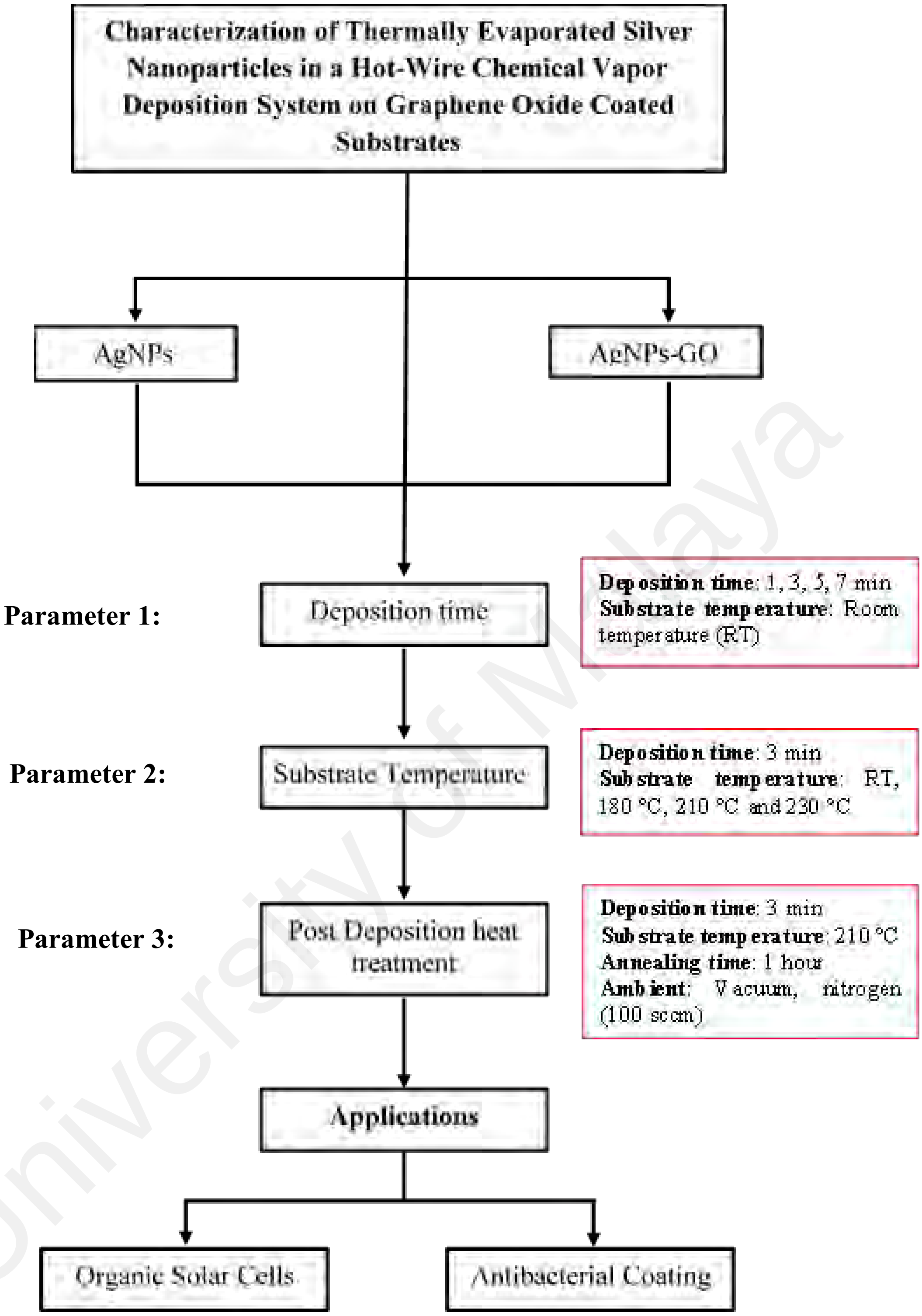

Figure 3.4: Flow chart of the research for the preparation of sample AgNPs and AgNPs-GO and its applications.

3.6 Field Emission Scanning Electron Microscopy

The surface morphologies of the films were investigated by using a field emission scanning electron microscopy (FESEM). A JEOL-JSM-7600F FESEM is used in this work is shown in Figure 3.5 with an acceleration voltage of 5kV. The surface images of the films obtained from this FESEM are very important to understand the morphology and structure of a material.

The FESEM scanning was carried out under high vacuum conditions to flow the electron beam to focus on the sample. These electrons are known as primary electrons which pass through the electromagnetic lenses and deflect to produce a narrow scan beam that bombard the sample. This bombardment leads to different types of electrons to be emitted from the sample. The detector will only capture secondary electrons and construct the image relative to the scanning primary electron beam. The angle and velocity of secondary electrons produced by the surface structure can be processed and captured into an electronic signal by a detector and transferred into an imaging monitor.

Figure 3.5: Picture of JEOL JSM-7600F field emission scanning electron microscope (FESEM).

From the FESEM image obtained, the diameter of the particle was analyzed using imageJ software. The particle size distribution was represented by the histogram graph.

3.7 Ultraviolet-Visible-Near Infrared Spectroscopy

Ultraviolet-visible-near infrared (UV-VIS-NIR) spectroscopy is an important analytical technique used to study the optical properties of thin films. The interaction between light and matter is exploited as the operation mechanism of this technique. The interesting region in electromagnetic (EM) spectrum range between 190 to 2500 nm (UV-VIS-NIR region) can be fully investigated. The light incident towards any medium such as thin film will be either reflected, absorbed or transmitted. As the EM radiation with different energies emitted at any wavelength is temperature dependent of the sample, the tungsten halogen lamp and deuterium discharge tube were used as sources for visible-near infrared and ultraviolet region, respectively.

In this work, the absorption of the film is measured using a Perkin Elmer Lambda 750 UV-VIS-NIR Spectrometer as shown in Figure 3.6. Typically, for absorbance measurements, two quartz slides which will act as reference were inserted in the sample holder. The light was passed through a grating in the monochromater and split into two light paths by a sector mirror. The first light path will be directed through the first quartz slide and the second light path will go through the second glass slide. The transmitted light was detected by photodiodes. The transmitted light from both sides was collected at the photomultiplier before transferred to the amplifier and decoded to the electrical signal. Using software, the signal was then displayed into a spectrum. Besides, the overall operation was also operated using this software. The basic working principle of the instrument was displayed in Figure 3.7. Since quartz was inserted in both sample holders, thereby no changes had been observed to the transmitted intensity. Thus, a baseline was formed which was used as the reference point for other film deposited on the quartz slide.

After the baseline was measured, one of the quartz slides was replaced by sample AgNPs on quartz film. It was scanned in the range 200 nm to 800 nm which is known as the greatest region of the light absorption for noble metal and is called as surface plasmon resonance (SPR). Based on the SPR peak, we can estimate the size, shape and distribution of the nanoparticles.

Figure 3.6: Perkin Elmer Lambda-1050 UV/Vis/NIR spectroscopy.

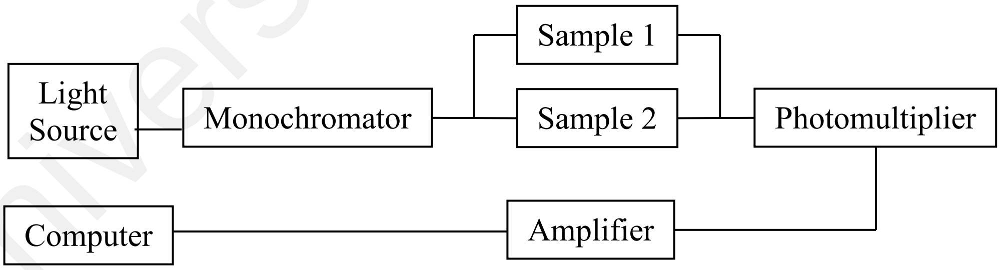

Figure 3.7: Schematic diagram of working principle of UV-Vis-NIR Spectroscopy.

3.8 Raman Spectroscopy

Raman spectroscopy is a study of the interaction between light and matter in which the light is inelastically scattered, or also known as the Raman Effect. As a monochromatic light hits the sample surface, the light can be absorbed, reflected or scattered. In this study, the Raman spectra were obtained using Renishaw in Via Raman

Microscope as shown in Figure 3.8. The sample were excited with a laser power of 10 % with a wavelength of 514 nm (green laser). The measurements were scanned from 1000 to 3200 cm^{-1}. The selection of laser is very important in Raman spectroscopy because each laser will have different penetration depths or otherwise, the sample may not be characterized. From the spectrum obtained, the peaks give information about the molecular structure of the sample. The parameter used in characterizing the film using Renishaw in Via Raman spectroscopy in this work is shown in Table 3.3.

Figure 3.8: Renishaw in Via Raman Microscope.

Table 3.3: Set up parameter for Raman spectroscopy.

Scan range	1000 – 3200 cm^{-1}
Laser power	10%
Exposure time	10 s
Laser	514 nm (green laser)

3.9 Electrical Measurement on Silver Nanoparticles and Silver Nanoparticles on Graphene Oxide

To investigate the plasmonic effect in OSCs, AgNPs and AgNPs-GO were incorporated into the layers of organic solar cell. OSCs were constructed with architectures of ITO/HTL/Active Layer/Al. Devices were fabricated by adding a buffer layer of poly(3, 4-ethylenedioxythiophene): poly(styrenesulfonate) (PEDOT:PSS) on AgNPs or AgNPs-GO coated ITO substrates (∼10 Ω sheet resistance) by employing a spin coating technique at 4000 rpm for 60 s in order to get 40 nm thick films followed by annealing at 120 ºC for 30 min. Subsequently, another layer of poly [N-90-heptadecanyl-2,7-carbazole-alt-5,5 - (40,70-di-2-thienyl-20,10,30-benzothiadiazole)] (PCDTBT): [6,6] phenyl-C71-butyric-acid-methyl-ester ($PC_{71}BM$) which acts as active material was spun onto the sample at 2000 rpm for 20 s to form a 70 nm thickness layer. Aluminum top electrodes were deposited by using thermal evaporation operated at 23 A for 1 min in the vacuum chamber.

The schematic diagram in Figures 3.9 shows the fabrication of the device. Three OSC devices with an arrangement of ITO/GO/AgNPs/PEDOT:PSS/PCDTBT:$PC_{71}BM$/Al, ITO/AgNPs/PEDOT:PSS/PCDTBT:$PC_{71}BM$/Al and ITO/PEDOT:PSS/PCDTBT: PC_{71}-BM/Al were measured using a Keithly 236 Source Measurement Unit (SMU) in a controlled environment. All the processes of fabricating the device were made on the ITO substrates, AgNPs and AgNPs-GO on the ITO to compare the effects on device properties. To eliminate the background light, a black box was used to place the sample holder, the electrical probe and the light source. Characterization under light illumination was done under an Oriel solar stimulator – model 67005 with Air Mass 1.5 filter by standard conditions with a white light irradiation at $100mW/cm^2$ to stimulate the irradiation of light from the sun. The overall measurement was controlled by a personal computer equipped with a LabVIEW system design software.

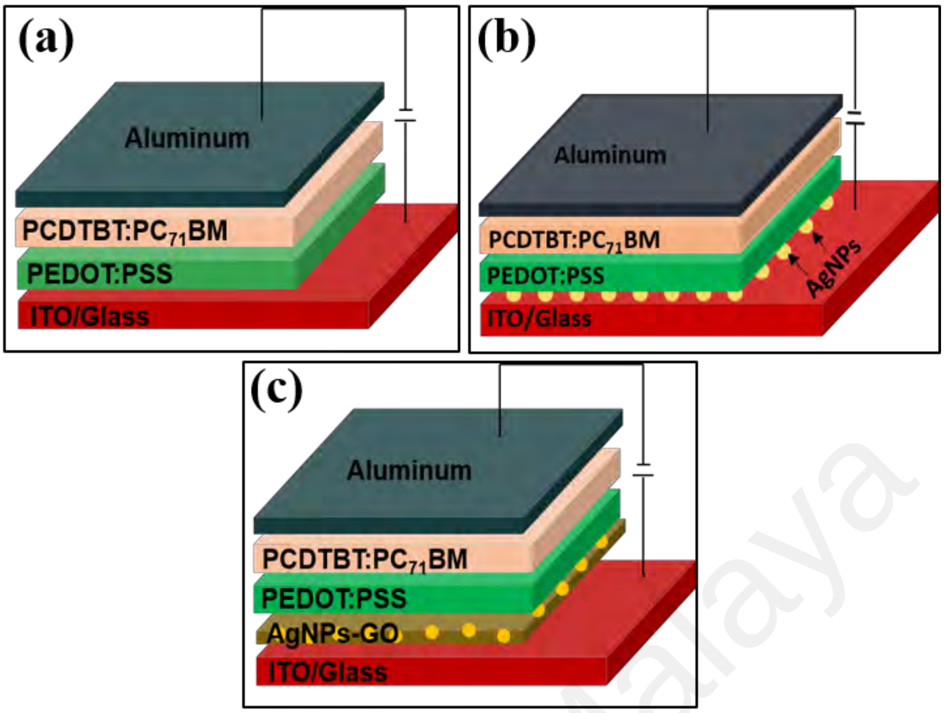

Figures 3.9: Schematic diagram of organic solar cells.

ITO and Al electrodes were connected to the anode and cathode respectively at the SMU before starting the measurement. The voltage was set to be at a range of -1.0 to 1.0 V to detect the photovoltaic effect which appeared at the 4th quadrant of the current-voltage curve. The response time was set to 1 µs so that it matched the typical mobility of electrons in organic material. The software gives the value of current and voltage of the device. The value of current was converted to current density by dividing the measured current to the effective area of the photovoltaic device. The graph of current density against voltage (*J-V*) was then plotted and analyzed. Information about the short-circuit current density and open-circuit voltage can be obtained from this graph. Equation 3.1 is used to calculate the fill factor of the device from the *J-V* graph.

$$\text{Fill Factor, FF} = \frac{J_{max}V_{max}}{J_{sc}V_{oc}} = \frac{P_{max}}{J_{sc}V_{oc}} \tag{3.1}$$

$$\frac{P_{max}}{P_{in}} = \frac{J_{sc}V_{oc}}{100\ mW/cm^2} \tag{3.2}$$

Where J_{max}, V_{max}, J_{SC}, and V_{OC} are maximum current density, maximum voltage, short-circuit current density and open-circuit voltage, respectively.

3.10 Antibacterial Testing of Silver Nanoparticles and Silver Nanoparticles on Graphene Oxide

To investigate the antibacterial efficiency of GO, AgNPs and AgNPs on GO coated glass, an agar diffusion method was used to test the prepared samples according to the Clinical and Laboratory Standards Institute (CLSI) guidelines (Steinkraus et al., 2007). The antibacterial test was performed on two strains, including Gram negative *Escherichia coli* (*E. coli)* (ATCC 25922) and Gram-positive *Staphylococcus aureus* (*S. aureus*) (ATCC 6538) (Gribbles Pathology Lab, Petaling Jaya). Selected strains were grown overnight on blood agar plates. The inoculums were prepared by diluting with saline and the turbidity was adjusted to 0.5 McFarland standards using broth. Then, the colonies were streaked on Mueller Hinton agar plates and the AgNPs and AgNPs on GO coated glass that was placed on the culture using sterile forceps. Following this, cultured plates were incubated overnight in an incubator at 35-37 °C After incubation, each sample and its surrounding agar area was photographed using a 16-megapixel digital camera (Canon A3300IS). Images of each tested plates and its surrounding agar area were analyzed to measure the zones of inhibition (mm). Mean zones of inhibition of the microorganisms were then calculated. Figure 3.10 shows the measurements of the zone of inhibition of bacteria.

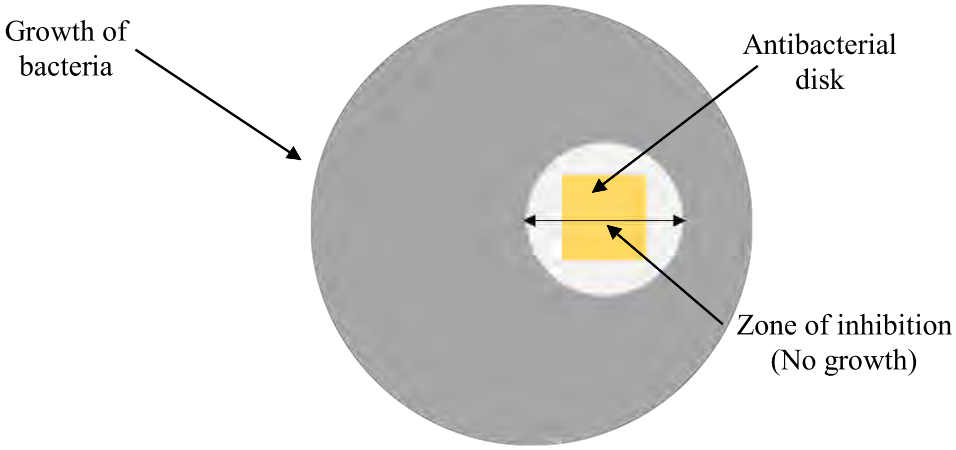

Figure 3.10: The measurement of zone of inhibition of bacteria.

CHAPTER 4: RESULTS AND DISCUSSION

4.1 Chapter Overview

In this study, AgNPs are grown on bare and GO coated quartz substrates. The AgNPs on GO (AgNPs-GO) coated quartz substrates are prepared using a two-step method which involves spin coating of GO grown by Hummers method on quartz substrates followed by the growth of AgNPs by evaporation of Ag wires placed on the hot-filament of tungsten wire in a hot-wire chemical vapour deposition (HWCVD) set-up onto the GO coated quartz substrates. The latter technique is used to directly grow the AgNPs on bare quartz substrates for the AgNPs samples on bare quartz substrates.

The HWCVD system is incorporated with a shutter to control the exposure time of the substrate to the hot-filament prior to deposition. This is to minimize impurities from initial evaporation of the Ag wires from the samples. The shutter time that is the time duration the shutter covers the substrate at the onset of the filament heater being turned on is fixed for 1 minute for all samples. In this work, the effects of three growth parameters are studied with respect to the morphology, surface plasma resonance (SPR) and microstructural properties are studied. The growth parameters studied are deposition time of AgNPs and substrate temperature (T_S). The effects of post-annealing of these AgNPs in vacuum and N_2 ambient are also investigated. The results obtained are analyzed and discussed and the sequence of the flow of this work experiment is presented in the flowchart in Figure 3.4 in previous chapter.

The AgNPs are characterized using FESEM, UV-VIS-NIR spectrophotometer and Raman scattering spectrometer set-up. The morphology of the AgNPs are studied from the FESEM images while the microstructural properties of the AgNPs-GO films are analyzed from the Raman spectra. The UV-VIS-NIR spectrophotometer are used to study the SPR properties of the AgNPs on bare and GO coated quartz substrates.

4.2 Preliminary Study on the Growth of AgNPs by Thermal Evaporation

The growth of AgNPs and AgNPs-GO were done by thermal evaporation method using home built HWCVD system. The deposition process by this method involved few parameters to produce a NPs at a particular size. A preliminary experiment was done to determine the effects of the Hydrogen (H_2) gas introduction into the HWCVD system to the growth of AgNPs.

Two deposition experiments were setup to study the effects of AgNPs growth with and without the H_2 flow. The deposition of AgNPs was fixed for 3 minutes in a high vacuum of 10^{-5} mbar. The optical absorbance of the as-deposited samples with and without H_2 flows was observed using UV-Visible spectroscopy. Ag at nanoscale exhibits optical absorbance known as SPR which absence in bulk Ag. The position, width, and intensity of SPR peak can be used to predict the structure of the as-deposited Ag film. Figure 4.1 shows the optical absorbance of the as-deposited sample deposited in high vacuum with and without H_2 flows. Without H_2 flow, the optical absorbance spectrum shows two peaks at 250 and 535 nm. The appearance of these two-different peaks in the optical spectrum indicates a flat, non-uniform and anisotropic shape of particles were formed. Meanwhile, for the sample deposited in H_2 ambient, only one peak appeared at 420 nm. The appearance of the narrow single peak is attributed to spherical NPs. A high aspect ratio and isotropic shapes of NPs result in narrowing of the width of localized surface plasmon band. The blue-shift of the SPR peak position is due to the uniform size distribution of Ag islands, more spherical shape particles with larger aspect ratio and reduction of surface coverage.

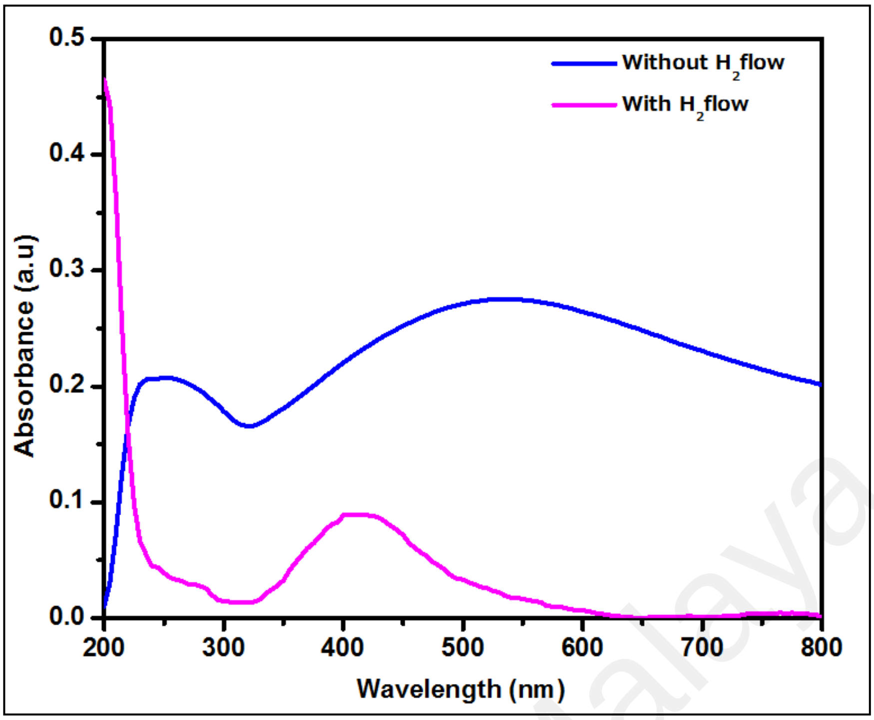

Figure 4.1: Optical absorbance of the sample without and with Hydrogen flow.

H_2 flow during deposition plays an important role in the formation of AgNPs. The introduction of H_2 gas has introduced an environment within the Ag wire evaporation zone which reduced the amount of the oxygen presented in the HWCVD system. H_2 gas has created surface passivation on quartz substrate thus removing dangling bonds and therefore prevent the formation of oxide particles. The growth of the spherical shape particles may be due to the absence of oxides acting as diffusion barriers leading to better particle growth (Lee et al., 2017).

This preliminary result has shown the importance of H_2 gas flow in the system during the deposition process which can produce a more uniform size distribution and shape of NPs. Therefore, the H_2 gas flow of 50 sccm is set as a fixed parameter for all deposition setup. To optimize the parameter for the AgNPs growth, the deposition time, substrate temperature and the post-deposition effects were studied which will be discussed in the next subtopic.

4.3 Effects of Deposition Time of Silver Nanoparticles

In this section, the effects of deposition time of Ag wire on the morphology, structure and optical properties of the AgNPs are investigated. Two sets of AgNPs consisting of AgNPs and AgNPs-GO are studied in this work. The GO suspension prepared by Hummer's method were then deposited onto quartz substrates using the spin coating technique. The AgNPs are grown in a HWCVD set-up by evaporating Ag wire placed on a tungsten filament in H_2 gas ambient shown in Figure 3.3. The AgNPs were grown at a different deposition time of the Ag wire. The effects of deposition time on morphology, structural and optical properties of AgNPs will be analyzed and discussed in the next subsections.

4.3.1 Morphological Analysis of AgNPs and AgNPs-GO at Different Deposition Time

Field emission scanning electron microscopy (FESEM) images of the AgNPs are used to study the morphology of these NPs. Figures 4.2 (a), (c), (e) and (g) show the FESEM images of the AgNPs while Figures 4.2 (b), (d), (f) and (h) show the histogram of the particle size distribution grown at different deposition times. The duration of deposition time of the Ag wire shows significant influence on the size of the AgNPs. The FESEM image of AgNPs at a deposition time of 1 minute clearly shows the formation of smaller NPs of different sizes compared to the NPs deposited at longer deposition times. Increase in deposition time to 3 minutes shows the formation of more symmetrically shaped NPs of larger sizes. With further increase in deposition time to 5 minutes, the NPs appear to agglomerate with neighboring NPs leading to the formation of larger and unsymmetrical shaped NPs. AgNPs grown at deposition time 7 minutes shows an increase in agglomeration resulting in the formation of elongated NPs.

The histogram plots of AgNPs sizes grown at deposition times of 1, 3, 5 and 7 minutes are calculated using the Image-J software. A Gaussian curve was fitted to determine the average values of the nanoparticle size. The Gaussian curves are shifted towards larger particle size with the increase in deposition time. The NPs sizes range between 7 nm to 38 nm depending on the deposition time of the AgNPs. The smaller size of the AgNPs varying from 7 to 16 nm with the average of 9 nm was obtained from the FESEM image of AgNPs deposited at 1 minute. The image shows the formation of a base layer of very closely spaced smaller NPs with sparsely distributed larger NPs on top of this layer. The low sticking coefficient of the AgNPs to the quartz substrate is due to the high surface tension of the quartz substrate to the NPs has contributed to the formation of the base layer of small spherically shaped AgNPs (Gromov et al., 2015). The lower surface tension between the AgNPs increases the sticking coefficient of the newly formed NPs on the base layer and increases agglomeration between adjacent NPs formed above the base layer (Bai et al., 2016).

However, the short deposition time only allows less time for agglomeration of AgNPs thus the AgNPs formed are small. It can be observed here that the NPs formed above the base layer become more anisotropic in shape due to the agglomeration of closely spaced adjacent NPs. When the deposition time is increased, the number of Ag atoms reaching the substrates increases thus the base layer is covered with a high density of closely packed larger NPs. Stacking of NPs also occurs as oncoming Ag atoms are stacked on top of the NPs formed. This result in the increase in the average size of the NPs in the sample grown for 3 minutes to 12 nm. Enhanced stacking and agglomeration of NPs result in the formation of anisotropic shaped AgNPs in the samples grown at longer deposition times of 5 and 7 minutes with the average size of the AgNPs increasing to 20 nm and 29 nm respectively.

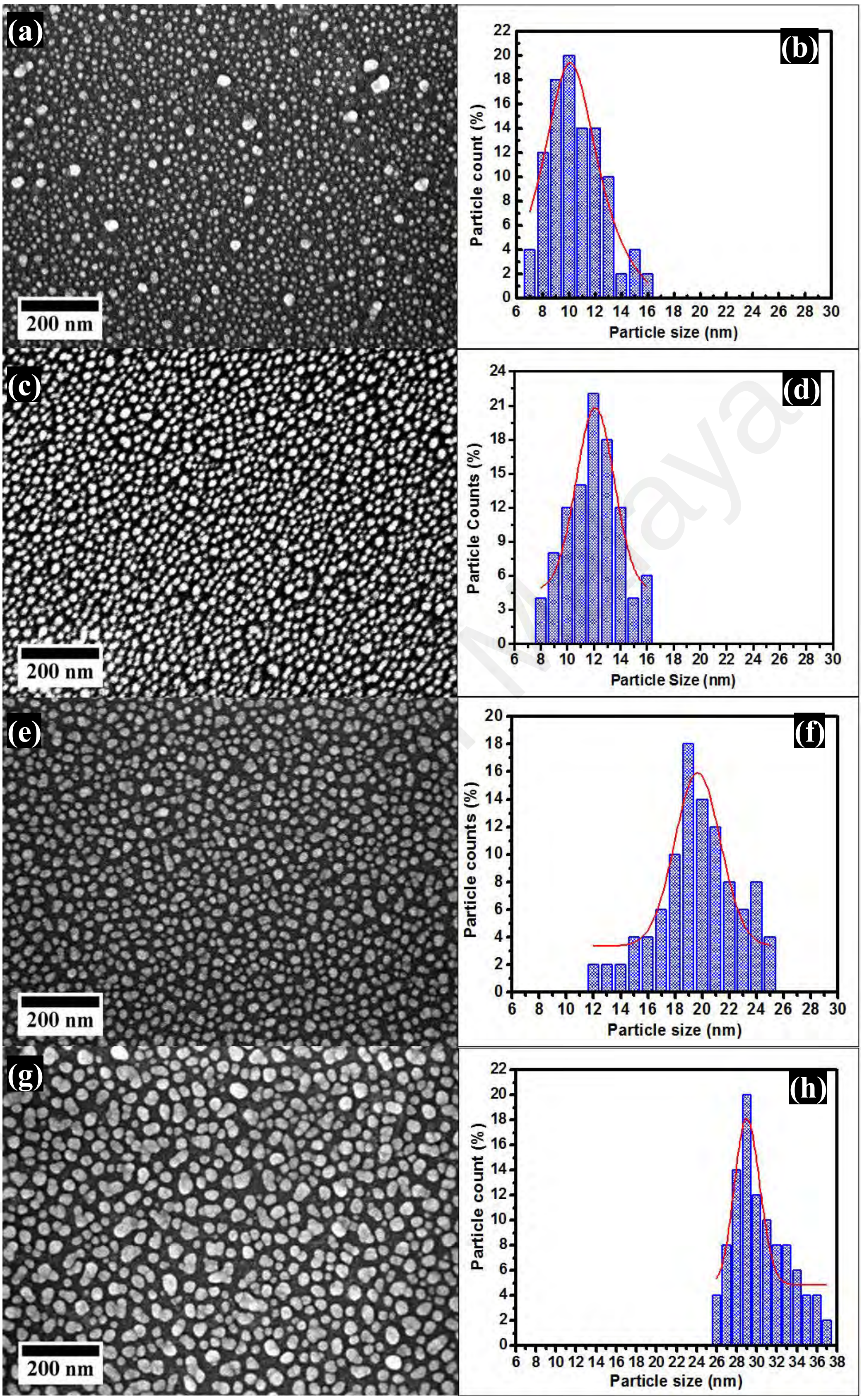

Figures 4.2: FESEM images (a), (c), (e) and (g) and the distribution size (b), (d), (f) and (h) for AgNPs deposited on quartz substrate at 1, 3, 5 and 7 minutes deposition time.

The FESEM images and histogram of the particle size distribution grown at different deposition times for AgNPs-GO were presented in Figure 4.3. At 1 minute deposition time, the FESEM image shows that the bottom layer NPs deposited on GO are smaller in size and finely distributed with a higher particle density. The AgNPs formed in the base layer are spherical in shape and isotropic with average size of 8 nm. Sparsely distributed larger AgNPs are formed above the base layer. The wrinkles seen below the base layer shows the existence of GO films. As the time is increased to 3 minutes, a distribution of spherically shaped AgNPs of the average size of 14 nm is formed with larger clusters of loosely packed AgNPs formed on top of it in consequence of the stacking of the evaporated Ag atoms on reaching the growth sites. However, the growth of AgNPs is accompanied by the large size of agglomerated NPs of average size 36 nm. The GO wrinkles are still observable even though they are covered with larger AgNPs layer. Longer deposition time results in an increase in the size of the NPs and the shape becomes isometric due to the longer exposure time to the hot filament. The completion of evaporation of the Ag wires stops the increase in the size of the NPs. The NPs size is increased to 22 nm and 24 nm for the samples grown 5 and 7 minutes respectively. In the images of these samples, the GO wrinkles are not visible but appear as crumples of wave-like background with NPs on the top of it.

The trend of the variation in the size of the NPs can be observed in a histogram of Gaussian shaped particle size distribution as shown in Figure 4.3 (e), (f), (g) and (h). The narrow FWHM of Gaussian curve for all samples indicates that the variation in the size of the AgNPs on the GO coated substrate is small. The shift of the fitted curve for samples of AgNPs-GO grown at 1 minute to 7 minutes deposition time showed similar trends with samples AgNPs grown on a bare quartz substrate. The calculated average NPs size is almost similar in the range between 7 to 32 nm with the calculated size of 9 nm, 13 nm, 19 nm and 24 nm correspond to samples grown at 1, 3, 5 and 7 minutes of deposition time.

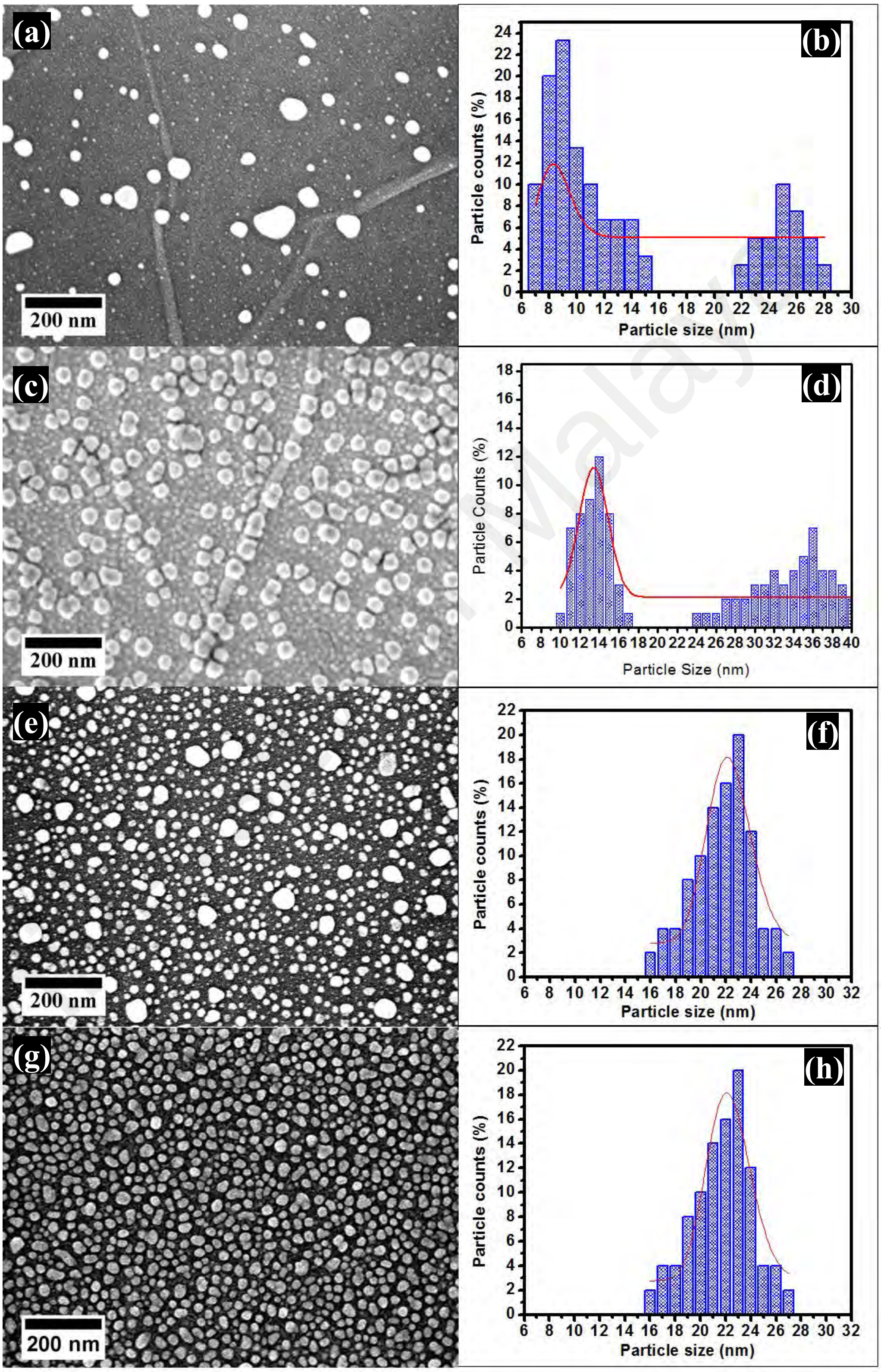

Figure 4.3: FESEM images (a), (c), (e) and (g) and size distribution (b), (d), (f) and (h) for AgNPs-GO grown on quartz substrate with deposition times of 1, 3, 5 and 7 minutes.

Figure 4.4 summarizes the growth behavior of the AgNPs on bare and GO coated quartz substrates with respect to the deposition time. The surface of the GO coated quartz substrate has higher surface tension to the AgNPs formed compared to the quartz substrate thus is more hydrophobic to the AgNPs. Initial growth of the AgNPs on bare and GO coated AgNPs is strongly dependent on the surface of the substrates. The oxygen (O) atoms in the bare quartz substrates are covalently bonded to the silicon (Si) atoms in the quartz thus the surface is almost free of charges. The sticking coefficient and the surface tension of the surface of the substrate to the evaporated Ag atoms are important factors in the growth of AgNPs at the surface. On the other hand, positively charged Ag+ ions can be easily attached to the negatively charged O functional groups of the GO as described by Lan et al, 2014.

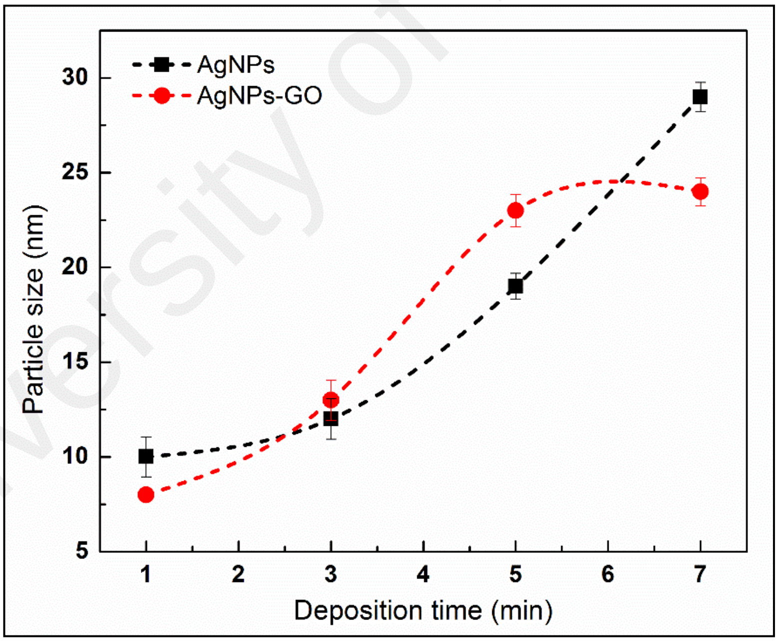

Figure 4.4: The variation of AgNPs size on bare and GO coated substrate.

The initial growth of AgNPs basically is due to AgNPs anchored to the surface of the GO nanosheets based on this mechanism. Thus, this explains the smaller size of the AgNPs deposited on GO coated substrates compared to the AgNPs deposited on bare quartz substrates when deposited for only one minute. The low sticking coefficient of the

AgNPs to the bare quartz substrates forces the NPs to be formed first and agglomeration between NPs increases the NPs sizes and this increases the sticking coefficient of the NPs. The initial AgNPs on the GO coated quartz is formed through anchoring of the positively charge Ag ions to the sites of negative charged O functional groups on the GO. This explains the smaller size and fine distribution of the AgNPs at the base layer for the NPs grown on GO coated substrates when deposition time is only 1 minute. However, when exposed to longer growth time, the AgNPs deposited on bare quartz substrate agglomerate to form larger particles NPs while the increase in NPs size for the NPs grown on GO coated quartz substrate is through the accumulation of Ag atoms on the AgNPs anchored at negative charged O functional groups on the surface of the GO nanosheets.

The size of AgNPs grown on GO coated quartz increases at a faster rate compared to the NPs grown on bare quartz substrate when the deposition times are 3 and 5 minutes suggesting agglomeration of AgNPs increases the size of AgNPs at a slower rate compared to the accumulation of Ag atoms on anchored NPs on the substrate. However, the size of the AgNPs on the GO coated quartz substrate saturates at 5 minutes deposition while the AgNPs on bare quartz substrate continues to increase with deposition time. The longer exposure time to the heated filament enhances agglomeration of the AgNPs in consequences of thermal effects but does not have an effect on the size of NPs anchored to specific points on the substrate. Thus, the growth of AgNPs on GO coated quartz substrate is capable to control the particle shape and size of NPs just by increasing the deposition time to point the NP size reaches saturation.

4.3.2 Surface Plasmon Resonance Studies on AgNPs and AgNPs at Different Deposition Time.

SPR is a prominent spectroscopic feature of noble metal NPs. The sharp, intense absorption band in the visible range in the optical absorbance spectra is the result of collective resonant oscillations of free electrons in the conduction band of the AgNPs with the incident photons. The conduction band (C_B) and valence band (V_B) of AgNPs are very close to each other thus these AgNPs have a significant presence of free electrons. The SPR peak is the result of collective oscillations of electrons resonating with the frequency of the light wave. The intensity and wavelength of the SPR peak have been shown to be dependent on the number, size, and shapes of the AgNPs.

The absorption of AgNPs on the quartz at different deposition times was illustrated in Figure 4.5. The background effects of the quartz substrate, in terms of its absorption, are subtracted from the raw optical measurements. The wavelength at the maximum intensity of plasma resonance band is called the SPR wavelength (λ_{SPR}) and is a characteristic of the AgNPs formations. It has been reported that AgNPs of diameter less than 100 nm produces SPR absorption band in between 370 and 600 nm (Amendola et al., 2010). A broad non-symmetric absorption band in this region with the λ_{SPR} were red-shifted approximately from 425 nm to 455 nm wavelength with an increase in deposition time. The non-symmetric band shows that the shapes of the NPs are anisotropic.

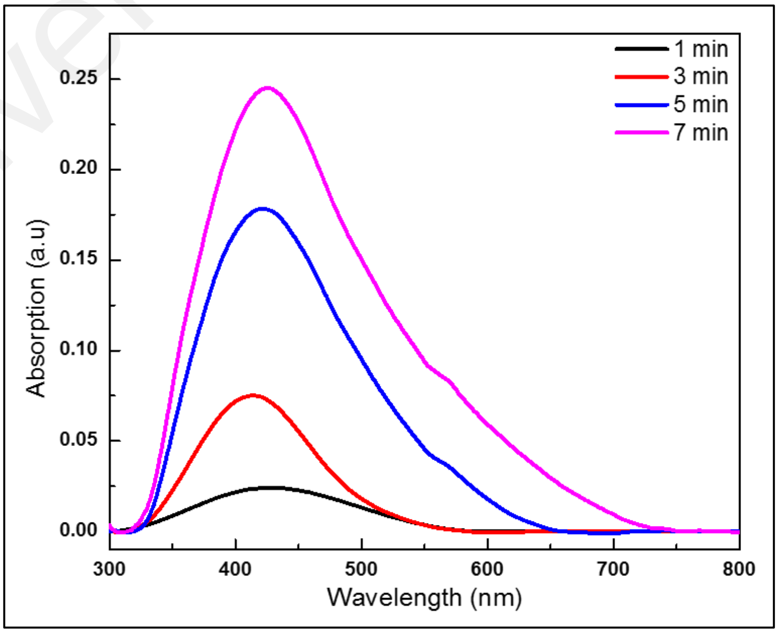

Figure 4.5: Absorption spectra of AgNPs varied deposition time at 1, 3, 5 and 7 minutes.

Al-Ghamdi et al and Noguez recorded that spherical shape AgNPs produce one symmetric SPR peak at 515 nm, triangular shaped AgNPs produce two peaks at 396 and 695 nm and cubic AgNPs produce 6 peaks at 630, 490, 420, 375, 362 and 340 nm. Thus, the broad non-symmetric absorption SPR band produces by the AgNPs on bare quartz substrates are due overlapping of bands of cubic, triangular and spherical NPs (Al-Ghamdi & Mahmoud, 2013; Noguez, 2007). At longer deposition time, increase in the SPR band intensity indicates the presence of higher density of AgNPs.

The λ_{SPR} for AgNPs grown for 1 minute is at 420 nm but increase the growth time to 3 minutes results in a blue shift of λ_{SPR} to 415 nm. However, increase in deposition time to 5 and 7 minutes has redshifted the SPR peak to 421 nm and 426 nm respectively. SPR is very sensitive to the changes in the particles size, particles shapes, and the surrounding media. For this experiment, the surrounding media was constant. Thus, it can be concluded from FESEM images and absorption spectra in Figures 4.2 and Figure 4.5, the variation of AgNPs size produces the most significant effect on the λ_{SPR}.

As a consequence of the increasing NPs size, the SPR position was red-shifted. The blue-shift in the SPR peak wavelength when the deposition time was increased from 1 to 3 minutes can be related to NPs formation. The NPs formed at a deposition time of 1 minute is mostly formed on the bare quartz substrate and the interparticle distance is larger thus the surrounding media has a measurable influence on the SPR effect on the λ_{SPR} (Kamakshi et al., 2017). The AgNPs deposited for 3 minutes are larger in size but the compactness in the distribution of the NPs decreases the influence of the surrounding media and the blue-shifts the λ_{SPR}. Increase in deposition time to 5 and 7 minutes, the red-shift of λ_{SPR} is more related to the increase in NPs size where the increase in NPs size increases the λ_{SPR}.

The absorption spectra of GO and AgNPs-GO at different deposition times is shown in Figure 4.7. The absorption spectrum of the GO films shows the appearance of the absorption peak at 230 nm. With the deposition of AgNPs on top of GO films, two absorption bands are present which correspond to the GO films and the second band is attributes to the AgNPs. The GO characteristic peak is shifted to 245 nm when AgNPs are incorporated on the surface of the GO. This peak shifting is believed to be due to the thermal effect induced by the hot filament used as the heating element to evaporate Ag wire. This thermal effect may remove some functional groups on the surface of the GO. The second SPR band of these samples deposited at different deposition times are within the same wavelength as the AgNPs on bare quartz substrate but are slightly red-shifted compared to the AgNPs on bare quartz substrates.

The appearance of second peak as observed in Figure 4.7 is the SPR characteristic of the AgNPs. This λ_{SPR} for the samples deposited at 1, 3, 5 and 7 minutes are positioned at 420 nm, 425 nm, 435 nm and 455 nm to respectively. The increase in the SPR band intensity shows an increase in the density distribution of the AgNPs. The SPR position is red-shifted with the increase of deposition time denoting the increase in particle size.

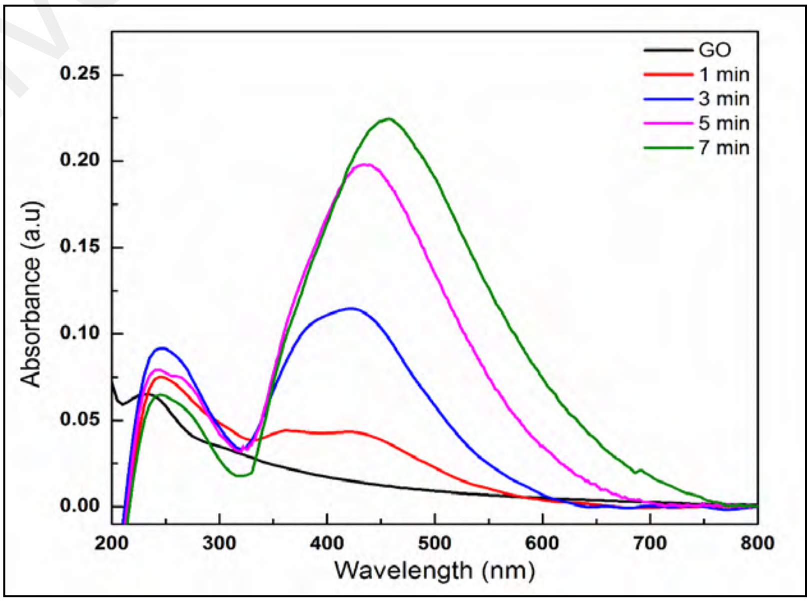

Figure 4.6: Absorption spectra of AgNPs-GO at deposition time at 1, 3, 5 and 7 minutes.

The variation of SPR peak position, λ_{SPR} for AgNPs on bare quartz and GO coated quartz substrates at 1, 3, 5 and 7 minutes of deposition time. The λ_{SPR} of AgNPs on GO is red-shifted with respect to the AgNPs on a bare quartz substrate. A red shift of λ_{SPR} is observed at the higher refractive index of surrounding media. Mahmoud et.al reported that a redshift of λ_{SPR} was observed due to the higher refractive index of surrounding media (Mahmoud et al., 2012). Since the refractive index of GO is higher than bare quartz this may have resulted in the red-shift of SPR peak position (Jung et al., 2008). Meanwhile, the λ_{SPR} of AgNPs is tunable with respect to the particle size within the same surrounding media. AgNPs size shows an increment with increasing deposition time. Increase in AgNPs size shifts the λ_{SPR} to a longer wavelength.

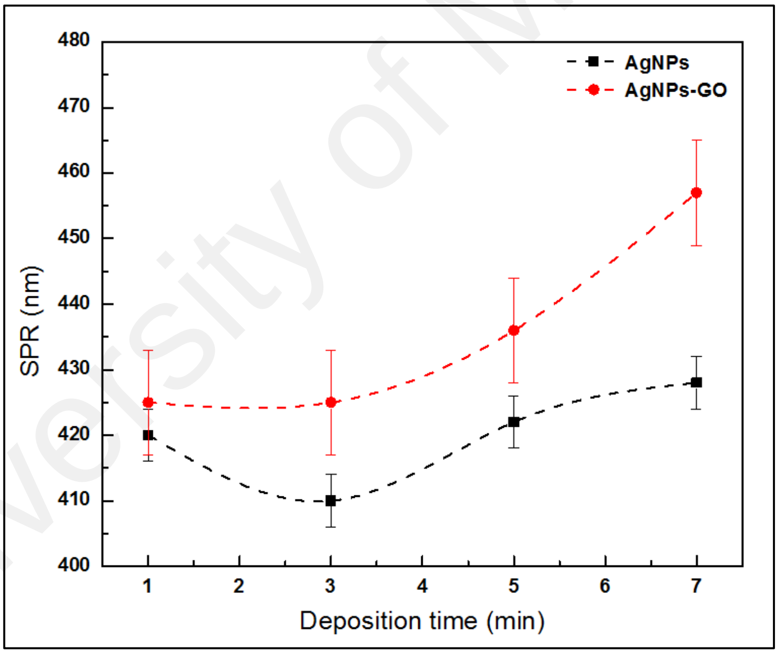

Figure 4.7: SPR variation of AgNPs and AgNPs-GO at 1, 3, 5 and 7 minutes.

The full width half maximum (FWHM) of the λ_{SPR} can provide more information on the formation of AgNPs with respect to the deposition time. The FWHM of the SPR band is calculated using Origin Pro 8.1 software. According to the Mie theory, when the system is monodispersed, the peak shape is symmetric and the value of the FWHM is small. When the system is poly-dispersed, the peak shape is asymmetric, which suggests that the peak actually consists of two or more absorption peaks of different species (Shahriary et al., 2015).

The variation of the FWHM of the λ_{SPR} of the AgNPs and AgNPs-GO with respect to deposition time are presented in Figure 4.9. The FWHM of the λ_{SPR} shows similar trends with an increase in deposition time as the FWHM of the Gaussian fitted histogram of the NPs size. The FWHM decreases to a minimum for the sample of AgNPs deposited for 3 minutes and increases with increase in deposition time. The AgNPs are poly-dispersed during the initial part of the deposition process as sticking coefficient of the AgNPs to the substrates is lower compared to the base AgNPs layer. This results in the formation of AgNPs of varied shapes and sizes but since the histograms in Figures 4.3 and 4.4 only record sizes, it can be concluded that the NPs are formed with varied sizes during the initial part of the deposition. A deposition time of 3 minutes is ideal for the formation of homogeneous shaped AgNPs on both substrates. This deposition allows the formation of AgNPs compact layer as a base for incoming Ag atoms to anchor on. Since the time is not long enough for active agglomeration and accumulation process of AgNPs thus the NPs formed are even in sizes. The FWHM increases with increase in deposition time especially for the AgNPs on GO coated quartz. This indicates that the agglomeration process active for AgNPs on bare quartz substrates can control the size and distribution of the AgNPs while continuous accumulation process of Ag atoms on AgNPs formed without agglomeration results in NPs of varied sizes (Li et al., 2002).

The variation of SPR peak intensity for AgNPs and AgNPs-GO at different deposition time are shown in Figure 4.9. It can be observed that both samples showed the same trends. Increasing amount of AgNPs will enhance the SPR peak. There is not much difference between both set samples. The intensity of SPR mainly affected by the particles density and size. SPR spectra show the most intense peak at 7 minutes deposition time suggesting that higher number of absorbing particles exists.

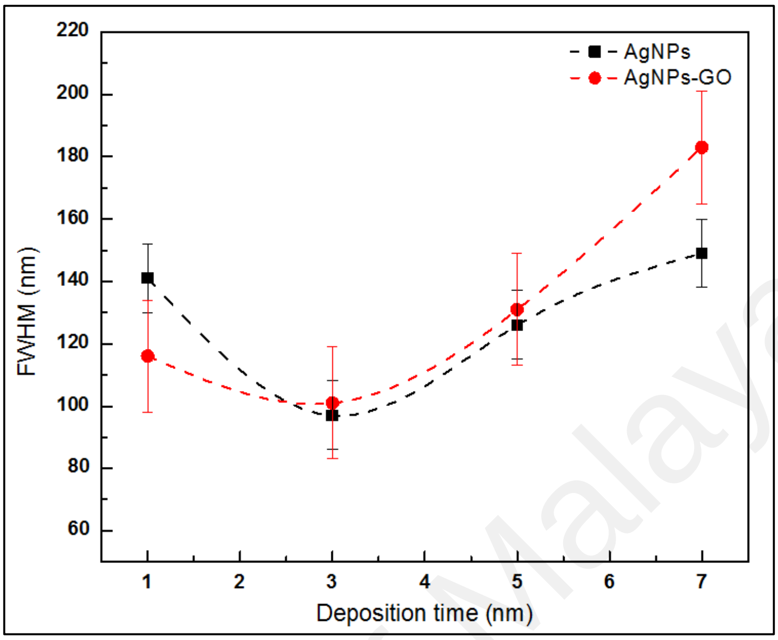

Figure 4.8: The variation of FWHM of absorption peak for AgNPs and AgNPs-GO.

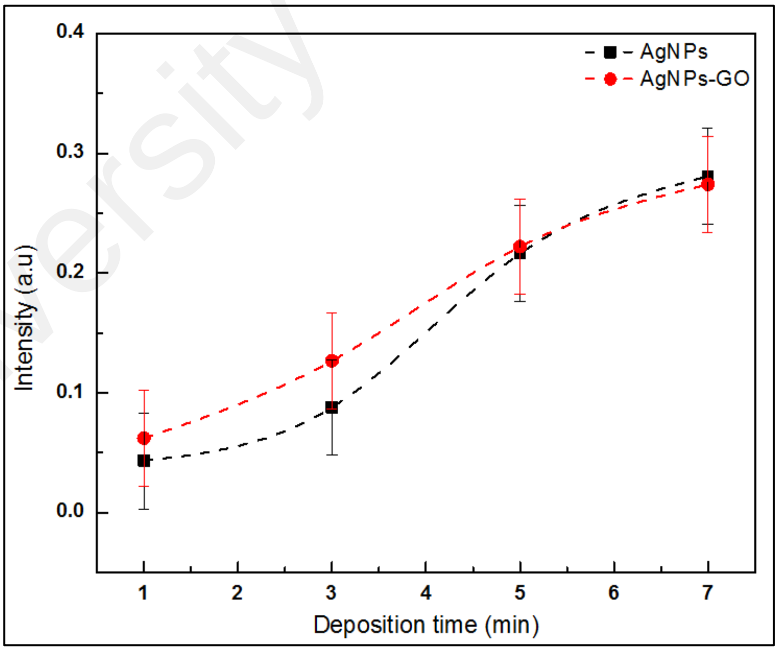

Figure 4.9: SPR intensity of AgNPs and AgNPs-GO at varied deposition time.

From morphology, structural and optical study, AgNPs deposited at 3 minutes was considered as the optimize samples. AgNPs is most stable for this parameter considering the morphology, structural and optical properties. At 3 and 5 minutes, almost the same value of FWHM is yielded but further increase to 7 minutes resulting in broad FWHM.

4.3.3 Raman Spectroscopies Studies on AgNPs-GO at Different Deposition Time

The Raman spectra for AgNPs-GO grown at different deposition times of 1, 3, 5 and 7 minutes are shown in Figure 4.10. The spectrum of the GO coated quartz substrate is included as a comparison for this discussion. The first two Raman peaks (corresponding to the D and G peaks) are fitted with Lorentzian curve fit while the second set of peaks (corresponding to the 2D and D+G peak) are fitted with Gaussian curve fit. Generally, the position and shape of the 2D peak are highly sensitive to the number of graphene layers and has been used to distinguish the single-layer from few-layer graphene. However, in our study, it is not possible to determine the number of the layer in the GO thin film since the GO nanosheets were spin dried on a quartz substrate to prepare a thin film.

The Raman spectrum of the GO coated substrate with and without the AgNPs shows the two major bands ranging from 1200 cm^{-1} to 1700 cm^{-1} wavenumber, corresponding to the well-documented D and G bands. In this work, the analysis is done only on the D and G bands. The D peak is due to A_1g mode breathing vibrations of the sp^2 carbon rings and is Raman active at the graphitic edges, which are absent in defect-free graphite carbon (Hong et al., 2013). Therefore, the D peak indicates the presence of defect induced by a grain boundary and in the GO coated quartz substrate, it could be due to the incorporation of oxygen atoms within the graphene matrix. Meanwhile, the G band is assigned to the E_{2g} mode of sp^2-bonded carbon atoms (Hong et al., 2013). Raman signals of GO in such hybrid films can be enhanced by the presence of AgNPs within the graphene structure displaying surface-enhanced Raman scattering activity. The number, size, and shape of AgNPs attached on the GO sheets can affect the degree of enhancement of Raman signals in AgNPs on GO coated quartz substrates.

The Raman spectra in Figure 4.10 are used to investigate the effects of AgNPs deposition time on the GO coated quartz substrate. It is observed that immobilization of AgNPs on the GO film results in a noticeable increase in the intensity of the D band and G band and slight broadening and narrowing of the D and G bands respectively. The increase in the Raman scattering is approximately one order of magnitude and can be attributed to the surface-enhanced Raman scattering (SERS) effect. The higher density of AgNPs leads to higher intensity of Raman signals (de Faria et al., 2014).

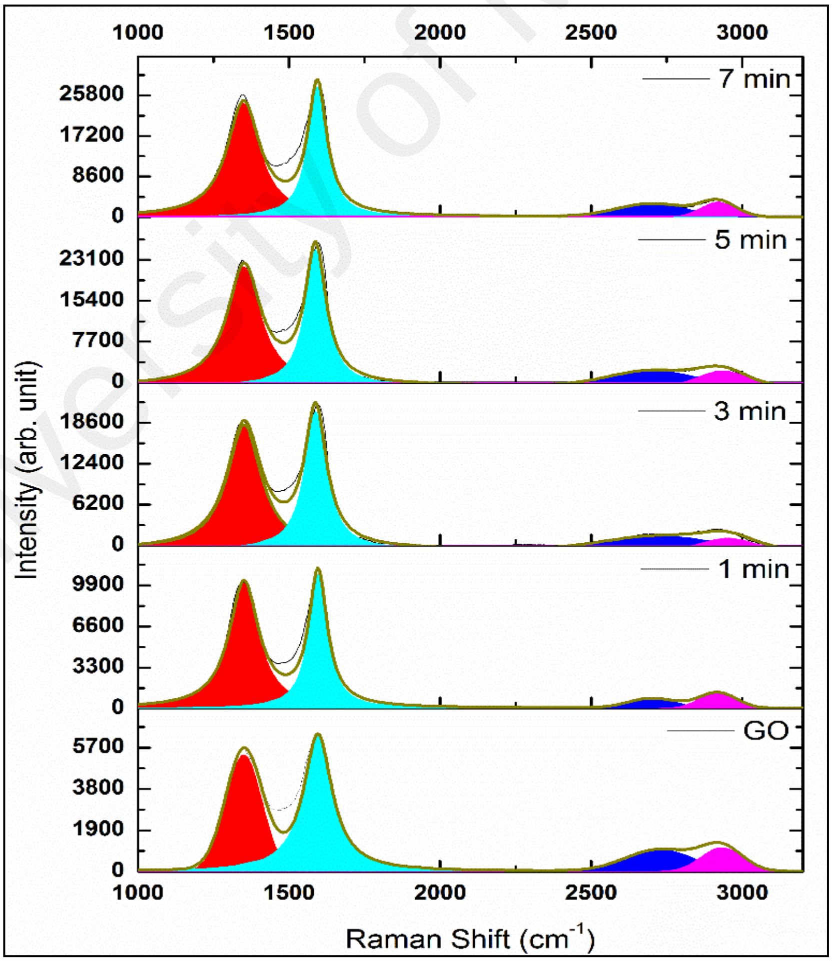

Figure 4.10: Raman spectra of GO and AgNPs deposited on GO deposited at 1, 3, 5 and 7 minutes.

Table 4.1 shows the peak position of the D and G peak of GO coated quartz substrates without and with AgNPs grown at a different deposition time of 1, 3, 5 and 7 minutes. The immobilization of AgNPs on GO surface has shifted the D peak position from 1352 cm^{-1} to 1350 cm^{-1} for the AgNPs deposited for 1 minute on the GO coated quartz substrate. Increase in amount of AgNPs in the AgNPs-GO sample deposited for 3 and 5 minutes, the D peak is further blue-shifted to 1346 cm^{-1}. This blue-shift in this D-peak position is due to the electromagnetic interaction between GO and AgNPs. The immobilization of AgNPs on GO structure may have contributed to the blue-shift in the D-peak position a result of the formation of sp^2 bonds. However, when the deposition time is increased further to 7 minutes, the D-peak position is red-shifted to 1348 cm^{-1} which can be assigned to further formations of defects in GO structure.

Table 4.1: Peak position of D and G peak of AgNPs-GO deposited at 1, 3, 5 and 7 minutes.

Sample	**D (cm^{-1})**	**G (cm^{-1})**
GO	1352	1597
AgNPs-GO 1 minute	1350	1597
AgNPs-GO 3 minute	1346	1595
AgNPs-GO 5 minute	1346	1596
AgNPs-GO 7 minute	1348	1596

The G-peak position for GO coated quartz substrate is observed at 1597 cm^{-1}. The G peak position shows a very small blue-shift but also produces similar trend as the D-peak position. The G-peak position of the AgNPs-GO is shifted to smaller wavenumber with the immobilization of AgNPs from 1597 cm^{-1} to 1595 cm^{-1} for the samples with the AgNPs deposited at 1 and 3 minutes. Increase in a deposition time of the AgNPs to 5 and

7 minutes shifts the G peak back to a larger wavenumber of 1596 cm^{-1}. However, this shift can be neglected due to very small changes.

Figure 4.11 shows the FWHM of the D and G peaks of the AgNPs-GO sample with the AgNPs deposited at deposition times of 1, 3, 5 and 7 minutes. The FWHM of D peak increase linearly for the samples deposited for 1, 3, 5 and 7 minutes of deposition time. The FWHM of the D peak for GO without AgNPs is 126 cm^{-1}. The FWHM increased to 130 cm^{-1} for the AgNPs-GO sample with AgNPs deposited for 1 minute. Further increase in AgNPs deposition times to 3, 5 and 7 minutes increases the FWHM to 135 cm^{-1}, 137 cm^{-1}, and 141 cm^{-1} respectively. The FWHM of G peak is decreased from 89 cm^{-1} to 81 cm^{-1} when AgNPs is deposited for 1 minute. The AgNPs-GO samples with AgNPs deposition times of 3, 5 and 7 minutes shows an increase in FWHM to 85 cm^{-1} and 86 cm^{-1} which is lower than the FWHM for GO coated quartz substrate without the AgNPs.

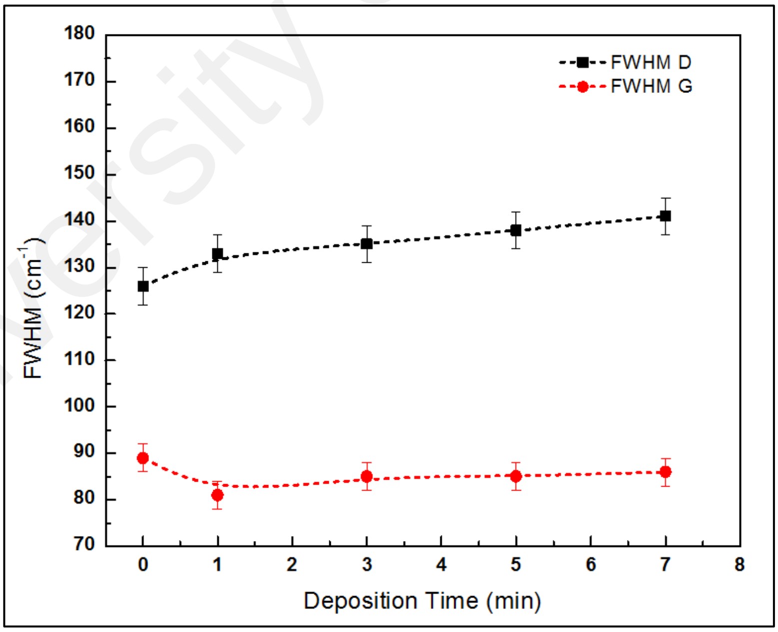

Figure 4.11: FWHM of D and G peak at varied deposition time at 1, 3, 5 and 7 minutes.

The decrease in FWHM of the G peak is usually related to the increase in the structural ordering of the sp^2-bonded carbon atoms in the GO film. Thus, immobilizing of AgNPs into the GO film is shown to increase the structural order in the graphitic sites of the GO films. Increase in the FWHM of the D peak with immobilizing of AgNPs into the GO structure can be due to increase in variation of the size of sp^2-bonded carbon rings within the GO structure and is consistent with the analysis of the FESEM images of these samples where increase in AgNPs deposition time increases the distribution of sizes and shapes of the AgNPs.

The ratio of D to G peak, (I_D/I_G) is usually related to the relative structural disorder present in graphitic structures. In GO films, I_D/I_G also gives an insight into the reduction process where oxygen functional groups are removed creating imperfections within the carbon basal plane and can be related to the in-plane sp^2 crystallite size.

Figure 4.12 presents the I_D/I_G of GO and AgNPs-GO with the AgNPs deposited for time durations of 1, 3, 5 and 7 minutes. The I_D/I_G for GO coated quartz substrate is 0.90. When AgNPs is immobilized on GO surface, the I_D/I_G is decreased to 0.88 and remains unchanged when the deposition time is increased to 3 and 5 minutes. The AgNPs appears to modify the defect center of the GO and thus restoring the л conjugation in GO and improves the structural order in sp^2-bonded C grains in the GO structure (Pasricha et al., 2012). The in-plane sp^2 crystallite grain size also increases with the immobilization of AgNPs within the GO film structure.

However, further increase the AgNPs deposition time to 7 minutes increases the I_D/I_G value to 0.90 close to that of GO (0.91). The sites for improving the structural order of sp2-bonded C in the GO film is probably saturated with an increase in the number of AgNPs immobilized onto the GO film when AgNPs is deposited at 5 minutes and a further increase in AgNPs results in defects in the GO sheets in the film structure.

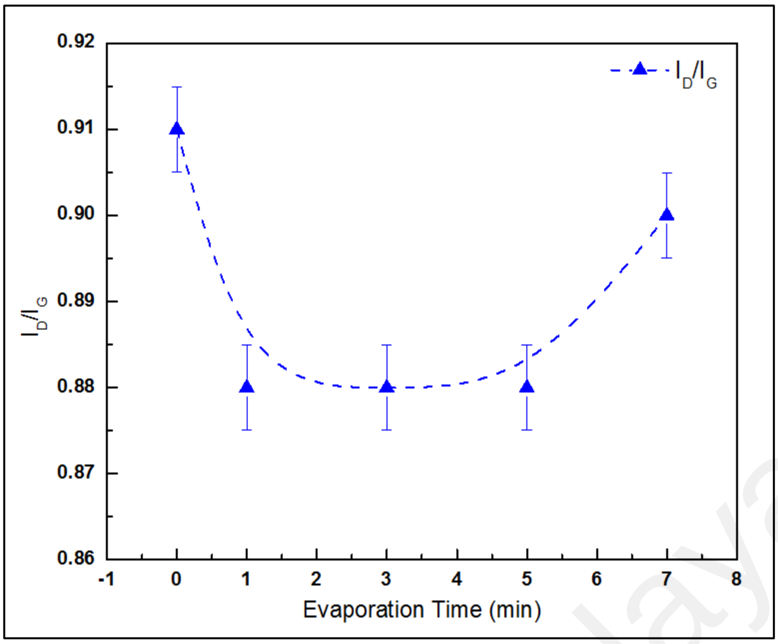

Figure 4.12: I_D/I_G variation for AgNPs-GO at different deposition time.

Analysis of the Raman spectroscopy results on the effects of increasing the deposition time of the AgNPs on GO coated quartz substrates produces some interesting observations and explanations. Immobilization AgNPs on the surface of GO shows some changes in the microstructural properties of GO. In this work, the number of AgNPs added to surface of GO coated quartz substrate is controlled by the deposition time of the AgNPs onto the GO, longer deposition time increases the number of AgNPs and increases inhomogeneity of the sizes and shapes of AgNPs as shown in earlier results presented in the earlier parts of this chapter. Higher density distribution of AgNPs lead to higher intensity of Raman signals and this reflected by the increase in the AgNPs deposition time increases the intensity of the Raman spectra.

Meanwhile, both the D and G peak positions are red-shifted shifted to lower wavenumbers for the samples with deposition times of 1 and 3 minutes. The large increase in deposition times of the AgNPs to 5 and 7 minutes blue-shift these peaks to larger wavenumbers. This phenomenon can be related to the filling of sub-particles of AgNPs on the GO sheet contributing to enhancement of the flat geometry of the graphene nanosheets (Garg et al., 2014) and large increase in the distribution density of the AgNPs alter the flat surface and is reflected by the blue-shift in the D and G peak positions for the samples with AgNPs deposition with duration times of 5 and 7 minutes. The increase in variation of sizes and shapes of the sp^2-bonded carbon rings with an increase in AgNPs deposition time is reflected by the increase in the FWHM of the D band.

Many reports show that I_D/I_G usually increases when AgNPs are added to the GO system (de Faria et al., 2014; Li & Liu, 2010; Li et al., 2015) indicating an increase in structural disorder in the sp^2-bonded C structure in the GO film. However, in this work, it is demonstrated that optimal density distribution, sizes, and shapes of AgNPs in AgNPs-GO samples with AgNPs deposition time of 1 and 3 minutes results in increase in structural ordering of the sp^2-bonded C structures in the GO film as reflected by the low FWHM of the G peak and I_D/I_G of these samples.

4.4 Effect of Substrate Temperature to the AgNPs Depositions

In the first part of this work, the effects of the deposition time of AgNPs at RT on the morphology, SPR and microstructure properties were investigated. The deposition time has shown to have a strong influence on these properties as exposure time to the radiant heat of the hot-filament produces these effects. Since the morphology involving the variation of size and inter-particle distance can induce significant changes in the SPR properties of the AgNPs, the effects of the substrate temperature (T_S) on these SPR properties will also be the focus of discussions in the following sections. In this part of the experiment, the temperature of the substrate was increased to study the properties of AgNPs deposited on the substrate at a higher temperature. The AgNPs studied are grown at RT as a control sample and different T_S of 180 °C, 210 °C and 230 °C on bare and GO coated quartz substrates at a deposition time of 3 minutes. The morphology, microstructure and SPR properties will be determined from the FESEM images, Raman scattering spectroscopy and optical absorption spectra in the visible region.

4.4.1 Morphological Analysis of AgNPs and AgNPs-GO at Different Substrate Temperature

The study of the morphology of AgNPs with effects of T_S variation was investigated using FESEM. The sample was studied at a different T_S at RT, 180 °C, 210 °C, and 230 °C. The presence of AgNPs with different morphologies can be observed on substrates at all range of applied temperature. The AgNPs deposition at different T_S shows significant influence on the distribution and shapes of the AgNPs. Figures 4.13 (a), (b), (c) and (d) show FESEM image of AgNPs deposited at varied T_S of RT, 180 °C, 210 °C and 230 °C respectively. To ease the comparison, all images are presented on the same scale. It was observed that AgNPs have distributed uniformly of average size 12 nm without substrate heating.

Comparing to the sample deposited at RT, changes of the nanoparticle size, interparticle distance and the particle density with increasing T_S were observed. When the melted Ag deposited on the heated substrate at 180 °C, a small size distribution of AgNPs was obtained as presented in Figures 4.13 (b). The growth of the smaller size of AgNPs was observed and a few clusters of AgNPs started to form. At T_S 210 °C, more Ag cluster was formed due to the gain of kinetic energy at a higher temperature which will merge the smaller nanoparticles to form larger NPs size. The merging of smaller NPs to form Ag cluster resulted in the increase of interparticle distance. At elevated temperature, NPs with very small size was unstable. The particles with high surface mobility tend to merge and formed an island. At 230 °C, more Ag clusters were observed when of maximum size 24 nm. Hereby, it can be concluded that increasing the T_S will grow more Ag island on a bare substrate.

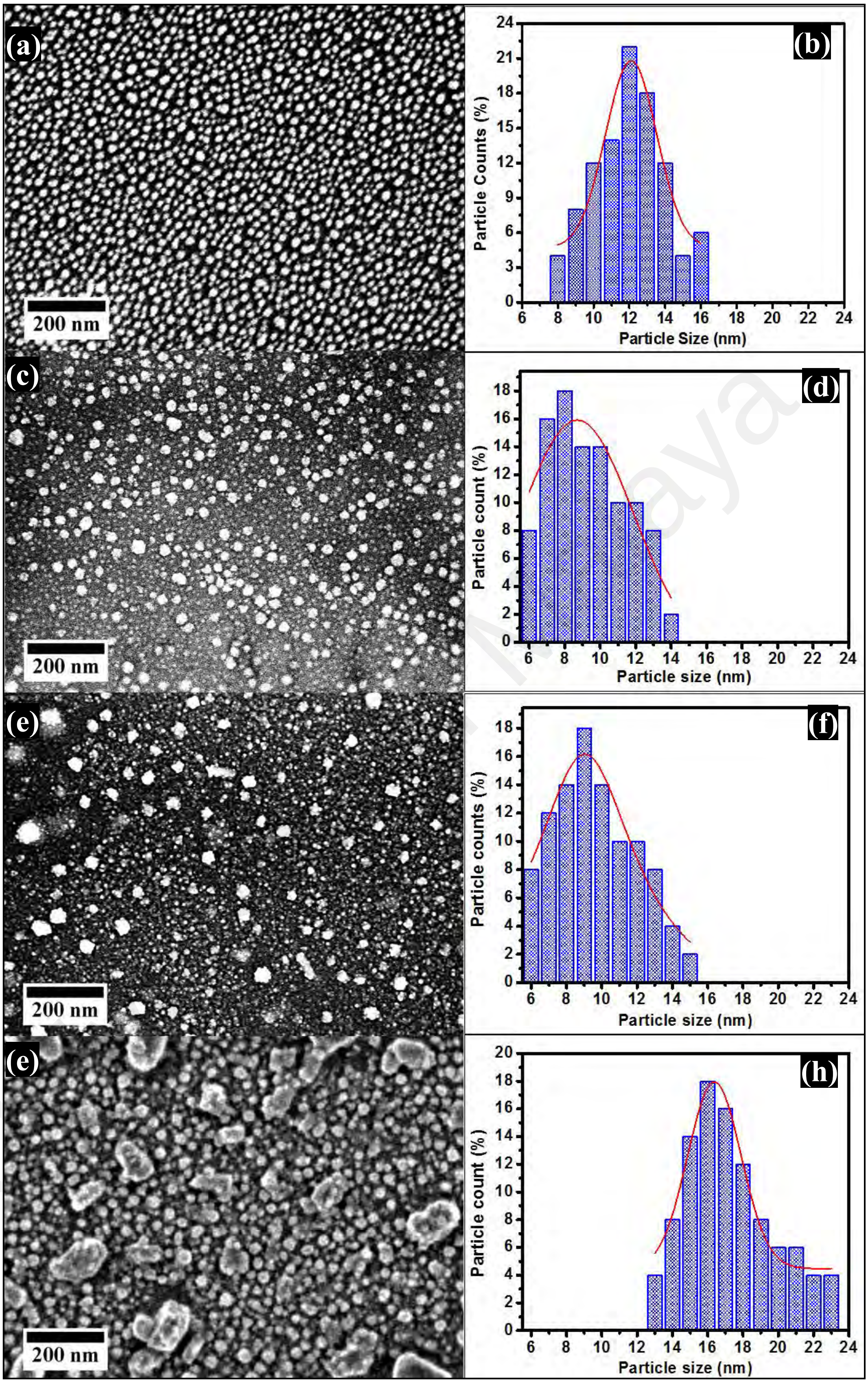

Figures 4.13: FESEM image (a), (c), (e) and (g) and the distribution size (b), (d), (f) and (h) for silver nanoparticles on quartz substrate at varied substrate temperature at RT, 180 °C, 210 °C and 230 °C.

The histogram in Figures 4.13 (b), (d), (f) and (h) illustrates the nanoparticle size for each sample at RT, 180 °C, 210 °C and 230 °C. The size and distribution are fitted with Gaussian distribution function. As shown in the histogram, at different T_S the NPs formed within the size range of 6 – 24 nm. The mean size for AgNPs is around 9 nm for AgNPs deposited at T_S 180 °C and 210 °C. Meanwhile at 230 °C, mostly all NPs were merged to form islands of average size 16 nm. Based on the FESEM image of AgNPs deposited at heated temperature, it can be concluded that the increase of T_S significantly changes the morphology. AgNPs is unstable and aggregated at high temperatures when deposited on a bare quartz substrate.

FESEM images in Figures 4.14 (a), (c), (e) and (g) display the morphology of AgNPs on GO with different TS at RT, 180 °C, 210 °C and 230 °C. At RT, the AgNPs was non-uniformly deposited on GO. The structure of the GO films was simultaneously modified as the substrate was heated. Thus, it will affect the growth of AgNPs on GO films. At 180 °C, a combination of small and large NPs within GO film was observed. A high density of AgNPs was deposited on GO coated quartz substrate of 700 particles/μm^2. When the TS was increased to 210 °C and above, the NPs were observed to be in close contact with each other and the films became even smoother. It is clear that this hybrid film is well distributed and uniform size within a large scale of 730 particles/μm^2. Furthermore, a well-separated formation of AgNPs on GO was displayed. Meanwhile, at 230 °C, FESEM image displayed that the AgNPs grow larger due to coalescence mechanism. The particle counts per unit micron decreased to 580 particles/μm^2 due to the size increment at 230 °C.

The trend of the variation in size of the NPs can be observed in histogram of Gaussian shaped particle size distribution as shown in Figures 4.14 (b), (d), (f) and (h). The narrow FWHM of Gaussian curve for all samples indicates that the variation in size of the NPs on the GO coated substrate is small. The shift of the fitted curve for samples of AgNPs on GO grown with TS at RT, 180 °C, 210 °C and 230 °C showed similar trends with samples AgNPs grown on a bare quartz substrate which was increasing in size with the increasing of TS. The average NPs size is almost similar in the range between 7 to 32 nm with the average size of 9 nm, 13 nm, 19 nm and 24 nm corresponds to samples grown at 1, 3, 5 and 7 minutes of deposition time. Compared to AgNPs-GO structure, it was found that the pure AgNPs are obviously aggregated revealing that the presence of GO enables the homogeneous distribution of AgNPs.

Figures 4.14 (b), (d), (f) and (h) present the histogram of size distribution of AgNPs-GO at different T_S. For AgNPs deposited at RT, the interparticle distance was apart. Hence, the particles distribution consists of a less surface coverage of NPs with a uniform size and distribution. As the T_S increase, the particles and cluster are transformed due to thermal enhancement in term of atom mobility which caused rearrangement of the atom and hence particles and clusters. When heat applied to the substrate, more particles per unit micron was observed due to the gain in kinetic energy of the Ag vapor atom. Deposition of AgNPs on the heated substrate has caused the AgNPs to migrate to the neighboring particles to form a hillock structure (Serrano et al., 2010). Compared to AgNPs-GO structure, it was found that the pure AgNPs are obviously aggregated revealing that the presence of GO enables the homogeneous distribution of AgNPs.

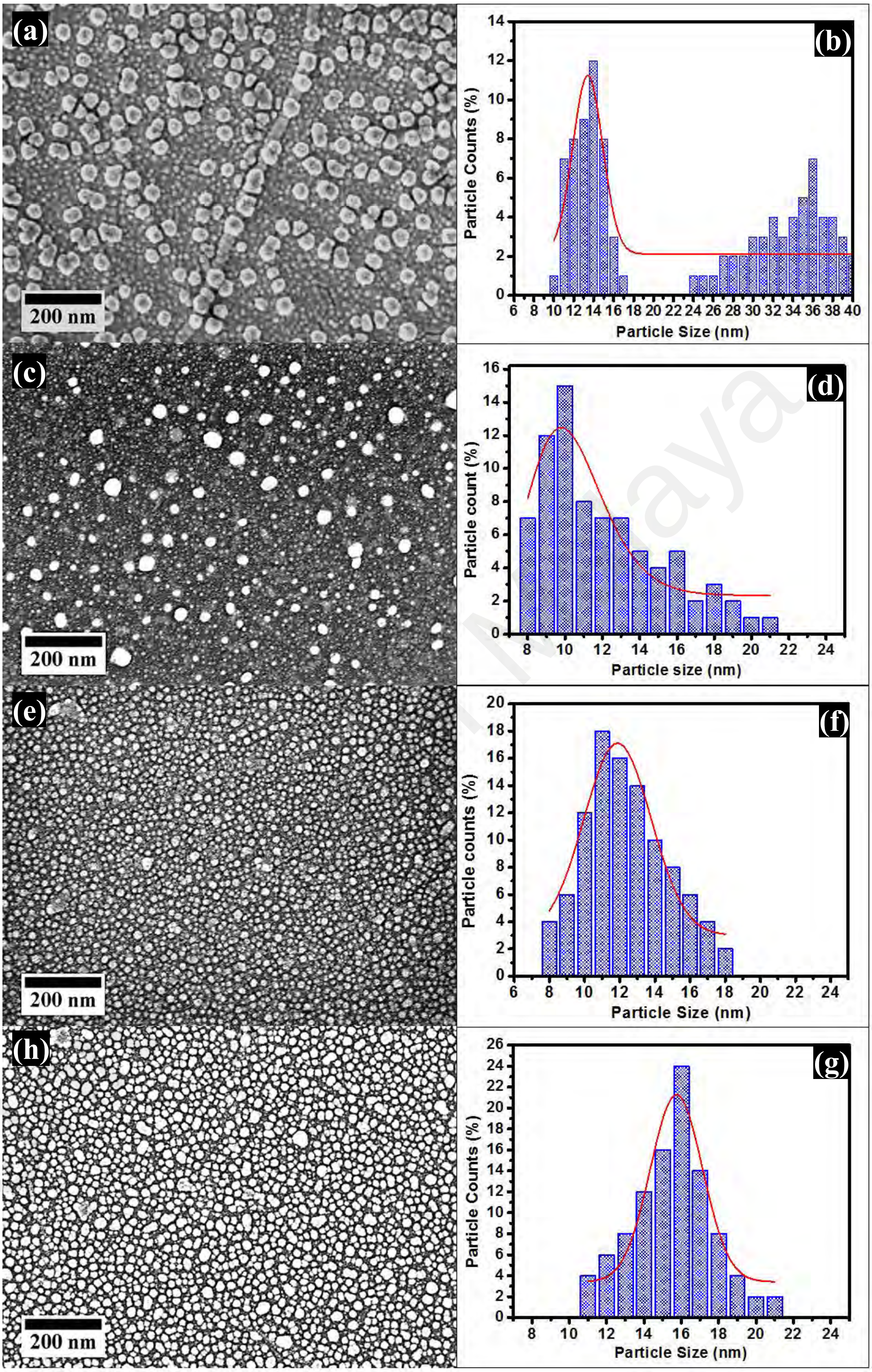

Figure 4.14: FESEM image (a), (c), (e) and (g) and the distribution size (b), (d), (f) and (h) for AgNPs-GO at varied substrate temperature at RT, 180 °C, 210 °C and 230 °C.

Figure 4.15 summarizes the growth behavior of the AgNPs on bare and GO coated quartz substrates with respect to the T_S. At higher T_S, the smaller AgNPs were consumed by the larger NPs, which resulted in a decrease of the areal density of AgNPs accompanied by a simultaneous increase of the average nanoparticle size. These NPs behavior can be observed at T_S started from 180 °C to 230 °C on a quartz substrate. Increasing T_S will increase the AgNPs size.

Meanwhile, AgNPs on GO coated substrate showed a similar trend of the NPs size with the increasing of T_S. However, AgNPs-GO showed a more controllable size and shape of AgNPs with a more uniform distribution. AgNPs started to reshape to a spherical shape and become more uniform at T_S 210 °C. It has been shown that AgNPs would undergo reshaping into large spherical particles after substrate heating because a sphere is the most thermodynamically favored particle shape with the lowest surface energy (Schneid et al., 2015). The presence of defects and oxygen functional groups make GO excellent templates for the post assembly of NPs. It was suggested that the interaction of AgNPs with the oxygenated surface of GO has promoted the reshaping of NPs at higher T_S.

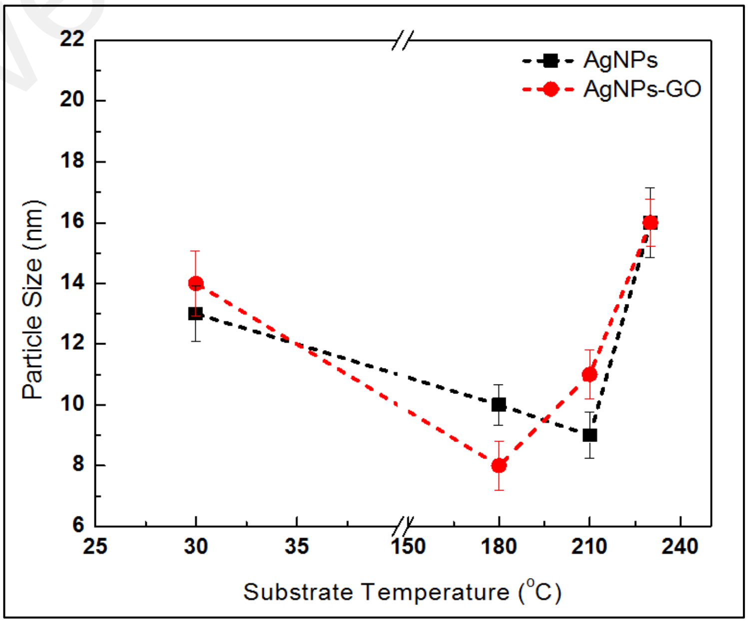

Figure 4.15: Particle size of AgNPs and AgNPs-GO at a varied substrate temperature.

The possible mechanisms are known to be responsible for the NPs growth process at different T_S is Ostwald ripening. In an Ostwald ripening process, atomic species from smaller particles transport to larger particles either by surface diffusion along the substrate or by vapor phase diffusion due to the difference in the chemical potentials between smaller and larger particles. Smaller NPs on the GO surface may be energetically less stable than larger ones due to their relatively larger surface to volume ratio. As a result, the transformation of smaller particles into larger ones could be energetically favorable on the GO surface. In addition, smaller NPs are likely to diffuse more readily than larger ones and so the growth of the larger particles could simply be a consequence of the smaller ones moving and colliding with the larger particles to form even larger particles (Thouti et al., 2015).

4.4.2 Surface Plasmon Resonance Studies on AgNPs and AgNPs-GO at Different Substrate Temperature.

SPR properties of AgNPs and AgNPs-GO deposited at different T_S are studied and analyzed in this section. The SPR properties are studied with respect to the morphological changes of the AgNPs. Figure 4.16 presents the UV-visible absorption spectra of AgNPs deposited at RT and different TS of 180 °C, 210 °C, and 230 °C. Signatures of localized SPR attributed to AgNPs have been observed in all the samples. SPR bands are observed with a peak at 410 nm for the AgNPs on bare quartz substrate deposited at RT. The absorption peaks gradually broadened and shifted to the longer wavelength of 410 nm, 411 nm, 417 nm and 441 nm for the samples deposited at RT and T_S of 180 °C, 210 °C and 230 °C respectively. This has been attributed to the presence of AgNPs of different sizes and distributions on the substrates.

The peak intensity is increasing when the T_S was set at 180 °C with respect to the film at RT. However, at a T_S above 180 °C, the SPR peak intensity is decreased. This decrease is associated with the increase of interparticle distance due to the particles migration on the substrate at a higher temperature. Larger interparticle distance reflects the decaying of field distribution between the particles that leads to the decrease in SPR intensity (Rahman et al., 2014). The changes observed for the characteristics of the SPR band are closely related to the changes in the morphology of the AgNPs with respect to T_S as revealed in FESEM image in Figures 4.13.

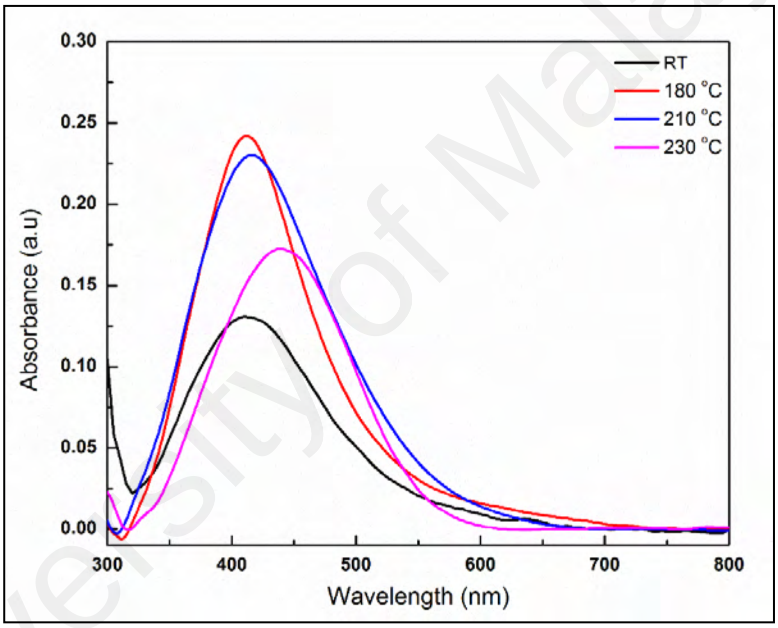

Figure 4.16: Absorption spectra of AgNPs on bare quartz substrates deposited at RT and a different substrate temperature of 180 °C, 210 °C, and 230 °C.

Figure 4.17 presents the UV–vis–NIR absorption spectra for AgNPs-GO deposited at RT and T_S of 180 °C, 210 °C and 230 °C. The absorption spectra of the control sample (GO) shows a maximum absorption at 230 nm, which corresponds to the л → л* transitions of aromatic C-C bonds. A small shoulder appeared at approximately 300 nm corresponds to n → л* transitions of C-O bonds (Dutta et al., 2013; Muhammad Hafiz et al., 2014). The first peak observed in absorption spectra of AgNPs-GO at all varied T_S corresponds to the absorbance of GO. It is observed that peak position of the absorption spectra of GO films with AgNPs grown on heated substrate shifted toward longer wavelength. The main absorption peak in GO is red-shifted from 230 to 254 nm in AgNPs-GO which verifies the restoration of conjugation during the reduction of GO (Dutta et al., 2013). The increase of T_S from 180 °C to 230 °C does not further shift the absorption peak of GO.

SPR band of AgNPs-GO grown at different T_S showed changes in the maximum of 419 nm, 460 nm, 503 nm and 503 nm for samples deposited at RT, 180 °C, 210 °C, and 230 °C. The spectra show that the SPR peak position is shifted to a longer wavelength from RT to 230 °C. The shift of the SPR from RT to 230 °C can be assigned to the coalescence of the metal NPs with the thermal treatment which increases the particle size. Due to the size increase of AgNPs, the interparticle distance was sparsely distributed and this was reflected by the decaying of field distribution between the particles that lead to the decrease in SPR intensity. This strong coupling has resulted in a broader SPR band at a longer wavelength. Meanwhile, at 230 °C, the peak position is saturated at 503 nm.

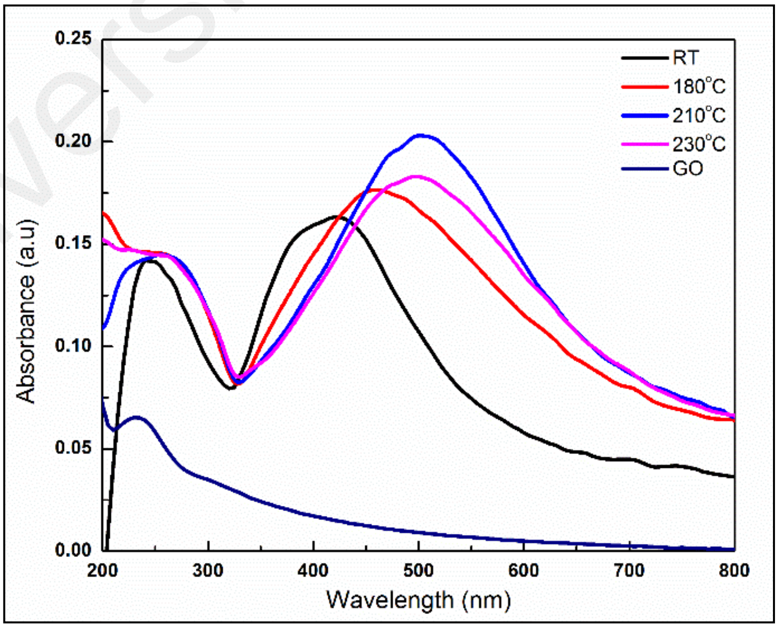

Figure 4.17: Absorption spectra of AgNPs-GO varied substrate temperature at RT, 180 °C, 210 °C and 230 °C.

The detailed plot of the SPR peak position for both AgNPs and AgNPs-GO is shown in Figure 4.18 (a). A large shift of SPR peak position is observed for a film of AgNPs-GO compared to AgNPs due to the difference in surrounding media. Partially embedding AgNPs in GO films produces an increment in the dielectric constant of the surrounding medium, which causes the redshift of localized SPR. The redshift of SPR at higher T_S is consistent with previous studies on metal thin films (Venugopal et al., 2013; X. Zhang et al., 2010).

Figure 4.18 (b) shows the variation of FWHM of AgNPs and AgNPs-GO at varied T_S. FWHM is increasing with the increase of T_S for both AgNPs and AgNPs-GO which are related to the increase in particle size and different surrounding medium. Previous studies showed that besides the particle size, the aspect ratio mainly influences the FWHM. This strong coupling has resulted in a broader SPR band at a longer wavelength. On the contrary, the band is broader as the temperature increase indicates large size distributions of particles. Based on FESEM image obtained, it can be assumed that the broader the SPR band indicates larger and non-homogeneous particles is deposited. The absorption spectrum becomes broader due to the strong coupling between the NPs.

Figure 4.18 (c) shows the variation of SPR intensity of AgNPs and AgNPs-GO at different T_S. A noticeable increase in SPR intensity was observed for both AgNPs and AgNPs-GO from RT to 210 °C. The increasing of intensity at 180 °C is due to the ripening of AgNPs. However, at 230 °C, the SPR intensity is observed to decrease. This phenomenon is assumed to be related to the aggregation of AgNPs and the degree of oxidation occured during the deposition at high temperature. Higher temperature will lead to higher rate of oxidation. Therefore, when the T_S is increased to 230 °C, the plasmon band was suppressed (Kvítek et al., 2013).

From the variation of Ts, it was observed that AgNPs size was changed and thus the SPR properties. It can be concluded that this SPR wavelength position, intensity, and FWHM vary with nanoparticle size, shape, and concentration (Thouti et al., 2015).

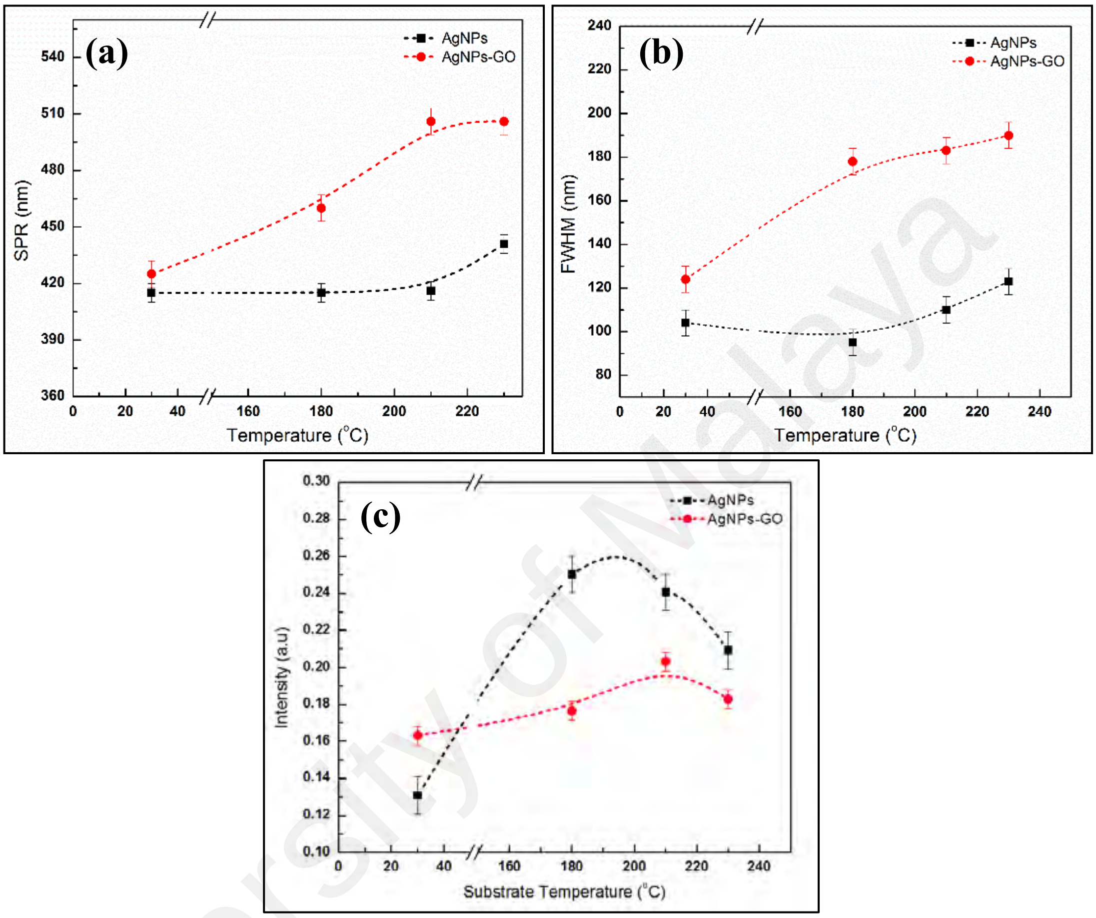

Figures 4.18: Variation of (a) SPR position, (b) FWHM and (c) intensity of AgNPs and AgNPs-GO at varied substrate temperature.

4.4.3 Raman Spectroscopies Studies on AgNPs-GO at Different Substrate Temperature

Four GO samples with different Ts were characterized by Raman spectroscopy with an excitation wavelength of 514 nm, as shown in Figure 4.19. The most prominent features in Raman spectra of GO are the G peak at 1597 cm^{-1} and the D peak at about 1352 cm^{-1}. The existence of 2D and D+G peak is due to the existence of GO structure. The D and G bands in AgNPs-GO hybrid film exhibit a small red shift compared with that of GO due to the interaction between GO and AgNPs.

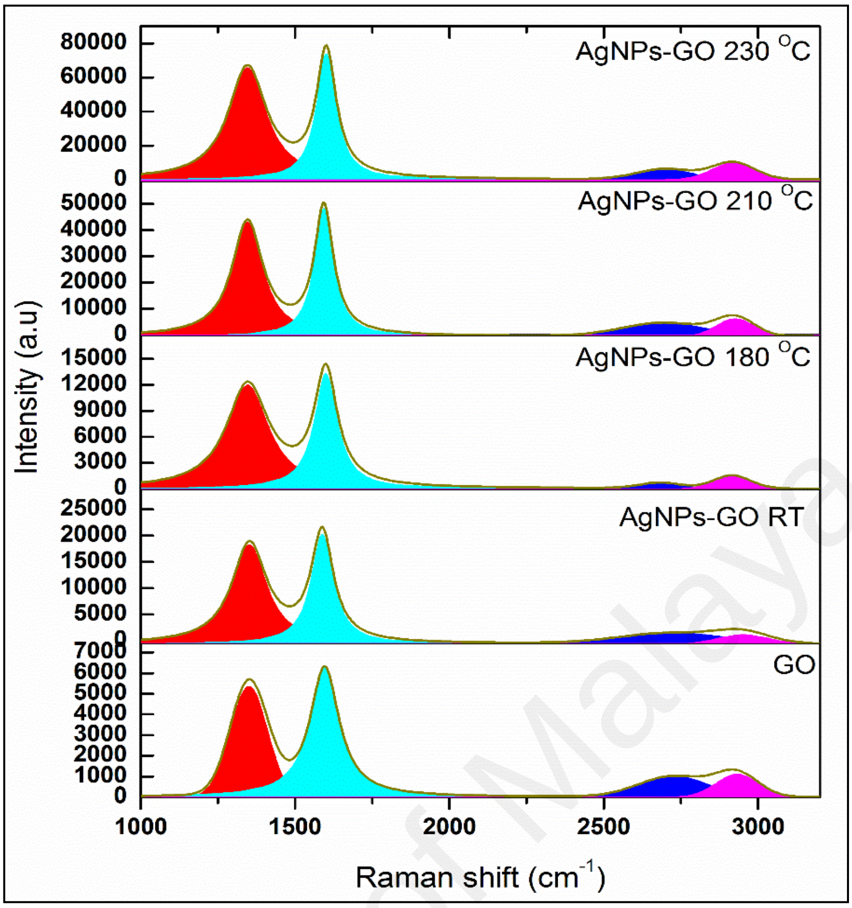

Figure 4.19: Raman spectra of GO and AgNPs deposited on GO at a varied substrate temperature of RT, 180 °C, 210 °C, and 230 °C.

Table 4.2 shows the peak position of D and G peak of AgNPs-GO at different T_S. It was observed from the previous parameter that the immobilization of AgNPs on GO surface at RT has shifted the D peak position which was due to the electromagnetic interaction between GO and AgNPs. There were no prominent changes were detected with the increase of T_S but only a slight blue shift to 1345 cm^{-1} and 1344 cm^{-1} for T_S 180 °C and 210 °C respectively. Increasing the T_S from 210 °C to 230 °C, no changes of D peak position were observed. Meanwhile, compared with the sample at RT, the G peak position was red-shifted about 4 cm^{-1} at a higher T_S of 180 °C, 210 °C and 230 °C. This shift was attributed to an increase in bond structure disorder and/or an increase of sp^3 content. The presence of sp^3 sites results from a distortion of six-fold rings in the carbon network (Seney et al., 2009). However, the peak position of G band was not affected by the increase of T_S from 180 °C to 230 °C. On the contrary, the intensity peaks of the D and G bands are enhanced in the case of AgNPs-GO at higher T_S due to the surface-enhanced Raman scattering effect of AgNPs, which is about 1100 % greater than that of GO (Murphy et al., 2013).

Table 4.2: Peak position of D and G peak of AgNPs-GO at different substrate temperature.

Sample	**D (cm^{-1})**	**G (cm^{-1})**
GO	1352	1597
AgNPs-GO RT	1346	1595
AgNPs-GO 180 °C	1345	1599
AgNPs-GO 210 °C	1344	1599
AgNPs-GO 230 °C	1344	1599

Figure 4.20 presents the variation of FWHM of D and G peak at T_S fixed at RT, 180 °C, 210 °C, and 230 °C. The FWHM of both D and G peak shows non-monotonous trends which are decreasing and increasing. For the D peak, when the T_S was increased to 180 °C and 210 °C, the FWHM is decreasing from 135 nm to 128 nm and 121 nm respectively. The decrease in FWHM of D band indicates the degree of reduction of GO. This indicates the GO structure become more ordered with the immobilization of AgNPs.

However, a significant increase of FWHM was observed at 230 °C of 149 cm^{-1}. This sudden increase at 230 °C can be related to the size of AgNPs attached to GO. The FWHM of G band for as-prepared GO samples was marked at 115 cm^{-1}. With the deposition of AgNPs, the FWHM significantly reduced to 87 cm^{-1}. The attachment of AgNPs to the GO structure has significantly decreased the FWHM of G band with the substrate at the RT. This indicates that the deposition of AgNPs onto GO at T_S 210 °C which has the lowest value of FWHM produced a more ordered structure of GO (Ferrari & Basko, 2013).

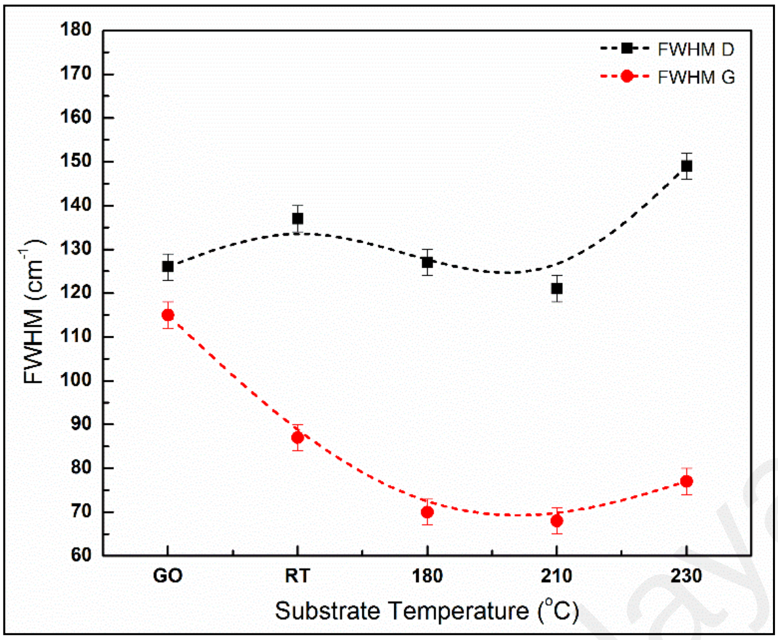

Figure 4.20: Variation of FWHM of D and G peak at different substrate temperature.

Figure 4.21 shows the I_D/I_G of GO and AgNPs-GO at varied T_S. The intensity ratio I_D/I_G in as prepared GO is 0.90, which is slightly decreased to 0.89 in the case of deposition of AgNPs on GO thin film. Upon heating the T_S up to 180 °C and 210 °C, the I_D/I_G ratios decreases to 0.86 and 0.82 respectively. However further increase the T_S to 230 °C, the I_D/I_G ratio showed a sudden increase to 0.89. The decrease in the I_D/I_G can also be attributed to the release of the oxygenated functional groups during thermal conditioning that will decrease the disorder associated with oxygen defects (García-Gómez et al., 2016).

Since I_D/I_G is proportional to the average size of the sp^2 carbon domain, the decreased I_D/I_G is attributed to the removal of defects and the conversion of sp^3 to sp^2 carbons (Tuinstra, 1970). Dao et.al reported that the intensity of the D band is a measure of the amount of disorder in graphene due to the activation of the D band which is attributed to the breaking of the translational symmetry of the C=C sp^2 bond. Therefore, an increase in the number of defects would result in an increase of the D band intensity and is associated with the drop in the intensity of the intrinsic G band of GO and thus increase the value of I_D/I_G (Dao et al., 2013).

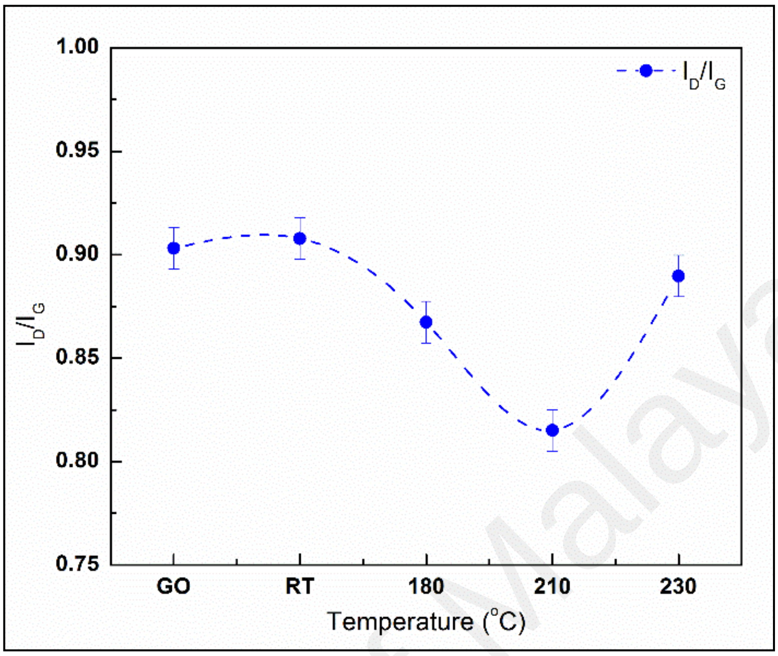

Figure 4.21: Variation of I_D/I_G with the variation of substrate temperature.

From these Raman spectra, we can conclude that 210 °C is the critical T_S for reduction of GO. This critical temperature is in agreement with the study that thermal annealing treatment would lead to lose the hydrogen and result in the graphitization conversion for C-C sp^3 bonded carbon to transform to C=C sp^2 bonded carbon (Tai et al., 2006).

4.5 Effects of Post Deposition Heat Treatment in Vacuum and Nitrogen Environment

In this part, post deposition heat treatment of AgNPs and AgNPs-GO were done. The deposition time and T_S were fixed at 3 minutes and 210 °C for all sample. The post deposition treatment was done in vacuum and Nitrogen (N_2) flows ambient with annealing time fixed for 1 hour. The morphology, optical and structural properties of the deposited sample is discussed in this subchapter. Thermal annealing was performed to study the nucleation and growth of the AgNPs on bare and GO on a quartz substrate. In addition to this, the effects of the annealing environment for the thermal annealing will be also discussed in this section.

4.5.1 Morphological analysis of AgNPs and AgNPs-GO in Vacuum and Nitrogen Environment

Figure 4.22 and Figure 4.23 show the FESEM images of AgNPs and AgNPs-GO annealed in vacuum and N_2 respectively at 210 °C for 1 hour. The results show that thermal annealing have significantly influenced the size, shape, and distributions of AgNPs. Annealing was performed to investigate the formation of AgNPs when exposed to high temperature for a longer time.

Figure 4.22 presents the FESEM image and size distributions of AgNPs annealed at 210 °C for 1 hour in vacuum and N_2 ambient. After 1 hour of annealing, an irregular shape of AgNPs are formed and dispersed randomly on the substrate as well as a small fraction of AgNPs gradually aggregate. The annealing process was performed for 1 hour at 210 °C has increased the kinetic energy of Ag atoms and caused the merging of AgNPs to its neighboring particles. This has significantly resulted in elongation of AgNPs thus increasing its aspect ratio and consequently reducing the particle density on the substrate. The particles were accumulated and dispersed to form larger particles which is known as coalescence mechanism. The histogram in Figure 4.22 (b) shows that the mean size of AgNPs in vacuum condition is around 40 nm. Meanwhile, in N_2 ambient, a similar formation of anisotropic shapes of AgNPs is discovered but in a smaller size distribution of mean size 16 nm as shown in histogram Figure 4.22 (d).

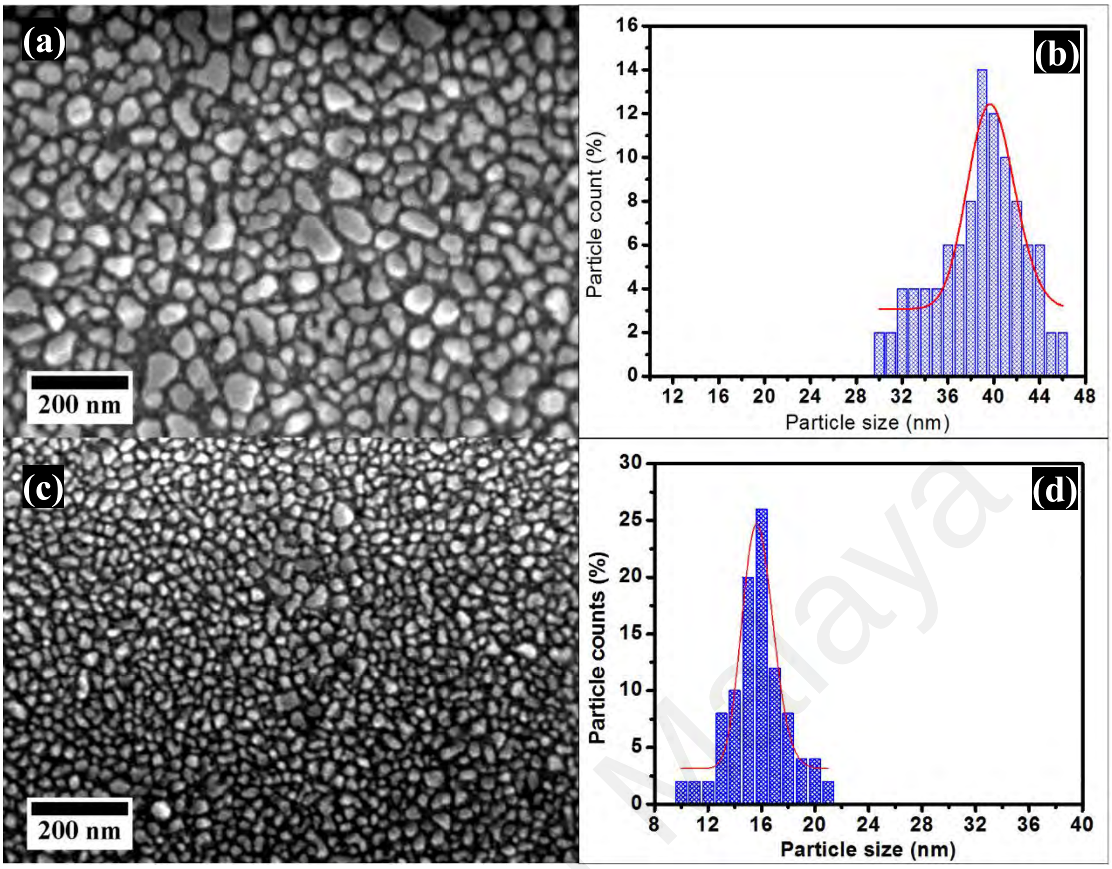

Figure 4.22: Morphology and size distributions of AgNPs annealed in vacuum and Nitrogen ambient.

On the other hand, AgNPs deposited on GO thin film show uniform AgNPs growth as displayed in Figure 4.23. An interesting feature of these samples is the controlled spherical shape of the NPs which was absent in sample AgNPs on bare quartz. They are almost perfectly spherical with small size distributions compared to samples on bare quartz. Compared to the AgNPs-GO composite, it can be found that the AgNPs on a bare quartz substrate is obviously aggregated, this revealed that the presence of GO enables the AgNPs to distribute homogeneously. This was related to the action of GO matrix. GO is known to contain lattice defects (vacancies, holes) and functional groups (carbonyls, epoxides, hydroxyls, etc.) that can act as strong anchoring sites for AgNPs (Xu et al., 2009). The presence of vacancies in the GO structure has been shown to enhance the stability of AgNPs on the GO support while weakening the O_2 adsorption energy on the cluster. The average size of AgNPs is observed to be around 21 nm and 14 nm in a vacuum and N_2 ambient respectively.

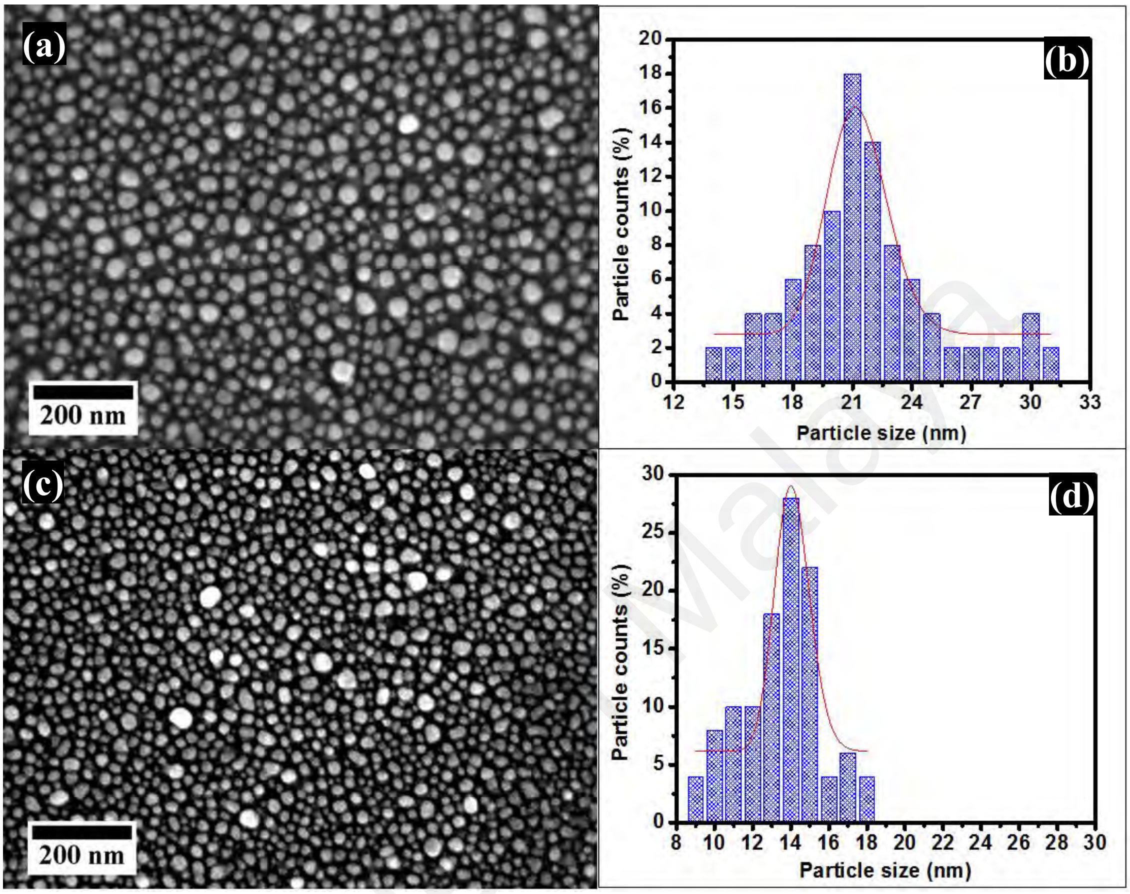

Figure 4.23: Morphology and size distributions of AgNPs-GO in vacuum and N_2 annealing.

In conclusion, the shape of AgNPs is greatly affected by the presence of GO. GO has blocked the elongation of AgNPs into a spherical shape. Without GO, AgNPs are dispersed randomly on the substrate and yield irregular shape distribution. Meanwhile, the treatment of N_2 has assisted in suppressing the growth of AgNPs thus result in the smaller size distribution of AgNPs on a substrate (Rahman et al., 2014). The significant size effect can be observed when compared to the sample without N_2 treatment. The average diameter for AgNPs is around 40 nm and 16 nm for vacuum condition and N_2 treatment respectively. AgNPs annealed with N_2 treatment produce a more uniform nanostructure.

4.5.2 Surface Plasmon Resonance Studies on AgNPs and AgNPs-GO in Vacuum and Nitrogen Environment

Figure 4.24 shows the absorption peak of AgNPs for unannealed, vacuum and N_2 annealing condition. As the AgNPs sample annealed in vacuum, the absorption intensity gradually increases as well as the peak broadening. The SPR position is observed at 437 nm. This shifted peak can be correlated with the coalescence of AgNPs as shown in FESEM (Figure 4.22) enlarged to 41 nm. The SPR peaks broadening and shifting towards longer wavelengths can be presumably attributed to the radiative damping of the resonance as the scattering cross section increases with increasing the size of AgNPs. On the other hand, the SPR position is observed at 417 nm after annealing was performed in N_2 ambient. This SPR position is in trend with the FESEM image that shows AgNPs formed is more uniform with the smaller size distribution of 16 nm compared to AgNPs in vacuum annealing. The FWHM and peak intensity is decreasing which are also related to the size and shape of AgNPs.

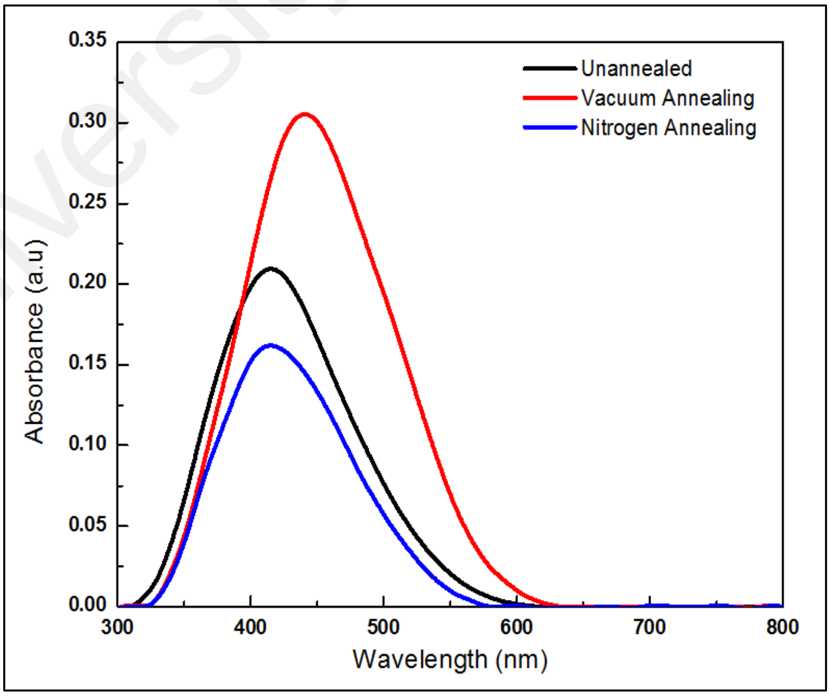

Figure 4.24: Absorption spectra for AgNPs in unannealed, vacuum annealing and N_2 annealing condition.

Figure 4.25 showed the absorption spectra for AgNPs-GO in unannealed, vacuum annealing and N_2 annealing condition. There is 2 peaks observed for AgNPs-GO which corresponds to AgNPs and GO. The first peak observed at 240 nm is contributed by the GO structure. Meanwhile, the second peak, a signature peak of AgNPs are observed at 488 nm and 444 nm for vacuum and N_2 annealing respectively. The variation of the SPR position is due to the difference in morphology for both samples. The SPR intensity for vacuum is almost two times higher than the N_2 annealed sample. It is believed that the significant increase observed in the optical absorption of AgNPs is mainly due to quantum size effects, scattering takes place within the AgNPs layer, the increased pathway of light, and thus maximized the chance for the absorption of light.

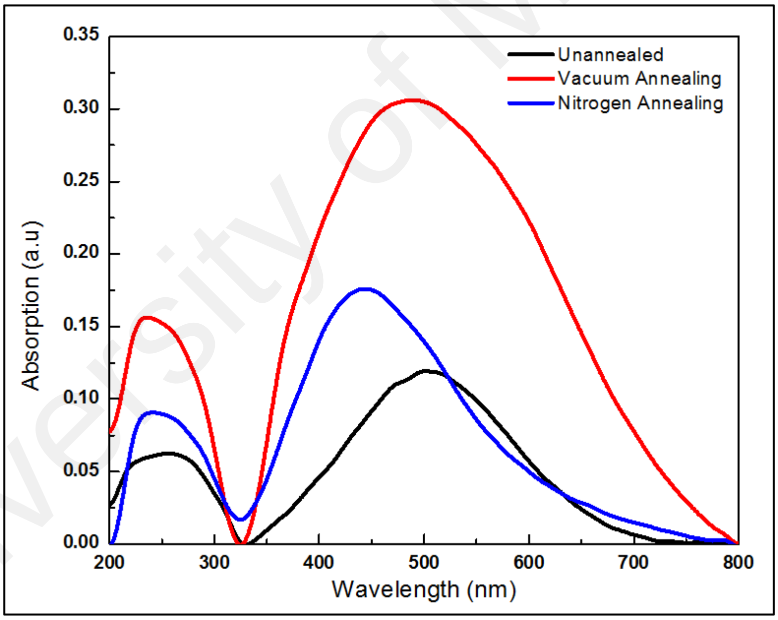

Figure 4.25: Absorption spectra of AgNPs-GO for unannealed, vacuum annealing and N_2 annealing.

4.5.3 Raman Spectroscopies Studies on Silver Nanoparticles on Graphene Oxide

Figure 4.26 shows the fitted Raman spectra of AgNPs-GO for the sample at T_S 210 °C without annealing, vacuum annealing, and N_2 annealing. From this Raman spectra, it is obvious that the Raman peak intensity is enhanced by one order after annealing was performed in a vacuum ambient. Meanwhile, annealing in N_2 environment has enhanced the Raman intensity peak of 5 orders compared to the not annealed sample and 2.5 orders increasing by comparing to vacuum annealing. This enhancement or SERS effects might be related to the size and shape of the attached AgNPs on the GO structure. The SERS signal largely depends on the Raman hot spots. More AgNPs provide more Raman hot spots, which make the SERS signal stronger. The drop of SERS signal is assumed to be related to the AgNPs size. When the size of AgNPs is larger, the number of gaps between neighboring AgNPs are reduced, which resulted in a decrease of Raman hot spots (Huang et al., 2015). In this experiment, AgNPs-GO annealed in N_2 environment produced a more uniform, small size distribution and isotropic spherical shape of NPs. Thus, the enhancement of the peak is more intense for this sample since it produced more hot spots compared to the AgNPs annealed in a vacuum and not annealed sample.

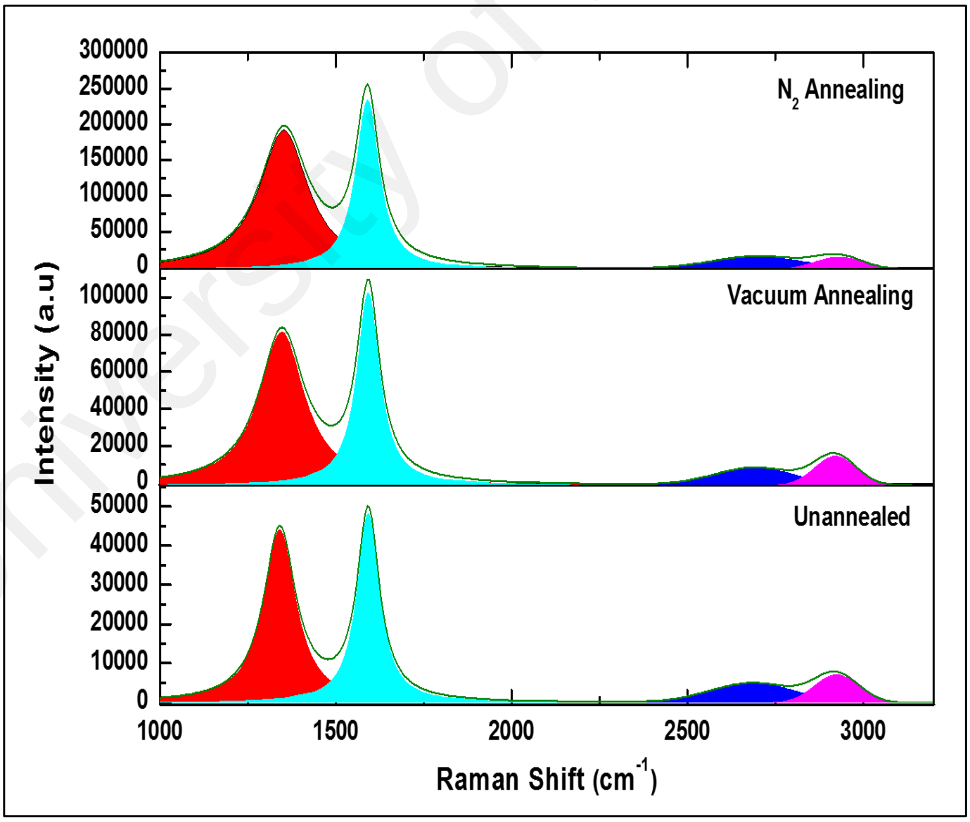

Figure 4.26: Raman spectra of AgNPs-GO for unannealed, vacuum annealing, and N_2 annealing condition.

Table 4.3 shows the position of D and G peak of AgNPs-GO of not anneal, vacuum and N_2 annealing. Annealing has shifted both D and G peak. For D peak, when sample was annealed in vacuum and N_2 environment, the D peak slightly decreasing to 1346 cm^{-1} and 1351 cm^{-1}. Meanwhile, the position of the G peak position was blue shifted to 1592 cm^{-1} and 1589 cm^{-1} with annealing in vacuum and N_2 environment.

The intensity of the D band is a measure of the amount of disorder in graphene because the activation of the D band is attributed to the breaking of the translational symmetry of the C=C sp^2 bond. Therefore, an increase in the number of defects would result in an increase of the D band intensity and a followed by the drop in the intensity of the intrinsic G band and 2D band of graphene (Dao et al., 2013). The calculated value of I_D/I_G shows a decreasing value of 0.86 to 0.77 upon annealing at 210 °C in both vacuum and N_2 environment. This indicates that during thermal annealing, most oxygen-containing group were removed and the conjugated G network (sp^2 Carbon) would be restored (Zainy et al., 2012; Zhou et al., 2012). The I_D/I_G value did not affect by the different annealing environment.

Table 4.3: Peak position of D and G peak of AgNPs-GO at annealing condition.

Sample	**D (cm^{-1})**	**G (cm^{-1})**	**I_D/I_G**
Unannealed	1344	1599	0.86
Vacuum Annealing	1346	1592	0.77
N_2 Annealing	1351	1589	0.77

4.6 Performance of Organic Solar Cell with the Incorporation of AgNPs and AgNPs-GO

Three systems of the OSCs have been made during the experiment, by comparing the hole extraction layer; 1) PEDOT:PSS, 2) AgNPs/PEDOT:PSS and 3) AgNPs-GO/PEDOT:PSS. Full fabrication has been done in open condition including its characterization. Photovoltaic parameters including open-circuit voltage (V_{OC}), short-circuit current density (J_{SC}), the maximum output voltage (V_{max}), maximum output current density (J_{max}) and their maximum output power (P_{max}) for both systems have been calculated. Current density-voltage (J–V) measurements were taken under 100 mW/cm^2 AM 1.5 illumination for the device with and without the presence of AgNPs.

The preliminary result shows improvement in OSCs with the incorporation of AgNPs or AgNPs-GO. Photovoltaic parameters including Jsc, Voc, and P_{max} for both systems have been calculated. The current density/voltage ($J-V$) measurements were taken under 100 mWcm^{-2} AM 1.5 illumination for all the compared the devices. The efficiency of the devices was calculated using the formula;

$$\eta = \frac{P_{max}}{P_{in}} \; x \; \mathrm{FF} \; x \; 100 \; \% \qquad (4.1)$$

Figure 4.27 presents the J_{SC} of the fabricated devices of OSCs system of PEDOT:PSS, AgNPs/PEDOT:PSS and AgNPs-GO/PEDOT:PSS. It shows that the incorporation of AgNPs has improved the J_{SC}. The combination of localized SPR of AgNPs efficiently increases the probability of exciton generation and dissociation which was influenced by the enhanced light scattering by AgNPs. As a result, this has improved the J_{SC} of OSC. Meanwhile, the incorporation of AgNPs complemented with GO to the OSCs system has further increased the J_{SC} of the organic solar cells. Here, it can be assumed that the probability of exciton generation has improved with the presence of GO. This effect might be due to different morphology of AgNPs. AgNPs with uniform size and shape can promote more light scattering in the OSCs system (Kalfagiannis et al., 2012). From this plot, we can also obtain the V_{OC} of the OSCs system.

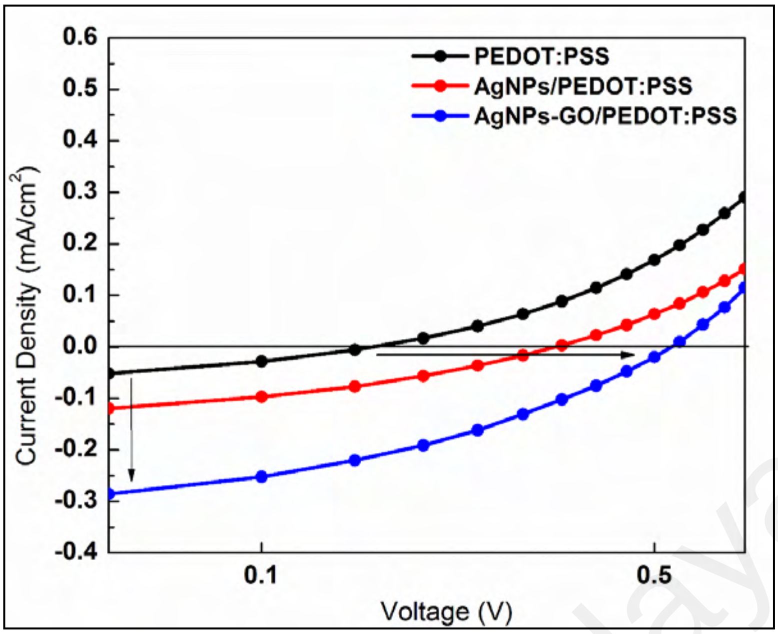

Figure 4.27: Photocurrent density–photovoltage (*J-V*) curves obtained for PEDOT:PSS, AgNPs/ PEDOT:PSS and AgNPs-GO/ PEDOT:PSS**.**

From Figure 4.28, it can be observed that the value of V_{OC} is enhanced about 2-fold with the incorporation of AgNPs of 0.35 V. The integration of AgNPs-GO into the OSCs layer has further enhanced to 0.55 V.

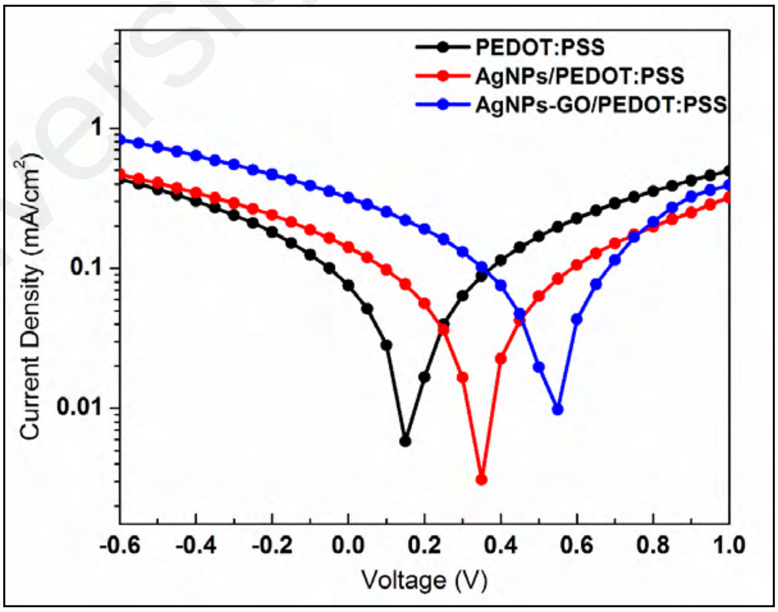

Figure 4.28: Open circuit voltage (V_{OC}) of PEDOT:PSS, AgNPs/ PEDOT:PSS and AgNPs-GO/ PEDOT:PSS**.**

.

Figure 4.29 shows the maximum power density obtained for PEDOT:PSS, AgNPs/PEDOT:PSS, and AgNPs-GO/PEDOT:PSS. It was observed that AgNPs-GO showed the highest power density of 0.25 mW/cm^2 compared to PEDOT:PSS and AgNPs/ PEDOT:PSS of 0.10 and 0.15 mW/cm^2 respectively.

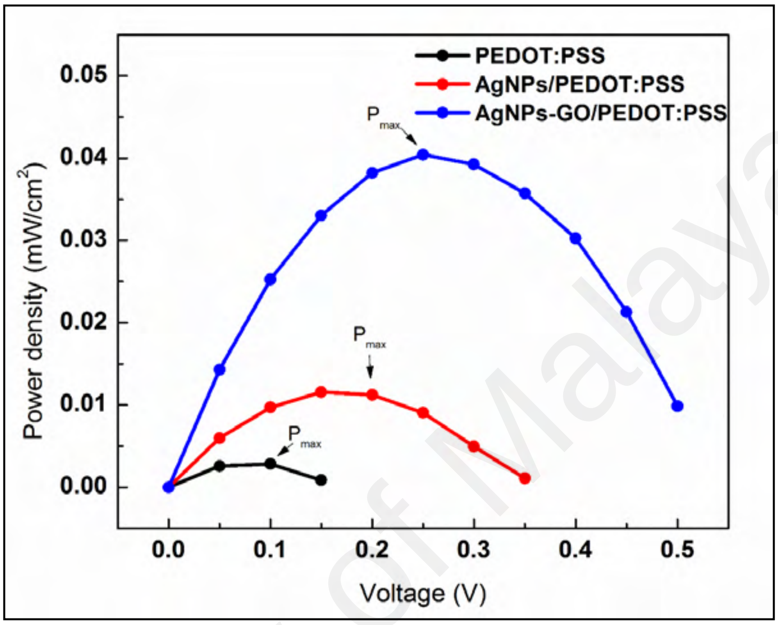

Figure 4.29: Maximum power density (P_{max}) of PEDOT:PSS, AgNPs/ PEDOT:PSS and AgNPs-GO/ PEDOT:PSS**.**

Compared to the device without AgNPs, the AgNPs incorporated device shows the higher efficiency of one order and two orders for AgNPs-GO. It is noteworthy that short-circuit current density J_{SC}, which is limited by several factors including weak absorbance of the solar spectrum and poor transport and collection of separated carriers at the interface of PCDTBT and PC$_{71}$BM, was remarkably improved. Normally, when the charge transport is improved, the FF and J_{SC} will be increased simultaneously.

Overall J_{SC} and FF values produced from the PEDOT:PSS, AgNPs/PEDOT:PSS, and AgNPs-GO/PEDOT:PSS devices are very small compared to those reported in literature for organic solar cells of 11.12 mA/cm^2 (Mahmoudi et al., 2016; Rafique et al., 2017; Smith et al., 2014). There are many factors contribute to this small value including the material handling of the fabricated device and electrical behavior is measured in air. These processes have certainly reduced the OSCs performance through device degradation. These devices are relatively easy to fabricate, can also be processed on flexible substrates, however, they have relatively low conversion efficiencies and offer low stability. Several suggestions to increase the solar cell performance are described in Chapter 5.

Table 4.4: The value of *Jsc*, P_{max}, *Voc* and FF.

Sample	***Jsc* (±0.01) (mA/cm^2)**	***Voc* (±0.02)**	**P_{max} (±0.01) (mW/cm^2)**	**FF (±0.0001)**	**Efficiency (±0.5 x 10^{-4})**
PEDOT:PSS	0.08	0.15	0.10	0.0025	2.5 x 10^{-4}
AgNPs/ PEDOT:PSS	0.14	0.35	0.15	0.0100	15 x 10^{-4}
AgNPs-GO/ PEDOT:PSS	0.31	0.55	0.25	0.0360	90 x 10^{-4}

4.7 Antibacterial Activities of AgNPs and AgNPs-GO

The antibacterial activities of AgNPs and AgNPs-GO were tested using disk diffusion method as mentioned earlier in Chapter 3. Table 4.5 presents the antibacterial properties of GO on glass substrate tested with *E. coli* and *S. aureus*. No zone of inhibition is observed for GO thin film for both bacteria. The absence of zone of inhibition (ZOI) for both E. coli and S. aureus for the control sample indicated attachments of these bacteria to the GO thus showing no antibacterial activity. GO thin film sample is regarded as reference samples for the antibacterial testing of AgNPs and AgNPs-GO against *E. coli* and *S. aureus*.

Table 4.5: The antibacterial properties of the GO against *E. coli* and *S. aureus*.

Bacteria	GO
E. coli **(Gram negative)**	
S. Aureus **(Gram positive)**	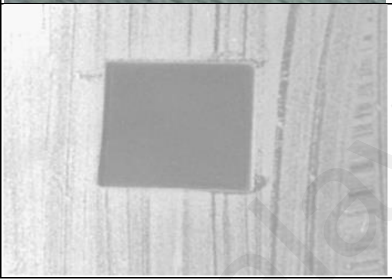

For the AgNPs and AgNPs-GO tested on *S. aureus* and *E. coli* showed a clear zone surrounding the glass substrates as shown in Figure 4.30 and Figure 4.31 respectively. This clear zone is known as ZOI. The antibacterial activities of AgNPs towards *E. coli* and *S. aureus* showed almost similar diameter of the ZOI of 16.0 mm. Surprisingly, despite the negative result obtained for GO thin film tested, the sample AgNPs-GO tested on *S. aureus* shows a significant enhancement in ZOI as compared to AgNPs of 17.5 mm. This enhancement might be attributed to the synergistic effect of AgNPs and GO (Zhang et al., 2015). The presence of GO was shown to enhance the attachment and proliferation of the bacteria cells. This resulted in an increase in the interaction between the AgNPs and the bacteria surface due to the increase in the number of AgNPs on the GO coated substrate which led to the improvement in the antibacterial activity (Ruiz et al., 2011).

Meanwhile for AgNPs-GO tested against *E. coli* shows a small increment in the ZOI of 16.5 mm as compared to sample with AgNPs. The lower sensitivities of *E. coli* as compared to *S. aureus* can be attributed to the presence of the outer membrane on the *E. coli* which consisted of the tightly packed lipopolysaccharide (LPS) molecules. This LPS molecule provides an effective barrier against AgNPs (Ma et al., 2011). Thereby, *E. coli* is harder to destroy and could develop resistance against AgNPs antibacterial properties. This *E. coli* showed similar resistance towards the AgNPs-GO sample since no significant change was observed in the ZOI as compared to AgNPs sample. In our case, AgNPs-GO demonstrated higher antibacterial efficacy against the Gram-positive bacteria as normally could be expected.

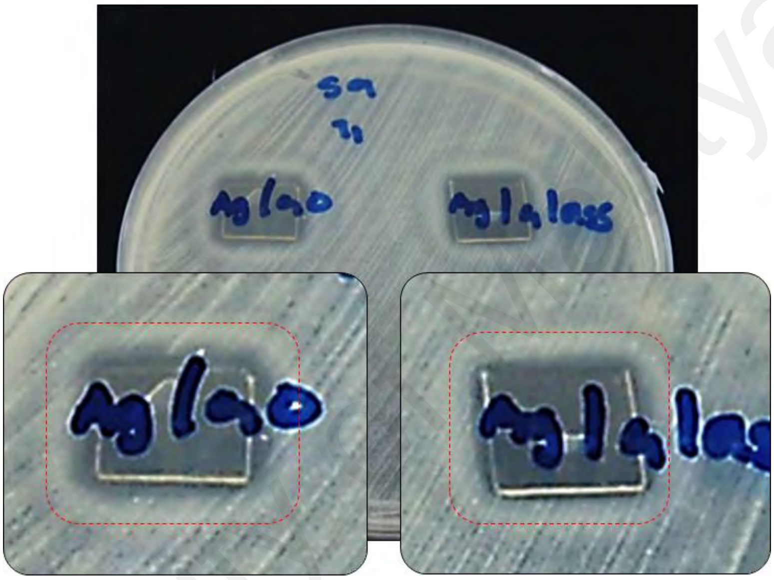

Figure 4.30: Antibacterial test of AgNPs and AgNPs-GO with *S. aureus*.

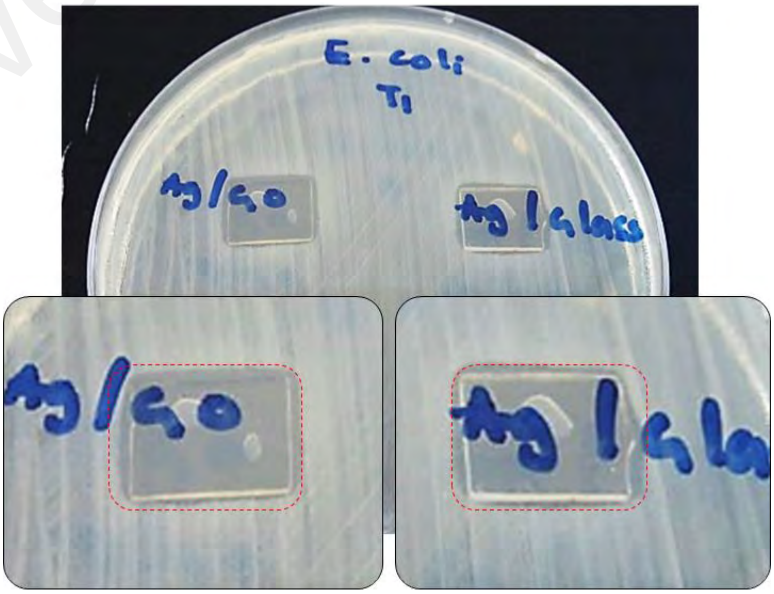

Figure 4.31: Antibacterial test of AgNPs and AgNPs-GO with *E. coli*.

In recent times, it has been discovered that nanoparticles exhibit cytotoxic effects against both Gram-positive and Gram-negative bacteria through different mechanisms such as inducing apoptosis-like process and inhibition of cell proliferation (Bao et al., 2015; Orlov et al., 2016). This work showed that the antibacterial activities were increased for the AgNPs-GO sample but were dependent on the type of bacteria. The antibacterial effect of AgNPs-GO studied in this work was found to be similar to earlier reports (Shahverdi et al., 2007) except that for the results in this work showed the antibacterial effect was dependent on the type of bacteria and in this case was very effective on the *S. aureus* bacteria.

Tang et al., 2013 reported that their AgNPs-GO developed by a one-pot boiling method showed the higher performance of bactericidal effect against *E. coli* when compared to *S. aureus*. The bactericidal effect of AgNPs-GO composite against *E. coli*, they claimed was due to the bacterial cell wall integrity disruption while for *S. aureus* was due to inhibition of cell division, which showed a lower performance when compared to *E. coli*. However, in our case, AgNPs-GO demonstrated higher antibacterial efficacy against the Gram-positive bacteria as normally could be expected. In recent times, it has been discovered that nanoparticles exhibit cytotoxic effects against both Gram-positive and Gram-negative bacteria through different mechanisms such as inducing apoptosis-like process and inhibition of cell proliferation (Bao et al., 2015; Orlov et al., 2016).

Many factors can impact the toxicity of AgNPs. However, results presented herein demonstrate the importance of the preliminary results observed in this work illustrated the possible application of AgNPs-GO coated glass as an effective antibacterial material that can be applied in biomedical applications.

CHAPTER 5: CONCLUSIONS

5.1 Conclusions

As a conclusion, AgNPs-GO nanocomposite films have been successfully synthesized using HWCVD techniques followed by the characterization of the morphology, optical and structural properties of AgNPs-GO films. Firstly, GO films were deposited using the spin coating technique followed by thermal evaporation the AgNPs onto the surface of GO films and bare substrate as a control sample using HWCVD system. The growth of AgNPs was studied by varying parameters of deposition time, T_S, and post-deposition heat treatment. It was noteworthy that AgNPs were successfully deposited on GO coated substrate and bare substrate. The average size of AgNPs increased with the increase of growth time and the yield of uniform nanoparticle distribution was obtained at substrate temperature 210 ºC. AgNPs post-annealed in N_2 gas environment were smaller in size of size 14 nm as compared the AgNPs post-annealed in a vacuum with average size 22 nm.

Embedding AgNPs into GO film matrix showed significant effects on its structure and optical properties. For structural properties of AgNPs-GO, it is proven that with the deposition of AgNPs, the structure of GO become more ordered and GO successfully control the size of AgNPs. Meanwhile, from UV-Visible measurement, it can be conclude that AgNPs size plays a vital role in tuning the SPR position which are the important for utilization in various applications. Meanwhile, the agglomerated and elongated structure were observed for AgNPs on a bare substrate. This proved that GO can act as a matrix for the growth of AgNPs which can control the spherical shape of AgNPs. The abundance of negative charge on the GO structure stabilize the formation of AgNPs without agglomeration occurred.

The photovoltaic device was fabricated by adding the AgNPs and AgNPs-GO to the conventional organic solar cells of ITO/PEDOT:PSS/PCDTBT:$PC_{71}BM$/Al. The current density-voltage (*J-V*) measurement was focused on the short-circuit-current density, *Jsc* since this value represent charge transfer transport behavior. Highest *Jsc* value, as well as fill factor, are determined for the device consists of the incorporation of AgNPs-GO film to the organic solar cells. With the incorporation of AgNPs-GO, the value of J_{SC} reaches 0.31 mA/cm^2, which is nearly 4-fold higher compared to the device without AgNPs-GO of 0.08 mA/cm^2. Charge transport in this device is more efficient thus yield higher J_{SC} value. This result agrees with the explanation of the morphology, structural and optical properties of AgNPs-GO with N_2 annealing condition.

For antibacterial applications, three samples of GO, AgNPs, and AgNPs-GO were compared to study the bacteria activities on the film. It was revealed that GO did not inhibit the bacterial growth in the film. However, the AgNPs-GO films showed enhancement in the zone of inhibition towards *S. aureus* bacteria. The antibacterial effect was shown to be dependent on the type of bacteria as the change in the zone of inhibition was not significant on *E. coli* bacteria.

5.2 Future Works

The deposition of AgNPs on GO films promises better NPs distribution with small size and spherical shapes that can be applied in various applications. However, there are many aspects that have yet to be investigated due to time limitation. The following suggestions are proposed for future works.

- Further characterization methods to be employed for these AgNPs-GO such as electrical properties, photoluminescence, and high resolution (TEM) images.

- The AgNPs-GO films have shown to have selective antibacterial properties towards *S. aureus* and *E. coli* bacteria. This AgNPs-GO film can be further tested for its antibacterial properties with the other types of bacteria.
- In the present work, the organic solar cells device fabrication and measurements are carried out in an ambient condition which may increase the risk of degradation of the devices. Therefore, in future works, it can be suggested that all the experimental work would be done under vacuum condition.
- In the future, hopefully, the results of this current work have a potential improve the large-scale production.

REFERENCES

Abou El-Nour, K. M. M., Eftaiha, A., Al-Warthan, A., & Ammar, R. A. A. (2010). Synthesis and applications of silver nanoparticles. *Arabian Journal of Chemistry*, *3*(3), 135–140.

Akhavan, O., & Ghaderi, E. (2010). Toxicity of graphene and graphene oxide nanowalls against bacteria. *ACS Nano*, *4*(10), 5731–5736.

Al-Ghamdi, H. S., & Mahmoud, W. E. (2013). One pot synthesis of multi-plasmonic shapes of silver nanoparticles. *Materials Letters*, *105*, 62–64

Amendola, V., Bakr, O. M., & Stellacci, F. (2010). A study of the surface plasmon resonance of silver nanoparticles by the discrete dipole approximation method: effect of shape, size, structure, and assembly. *Plasmonics*, *5*(1), 85–97.

Armelao, L., Barreca, D., Bottaro, G., Gasparotto, A., Gross, S., Maragno, C., & Tondello, E. (2006). Recent trends on nanocomposites based on Cu, Ag and Au clusters: A closer look. *Coordination Chemistry Reviews*, *250*(11–12), 1294–1314.

Asanithi, P., Chaiyakun, S., Limsuwan, P., Asanithi, P., Chaiyakun, S., & Limsuwan, P. (2012). Growth of silver nanoparticles by DC magnetron sputtering. *Journal of Nanomaterials*, *2012*, 1–8.

Atwater, H. A., & Polman, A. (2010). Plasmonics for improved photovoltaic devices. *Nature Materials*, *9*(3), 205–213.

Bao, H., Yu, X., Xu, C., Li, X., Li, Z., Wei, D., & Liu, Y. (2015). New toxicity mechanism of silver nanoparticles: promoting apoptosis and inhibiting proliferation. *PloS One*, *10*(3), e0122535.

Boies, A. M., Lei, P., Calder, S., Shin, W. G., & Girshick, S. L. (2011). Hot-wire synthesis of gold nanoparticles. *Aerosol Science and Technology*, *45*(5), 654–663.

Cho, S. H., Lee, S., Ku, D. Y., Lee, T. S., Cheong, B., Kim, W. M., & Lee, K. S. (2004). Growth behavior and optical properties of metal-nanoparticle dispersed dielectric thin films formed by alternating sputtering. *Thin Solid Films*, *447–448*, 68–73.

Chook, S. W., Chia, C. H., Zakaria, S., Ayob, M. K., Chee, K. L., Huang, N. M., … Rahman, R. (2012). Antibacterial performance of Ag nanoparticles and AgGO nanocomposites prepared via rapid microwave-assisted synthesis method. *Nanoscale Research Letters*, *7*(1), 541.

Dao, T. D., Lee, H., Jeong, H. M., & Kim, B. K. (2013). Direct covalent modification of thermally exfoliated graphene forming functionalized graphene stably dispersible in water and poly(vinyl alcohol). *Colloid and Polymer Science*, *291*(10), 2365–2374.

Das, M. R., Sarma, R. K., Saikia, R., Kale, V. S., Shelke, M. V, & Sengupta, P. (2011). Synthesis of silver nanoparticles in an aqueous suspension of graphene oxide sheets and its antimicrobial activity. *Colloids and Surfaces. B, Biointerfaces*, *83*(1), 16–22.

de Faria, A. F., Martinez, D. S. T., Meira, S. M. M., de Moraes, A. C. M., Brandelli, A., Filho, A. G. S., & Alves, O. L. (2014). Anti-adhesion and antibacterial activity of silver nanoparticles supported on graphene oxide sheets. *Colloids and Surfaces. B, Biointerfaces*, *113*, 115–124.

Dizaj, S. M., Lotfipour, F., Barzegar-Jalali, M., Zarrintan, M. H., & Adibkia, K. (2014). Antimicrobial activity of the metals and metal oxide nanoparticles. *Materials Science and Engineering: C*, *44*, 278–284.

Dutta, S., Ray, C., Sarkar, S., Pradhan, M., Negishi, Y., & Pal, T. (2013). Silver nanoparticle decorated reduced graphene oxide (rGO) nanosheet: a platform for SERS based low-level detection of uranyl ion. *ACS Applied Materials & Interfaces*, *5*(17), 8724–8732.

Eda, G., Lin, Y.-Y., Miller, S., Chen, C.-W., Su, W.-F., & Chhowalla, M. (2008). Transparent and conducting electrodes for organic electronics from reduced graphene oxide. *Applied Physics Letters*, *92*(23), 233305.

Ethiraj, A. S., Jayanthi, S., Ramalingam, C., & Banerjee, C. (2016). Control of size and antimicrobial activity of green synthesized silver nanoparticles. *Materials Letters*, *185:* 526–529.

Eustis, S., El-Sayed, M. A., El-Sayed, M. A., Meltzer, S., Requicha, A. A. G., Atwater, H. A., … Huang, J. (2006). Why gold nanoparticles are more precious than pretty gold: Noble metal surface plasmon resonance and its enhancement of the radiative and nonradiative properties of nanocrystals of different shapes. *Chemical Society Reviews*, *35*(3), 209–217.

Fan, W., Lee, Y. H., Pedireddy, S., Zhang, Q., Liu, T., Ling, X. Y., … Sheu, S. F. (2014). Graphene oxide and shape-controlled silver nanoparticle hybrids for ultrasensitive single-particle surface-enhanced Raman scattering (SERS) sensing. *Nanoscale*, *6*(9), 4843-4851.

Fernando, K. A. S., Watson, V. G., Wang, X., McNamara, N. D., JoChum, M. C., Bair, D. W., … Bunker, C. E. (2014). Migration of silver nanoparticles from silver decorated graphene oxide to other carbon nanostructures. *Langmuir : The ACS Journal of Surfaces and Colloids*, *30*(39), 11776–11784.

Ferrari, A. C., & Basko, D. M. (2013). Raman spectroscopy as a versatile tool for studying the properties of graphene. *Nature Nanotechnology*, *8*(4), 235–246.

Fleetham, T., Choi, J.-Y., Choi, H. W., Alford, T., Jeong, D. S., Lee, T. S., … Kim, I. (2015). Photocurrent enhancements of organic solar cells by altering dewetting of plasmonic Ag nanoparticles. *Scientific Reports*, *5*, 14250.

Fumitaka Mafuné, Jun-ya Kohno, Yoshihiro Takeda, A., Kondow, T., & Sawabe, H. (2000). Formation and size control of silver nanoparticles by laser ablation in aqueous solution. *104*(39), 9111–9117.

Ganguly, A., Sharma, S., Papakonstantinou, P., & Hamilton, J. (2011). Probing the thermal deoxygenation of graphene oxide using high-resolution in situ x-ray-based spectroscopies. *The Journal of Physical Chemistry C*, *115*(34), 17009–17019.

García-Gómez, A., Eugénio, S., Duarte, R. G., Silva, T. M., Carmezim, M. J., & Montemor, M. F. (2016). Electrodeposited reduced-graphene oxide/cobalt oxide electrodes for charge storage applications. *Applied Surface Science*, *382*, 34–40.

Garg, R., Dutta, N., & Choudhury, N. (2014). Work function engineering of graphene. *Nanomaterials*, *4*(2), 267–300.

Haidari, G., Hajimahmoodzadeh, M., Fallah, H. R., & Varnamkhasti, M. G. (2015). Effective medium analysis of thermally evaporated Ag nanoparticle films for plasmonic enhancement in organic solar cell. *Superlattices and Microstructures*, *85*, 294–304.

Halas, N. J., Lal, S., Chang, W. S., Link, S., & Nordlander, P. (2011). Plasmons in strongly coupled metallic nanostructures. *Chemical Reviews*, *111*(6), 3913–3961

He, L., Dumée, L. F., Liu, D., Velleman, L., She, F., Banos, C., … Kong, L. (2015). Silver nanoparticles prepared by gamma irradiation across metal–organic framework templates. *RSC Advance*, *5*(14), 10707–10715.

Hong, J., Park, M. K., Lee, E. J., Lee, D., Hwang, D. S., & Ryu, S. (2013). Origin of new broad Raman D and G peaks in annealed graphene. *Scientific Reports*, *3*, 2700.

Huang, J., Xie, Z., Xie, Z., Luo, S., Xie, L., Huang, L., … Zeng, T. (2016). Silver nanoparticles coated graphene electrochemical sensor for the ultrasensitive analysis of avian influenza virus H7. *Analytica Chimica Acta*, *913*, 121–127.

Huang, Q., Wang, J., Wei, W., Yan, Q., Wu, C., & Zhu, X. (2015). A facile and green method for synthesis of reduced graphene oxide/Ag hybrids as efficient surface enhanced Raman scattering platforms. *Journal of Hazardous Materials*, *283*, 123–130.

Jeong, H. Y., Kim, J. Y., Kim, J. W., Hwang, J. O., Kim, J.-E., Lee, J. Y., … Choi, S.-Y. (2010). Graphene oxide thin films for flexible nonvolatile memory applications. *Nano Letters*, *10*(11), 4381–4386.

Jones, D., Liu, N., Corbett, B., Lovera, P., Quinn, A. J., & O'Riordan, A. (2011). Surface Plasmon assisted extraordinary transmission in metallic nanohole arrays and its suitability as a bio-sensor. *Journal of Physics: Conference Series*, *307*(1), 012005.

Jung, I., Vaupel, M., Pelton, M., Piner, R., Dikin, D. A., Stankovich, S., … Ruoff, R. S. (2008). Characterization of thermally reduced graphene oxide by imaging ellipsometry. *The Journal of Physical Chemistry C*, *112*(23), 8499–8506.

K. Kolwas, A. Derkachova, D. J. (2015). Tailoring Plasmon Resonances in Metal Nanospheres for Optical Diagnostics of Molecules and Cells. In *Advances in Nanomaterials and Tissue Engineering* (pp. 141-182). Oakville, Canada. Apple Academic Press.

Kalfagiannis, N., Karagiannidis, P. G., Pitsalidis, C., Panagiotopoulos, N. T., Gravalidis, C., Kassavetis, S., … Logothetidis, S. (2012). Plasmonic silver nanoparticles for improved organic solar cells. *Solar Energy Materials and Solar Cells*, *104*, 165–174.

Kamakshi, K., Silva, J. P. B., Sekhar, K. C., Agostinho Moreira, J., Almeida, A., Pereira, M., & Gomes, M. J. M. (2017). Substrate temperature effect on microstructure, optical, and glucose sensing characteristics of pulsed laser deposited silver nanoparticles. *Plasmonics*, *13*(4), 1235–1241.

Kavinkumar, T., & Manivannan, S. (2016). Uniform decoration of silver nanoparticle on exfoliated graphene oxide sheets and its ammonia gas detection. *Ceramics International*, *42*(1), 1769–1776.

Kelly, K. L., Coronado, E., Zhao, L. L., & Schatz, G. C. (2003). The Optical properties of metal nanoparticles: The influence of size, shape, and dielectric environment. *The Journal of Physical Chemistry B*, *107*(3), 668–677.

Kim, S.-H., Lee, C.-H., Yun, J.-M., Noh, Y.-J., Kim, S.-S., Lee, S., … Na, S.-I. (2014). Fluorine-functionalized and simultaneously reduced graphene oxide as a novel hole transporting layer for highly efficient and stable organic photovoltaic cells. *Nanoscale*, *6*(13), 7183–7187.

Kim, Y.-K., Han, S. W., & Min, D.-H. (2012). Graphene oxide sheath on Ag nanoparticle/graphene hybrid films as an antioxidative coating and enhancer of surface-enhanced Raman scattering. *ACS Applied Materials & Interfaces*, *4*(12), 6545–6551.

Krylova, G., & Eremenko, A. (2005). Structure and spectra of photochemically obtained nanosized silver particles in presence of modified porous silica. *International Journal of Photoenergy, 7*(4), 193-198.

Kumar, N., Gupta, B. K., Srivastava, A. K., Patel, H. S., Kumar, P., Banerjee, I., … Varma, G. D. (2015). Multifunctional two-dimensional reduced graphene oxide thin film for gas sensing and antibacterial applications. *Science of Advanced Materials*, *7*(6), 1125–1136.

Kvítek, O., Siegel, J., Hnatowicz, V., & Švorčík, V. (2013). Noble metal nanostructures influence of structure and environment on their optical properties. *Journal of Nanomaterials*, *2013*, 1–15.

Lan, N. T., Chi, D. T., Dinh, N. X., Hung, N. D., Lan, H., Tuan, P. A., … Le, A.-T. (2014). Photochemical decoration of silver nanoparticles on graphene oxide nanosheets and their optical characterization. *Journal of Alloys and Compounds*, *615*, 843–848.

Lee, D., Lee, K., Kim, D. S., Lee, J.-K., Park, S. J., & Choi, M. (2017). Hydrogen-assisted spark discharge generation of highly crystalline and surface-passivated silicon nanoparticles. *Journal of Aerosol Science*, *114*, 139–145.

Lee, K.-C., Lin, S.-J., Lin, C.-H., Tsai, C.-S., & Lu, Y.-J. (2008). Size effect of Ag nanoparticles on surface plasmon resonance. *Surface and Coatings Technology*, *202*(22–23), 5339–5342.

Li, J., Lin, Y., & Zhao, B. (2002). Spontaneous agglomeration of silver nanoparticles deposited on carbon film surface. *Journal of Nanoparticle Research*, *4*(4), 345–349.

Li, J., & Liu, C. (2010). Ag/graphene heterostructures: Synthesis, characterization and optical properties. *European Journal of Inorganic Chemistry*, *2010*(8), 1244–1248.

Li, Y., Zhao, X., Zhang, P., Ning, J., Li, J., Su, Z., & Wei, G. (2015). A facile fabrication of large-scale reduced graphene oxide–silver nanoparticle hybrid film as a highly active surface-enhanced Raman scattering substrate. *Journal of Materials Chemistry C*, *3*(16), 4126–4133.

Liu, L., Liu, J., Wang, Y., Yan, X., & Sun, D. D. (2011). Facile synthesis of monodispersed silver nanoparticles on graphene oxide sheets with enhanced antibacterial activity. *New Journal of Chemistry*, *35*(7), 1418-1423.

Liu, S., Zeng, T. H., Hofmann, M., Burcombe, E., Wei, J., Jiang, R., … Chen, Y. (2011). Antibacterial activity of graphite, graphite oxide, graphene oxide, and reduced graphene oxide: membrane and oxidative stress. *ACS Nano*, *5*(9), 6971–6980.

Liu, X., Li, D., Sun, X., Li, Z., Song, H., Jiang, H., & Chen, Y. (2015). Tunable dipole surface plasmon resonances of silver nanoparticles by cladding dielectric layers. *Scientific Reports*, *5*, 12555.

Lorenzoni, M., Giugni, A., Di Fabrizio, E., Pérez-Murano, F., Mescola, A., & Torre, B. (2015). Nanoscale reduction of graphene oxide thin films and its characterization. *Nanotechnology*, *26*(28), 285301.

Ma, J., Zhang, J., Xiong, Z., Yong, Y., & Zhao, X. S. (2011). Preparation, characterization and antibacterial properties of silver-modified graphene oxide. *Journal of Materials Chemistry, 21*(10), 3350–3352.

Mahmoud, M. A., Chamanzar, M., Adibi, A., & El-Sayed, M. A. (2012). Effect of the dielectric constant of the surrounding medium and the substrate on the surface plasmon resonance spectrum and sensitivity factors of highly symmetric systems: Silver nanocubes. *Journal of the American Chemical Society*, *134*(14), 6434–6442.

Mahmoudi, T., Seo, S., Yang, H. Y., Rho, W. Y., Wang, Y., & Hahn, Y. B. (2016). Efficient bulk heterojunction hybrid solar cells with graphene-silver nanoparticles composite synthesized by microwave-assisted reduction. *Nano Energy*, *28*, 179–187.

Maier, S. A., & Atwater, H. A. (2005). Plasmonics: Localization and guiding of electromagnetic energy in metal/dielectric structures. *Journal of Applied Physics*, *98*(1), 011101.

Maier, S. A., Kik, P. G., Atwater, H. A., Meltzer, S., Harel, E., Koel, B. E., & Requicha, A. A. G. (2003). Local detection of electromagnetic energy transport below the diffraction limit in metal nanoparticle plasmon waveguides. *Nature Materials*, *2*(4), 229–232.

Marcano, D. C., Kosynkin, D. V, Berlin, J. M., Sinitskii, A., Sun, Z., Slesarev, A., … Tour, J. M. (2010). Improved synthesis of graphene oxide. *ACS Nano*, *4*(8), 4806–4814.

Mehl, H., Oliveira, M. M., & Zarbin, A. J. G. (2015). Thin and transparent films of graphene/silver nanoparticles obtained at liquid–liquid interfaces: Preparation, characterization and application as SERS substrates. *Journal of Colloid and Interface Science*, *438*, 29–38.

Messing, M. E., Hillerich, K., Johansson, J., Deppert, K., & Dick, K. A. (2009). The use of gold for fabrication of nanowire structures. *Gold Bulletin*, *42*(3), 172–181.

Mie, G. (1908). Contributions to the Optics of Turbid Media Particularly of Colloidal Metal Solutions. *Annalen Der Physik*, *330*(3), 377–445.

Muhammad Hafiz, S., Ritikos, R., Whitcher, T. J., Md. Razib, N., Bien, D. C. S., Chanlek, N., … Rahman, S. A. (2014). A practical carbon dioxide gas sensor using room-temperature hydrogen plasma reduced graphene oxide. *Sensors and Actuators B: Chemical*, *193*, 692–700.

Murphy, S., Huang, L., & Kamat, P. V. (2013). Reduced graphene oxide–silver nanoparticle composite as an active SERS material. *The Journal of Physical Chemistry C*, *117*(9), 4740–4747.

Noguez, C. (2007). Surface plasmons on metal nanoparticles: The influence of shape and physical environment. *Journal of Physical Chemistry C. 111*(10), 3806–3819.

Orlov, I. A., Sankova, T. P., Babich, P. S., Sosnin, I. M., Ilyechova, E. Y., Kirilenko, D. A., … Puchkova, L. V. (2016). New silver nanoparticles induce apoptosis-like process in E. coli and interfere with mammalian copper metabolism. *International Journal of Nanomedicine*, *11*, 6561–6574.

Panacek, A., Kvítek, L., Prucek, R., Kolar, M., Vecerova, R., Pizúrova, N., … Zboril, R. (2006). Silver colloid nanoparticles: synthesis, characterization, and their antibacterial activity. *The Journal of Physical Chemistry. B*, *110*(33), 16248–16253.

Park, S.-H., Ko, Y.-S., Park, S.-J., Lee, J. S., Cho, J., Baek, K.-Y., … Lee, J.-H. (2015). Immobilization of silver nanoparticle-decorated silica particles on polyamide thin film composite Membranes for antibacterial properties. *Journal of Membrane Science*, *499*, 80–91.

Park, S. H., Roy, A., Beaupré, S., Cho, S., Coates, N., Moon, J. S., … Heeger, A. J. (2009). Bulk heterojunction solar cells with internal quantum efficiency approaching 100%. *Nature Photonics*, *3*(5), 297–302.

Pasricha, R., Gupta, S., Joshi, A. G., Bahadur, N., Haranath, D., Sood, K. N., … Singh, S. (2012). Directed nanoparticle reduction on graphene. *Materials Today*, *15*(3), 118–125.

Qi, J., Lv, W., Zhang, G., Li, Y., Zhang, G., Zhang, F., & Fan, X. (2013). A graphene-based smart catalytic system with superior catalytic performances and temperature responsive catalytic behaviors. *Nanoscale*, *5*(14), 6275–6279.

Raffi, M., Rumaiz, A. K., Hasan, M. M., & Shah, S. I. (2007). Studies of the growth parameters for silver nanoparticle synthesis by inert gas condensation. *Journal of Materials Research*, *22*(12), 3378–3384.

Rafique, S., Abdullah, S. M., Shahid, M. M., Ansari, M. O., & Sulaiman, K. (2017). Significantly improved photovoltaic performance in polymer bulk heterojunction solar cells with graphene oxide /PEDOT:PSS double decked hole transport layer. *Scientific Reports*, *7*(1), 39555.

Rahman, M. M., Hattori, N., Nakagawa, Y., Lin, X., Yagai, S., Sakai, M., … Yamamoto, K. (2014). Preparation and characterization of silver nanoparticles on localized surface plasmon-enhanced optical absorption. *Japanese Journal of Applied Physics*, *53*(11S), 11RE01.

Rai, M., Yadav, A., & Gade, A. (2009). Silver nanoparticles as a new generation of antimicrobials. *Biotechnology Advances*, *27*(1), 76–83.

Reese, C., & Bao, Z. (2007). Organic single-crystal field-effect transistors. *Materials Today*, *10*(3), 20–27.

Ruffino, F., & Grimaldi, M. G. (2013). Au nanoparticles decorated SiO_2 nanowires by dewetting on curved surfaces: facile synthesis and nanoparticles–nanowires sizes correlation. *Journal of Nanoparticle Research*, *15*(9), 1909.

Ruiz, O. N., Fernando, K. A. S., Wang, B., Brown, N. A., Luo, P. G., McNamara, N. D., … Bunker, C. E. (2011). Graphene oxide: A nonspecific enhancer of cellular growth. *ACS Nano*, *5*(10), 8100–8107.

Sarkar, K., Sarkar, K. J., & Banerji, P. (2015). Synthesis of graphene oxide–silver nanocomposite with photochemically grown silver nanoparticles to use as a channel material in thin film field effect transistors. *RSC Advance*, *5*(130), 107811–107821.

Schneid, A. C., Pereira, M. B., Horowitz, F., Mauler, R. S., Matte, C. R., Klein, M. P., … Benvenutti, E. V. (2015). Silver nanoparticle thin films deposited on glass surface using an ionic silsesquioxane as stabilizer and as crosslinking agent. *Journal of the Brazilian Chemical Society*, *26*(5), 1004–1012.

Schropp, R. E. I. (2009). Frontiers in HWCVD. *Thin Solid Films*, *517*(12), 3415–3419.

Schropp, R. E. I. (2015). Industrialization of hot wire chemical vapor deposition for thin film applications. *Thin Solid Films*, *595*, 272–283.

Scott Gilje, Song Han, Minsheng Wang, Kang L. Wang, and, & Richard B. Kaner, (2007). A chemical route to graphene for device applications. *Nano Letters,* 7(11)*,* 3394–3398.

Seney, C. S., Gutzman, B. M., & Goddard, R. H. (2009). Correlation of size and surface-enhanced raman scattering activity of optical and spectroscopic properties for silver nanoparticles. *The Journal of Physical Chemistry C*, *113*(1), 74–80.

Serrano, A., Rodríguez de la Fuente, O., & García, M. A. (2010). Extended and localized surface plasmons in annealed Au films on glass substrates. *Journal of Applied Physics*, *108*(7), 074303.

Shahverdi, A. R., Fakhimi, A., Shahverdi, H. R., & Minaian, S. (2007). Synthesis and effect of silver nanoparticles on the antibacterial activity of different antibiotics against Staphylococcus aureus and Escherichia coli. *Nanomedicine: Nanotechnology, Biology and Medicine*, *3*(2), 168–171.

Smith, C. T. G., Rhodes, R. W., Beliatis, M. J., Imalka Jayawardena, K. D. G., Rozanski, L. J., Mills, C. A., & P. Silva, S. R. (2014). Graphene oxide hole transport layers for large area, high efficiency organic solar cells. *Applied Physics Letters*, *105*(7), 073304.

Steinkraus, G., White, R., & Friedrich, L. (2007). Vancomycin MIC creep in non-vancomycin-intermediate Staphylococcus aureus (VISA), vancomycin-susceptible clinical methicillin-resistant S. aureus (MRSA) blood isolates from 2001-05. *The Journal of Antimicrobial Chemotherapy*, *60*(4), 788–794.

Su, Ke, Y.-F., Cai, S.-L., & Yao, Q.-Y. (2012). Surface plasmon resonance of layer-by-layer gold nanoparticles induced photoelectric current in environmentally-friendly plasmon-sensitized solar cell. *Light: Science & Applications*, *1*(6), e14.

Su, Y.-A., Lin, W.-C., Wang, H.-J., Lee, W.-H., Lee, R.-H., Dai, S. A., … Jeng, R.-J. (2015). Enhanced photovoltaic performance of inverted polymer solar cells by incorporating graphene nanosheet/AgNPs nanohybrids. *RSC Advance*, *5*(32), 25192–25203.

Sutradhar, P., & Saha, M. (2016). Silver nanoparticles: Synthesis and its nanocomposites for heterojunction polymer solar cells. *The Journal of Physical Chemistry C*, *120*(16), 8941–8949.

Tai, F. C., Lee, S. C., Wei, C. H., & Tyan, S. L. (2006). Correlation between ID⁄IG Ratio from visible Raman spectra and sp^2/sp^3 ratio from XPS spectra of annealed hydrogenated DLC film. *Materials Transactions*, *47*(7), 1847–1852.

Takami, S. (2012). Application 41 – Surface modification of inorganic nanoparticles by organic functional groups. In *Nanoparticle Technology Handbook* (pp. 593–596). Oxford, United Kingdom. Elsevier.

Tam, L. T., Phan, V. N., Lan, H., Thuy, N. T., Hien, T. M., Huy, T. Q., … Le, A.-T. (2013). Characterization and antimicrobial activity of silver nanoparticles prepared by a thermal decomposition technique. *Applied Physics A*, *113*(3), 613–621.

Tang, J., Chen, Q., Xu, L., Zhang, S., Feng, L., Cheng, L., … Peng, R. (2013). Graphene oxide-silver nanocomposite as a highly effective antibacterial agent with species-specific mechanisms. *ACS Applied Materials & Interfaces*, *5*(9), 3867–3874.

Thangala, J., Vaddiraju, S., Malhotra, S., Chakrapani, V., & Sunkara, M. K. (2009). A hot-wire chemical vapor deposition (HWCVD) method for metal oxide and their alloy nanowire arrays. *Thin Solid Films*, *517*(12), 3600–3605.

Thouti, E., Kumar, V., Parashar, P. K., Reddy, G. B., Pasricha, R., & Komarala, V. K. (2015). Optical properties of silver nanoparticles integrated graphene oxide thin films on glass and silicon substrates. *Plasmonics*, *10*(5), 1063–1069.

Tran, M.-H., & Jeong, H. K. (2015). Synthesis and characterization of silver nanoparticles doped reduced graphene oxide. *Chemical Physics Letters*, *630*, 80–85.

Tuinstra, F. (1970). Raman spectrum of graphite. *The Journal of Chemical Physics*, *53*(3), 1126.

Venugopal, N., & Mitra, A. (2013). Influence of temperature dependent morphology on localized surface plasmon resonance in ultra-thin silver island films. *Applied Surface Science*, *285*, 357–372.

Wan, S., Bi, H., Zhou, Y., Xie, X., Su, S., Yin, K., & Sun, L. (2017). Graphene oxide as high-performance dielectric materials for capacitive pressure sensors. *Carbon*, *114*, 209–216.

Willets, K. A., & Van Duyne, R. P. (2007). Localized surface plasmon resonance spectroscopy and sensing. *Annual Review of Physical Chemistry*, *58*, 267–297.

Xiang, F., Li, B., Li, Y., Zhou, J., Gan, …... and H (2016). Preparation of silver-coated glass frit and its application in silicon solar cells. *Chinese Physics B*, *25*(7), 078110.

Xiu, Z., Zhang, Q., Puppala, H. L., Colvin, V. L., & Alvarez, P. J. J. (2012). Negligible particle-specific antibacterial activity of silver nanoparticles. *Nano Letters*, *12*(8), 4271–4275.

Xu, C., & Wang, X. (2009). Fabrication of flexible metal-nanoparticle films using graphene oxide sheets as substrates. *Small,* *5*(19), 2212–2217.

Zainy, M., Huang, N. M., Vijay Kumar, S., Lim, H. N., Chia, C. H., & Harrison, I. (2012). Simple and scalable preparation of reduced graphene oxide–silver nanocomposites via rapid thermal treatment. *Materials Letters*, *89*, 180–183.

Zhang, P., Wang, H., Zhang, X., Xu, W., Li, Y., Li, Q., … Su, Z. (2015). Graphene film doped with silver nanoparticles: self-assembly formation, structural characterizations, antibacterial ability, and biocompatibility. *Biomaterials Science*, *3*(6), 852–860.

Zhang, X., Zhang, J., Wang, H., Hao, Y., Zhang, X., Wang, T., … A, J. P. K. and E.-S. M. (2010). Thermal-induced surface plasmon band shift of gold nanoparticle monolayer: morphology and refractive index sensitivity. *Nanotechnology*, *21*(46), 465702.

Zhao, G., & Jr, S. E. S. (1998). Multiple parameters for the comprehensive evaluation of the susceptibility of Escherichia coli to the silver ion. *Biometals*, *11*(1), 27–32.

Zhou, Y., Yang, J., Cheng, X., Zhao, N., Sun, L., Sun, H., & Li, D. (2012). Electrostatic self-assembly of graphene–silver multilayer films and their transmittance and electronic conductivity. *Carbon*, *50*(12), 4343–4350.

Zhu, Z., Su, M., Ma, L., Ma, L., Liu, D., & Wang, Z. (2013). Preparation of graphene oxide-silver nanoparticle nanohybrids with highly antibacterial capability. *Talanta*, *117*, 449–455.